Chem Soc Rev

REVIEW ARTICLE

View Article Online
View Journal | View Issue

Cite this: *Chem. Soc. Rev.*, 2019, **48**, 2366

Advances in porous and nanoscale catalysts for viable biomass conversion

Putla Sudarsanam, *[a] Elise Peeters, [a] Ekaterina V. Makshina, [a] Vasile I. Parvulescu[b] and Bert F. Sels *[a]

Heterogeneous catalysis is a promising technology for the valorization of renewable biomass to sustainable advanced fuels and fine chemicals. Porosity and nanostructure are the most versatile features of heterogeneous solid catalysts, which can greatly determine the accessibility of specific active sites, reaction mechanisms, and the selectivity of desirable products. Hence, the precise tuning of porosity and nanostructure has been a potential strategy towards developing novel solid catalysts with indispensable characteristics for efficient biomass valorization. Herein, we present a timely and comprehensive review of the recent advances in catalytic biomass conversions over microporous zeolites, mesoporous silicas, and nanostructured metals/metal oxides. This review covers the catalytic processing of both edible (lipids and starch) and non-edible (lignocellulose) biomass as well as their derived compounds, along with a systematic evaluation of catalyst reusability/kinetic/mechanistic aspects in the relevant processes. The key parameters essential for tailoring particle size, morphology, porosity, acid–base, and redox properties of solid catalysts are emphasized, while discussing the ensuing catalytic effects towards the selective conversion of biomass into desirable chemicals. Special attention has been drawn to understand the role of water in liquid phase biomass conversions as well as the hydrothermal stability and the deactivation of nanoporous catalysts. We believe this comprehensive review will provide new insights towards developing state-of-the-art solid catalysts with well-defined porosity and nanoscale properties for viable biomass conversion.

Received 31st May 2018

DOI: 10.1039/c8cs00452h

rsc.li/chem-soc-rev

1. Introduction

Escalating energy demand, depletion of fossil fuels, and abnormal climate change are the major problems facing humankind in the 21st century.[1–5] Non-renewable fossil fuels (coal, crude oil, and natural gas) currently provide more than 90% of our energy needs. Nevertheless, the surplus consumption of fossil fuels is the primary reason for increasing levels of atmospheric CO_2 and hence, global warming, a major threat to all living organisms. The utilization of renewable energy sources (wind, solar, geothermal, hydropower, and biomass) as alternatives to fossil fuels is one of the promising solutions for a more sustainable society. The valorization of biomass (an abundant non-fossil carbon source) has particularly attracted a lot of attention because of its ability to provide a wide range of valuable functionalized chemicals and high-energy density fuels (Fig. 1). Biomass is the fourth largest source of energy, after crude oil, coal, and natural gas and has been used to generate heat and power over the last few decades.[6] Nature itself produces huge amounts of biomass *via* photosynthesis using water, sunlight, and atmospheric CO_2 (Fig. 2).[6] Hence, the efficient valorization of biomass could not only provide useful fuels and chemicals, but also assist to reduce the net emissions of CO_2 by an interplay chemistry of photosynthesis and biorefinery processes. Consequently, biofuel share is predicted to reach about 9% in the transport sector by 2030.[4] The utilization of naturally abundant biomass as a feedstock for chemicals production can also boost the principles of green chemistry within the context of sustainability.[7]

Biomass can be largely derived from lignocellulose, lipids, and starch crops.[8,9] A number of feasible processes and technologies, mostly catalytic based routes, have been developed for biomass valorization. These include biochemical (enzymatic hydrolysis and fermentation), thermochemical (combustion, pyrolysis, and gasification), hydroprocessing, oxidation, (*trans*)-esterification, isomerization, dehydration, hydrolysis, and many others. For instance, bioethanol is produced *via* fermentation of edible biomass feedstocks (sugar cane or corn).[10,11] Vegetable oils, obtained from food sources (soybeans, palm or sunflower), are the raw materials for biodiesel production *via* catalytic

[a] *Centre for Surface Chemistry and Catalysis, Faculty of Bioscience Engineering, KU Leuven, Celestijnenlaan 200f, 3001, Heverlee, Belgium. E-mail: sudarsanam.putla@kuleuven.be, putla2007@gmail.com, bert.sels@kuleuven.be; Fax: +32 16 321 998; Tel: +32 16 321 610*
[b] *University of Bucharest, Department of Organic Chemistry, Biochemistry and Catalysis, B-dul Regina Elisabeta 4-12, Bucharest 030016, Romania*

transesterification reaction.[12,13] By using thermochemical methods, all plant-based residues can be converted into bio-oil or syngas.[9,14] Catalytic hydroprocessing methods are essential for upgrading biomass-derived platform molecules to fuel grade chemicals. On the other hand, biopolymer building blocks can be produced *via* catalytic oxidation of biomass-derived compounds. Recently, the reductive catalytic fractionation process has attracted much attention as this strategy converts non-edible lignocellulosic biomass into two valuable fractions: (i) lignin-based phenolic compounds and (ii) (hemi)cellulose pulp.[15–17] Fig. 2 shows the structure of lignocellulose with the major components: cellulose, hemicellulose, and lignin. In many of these biomass conversions, selectively directing a reaction pathway towards desirable chemicals remains a great

Putla Sudarsanam

Putla Sudarsanam (1986), currently Marie Curie Postdoctoral Fellow at KU Leuven (Belgium), obtained his PhD degree in Chemistry (2015) from CSIR-Indian Institute of Chemical Technology, India (Supervisor: Dr B. Mahipal Reddy). Before joining at KU Leuven, he did postdoctoral work with Prof. Suresh Bhargava (RMIT University, Melbourne, 2014–2016) and with Prof. Angelika Brückner (Leibniz Institute for Catalysis, Germany, 2017). His research focuses on developing heterogeneous solid catalysts for biomass valorization, CO_2 upgrading, green chemistry, and environmental protection. He received several awards/fellowships, including Marie Skłodowska-Curie Fellowship-2016, Leibniz-DAAD Postdoc Fellowship-2016, Best PhD Thesis Award-2015 (The Catalysis Society of India), EuropaCat PhD Student Award-2013 (XIth European Congress on Catalysis, France) and Endeavour Research Fellowship-2013 (Australia). He authored about 50 peer-reviewed journal articles with an h-index of 25 and more than 1550 citations.

Elise Peeters

Elise Peeters obtained her MSc degree in Bioscience Engineering (Catalytic Technology) at KU Leuven (Belgium) in 2017. She completed her master's thesis at the Centre for Surface Chemistry and Catalysis under the supervision of Prof. Bert Sels, where she studied the hydrodeoxygenation of (ligno)cellulose into liquid short alkanes. She is currently pursuing a PhD in the same group as an FWO-funded fellow. Her current research topic focuses on the efficient conversion of biomass-derived molecules by Sn-BEA catalysis.

Ekaterina V. Makshina

Dr Ekaterina V. Makshina obtained her PhD degree in 2007 in the frame of a cooperation agreement (Co-tutelle) of Moscow State University (Russia) and Littoral University (France) working on the topic of methanol and VOCs oxidation over supported oxide catalysts. In 2010, she joined the group of Prof. Sels at the Centre for Surface Chemistry and Catalysis (KU Leuven). Her research expertise covers the development of the solid catalysts and new processes targeting biomass transformation into commodity chemicals.

Vasile I. Parvulescu

Vasile I. Parvulescu received his PhD from the Polytechnic University of Bucharest in 1986 with a thesis investigating the selectivity of bi- and multi-metal catalysts in hydrogenation of aromatic hydrocarbons. After several years as high-signor researcher at the Institute of Inorganic and Rare Metals, in 1992 he joined the University of Bucharest, where he becomes full professor in 1999. He is currently director of the Department of Organic Chemistry, Biochemistry and Catalysis. His scientific interest concerns the study of heterogeneous catalysts for green and fine chemistry and environmental protection. He authored more than 380 papers, 27 patents, and 7 books. He was awarded by the Romanian Academy ("Nicolae Teclu" Award, 1990), Romanian President (Knight for Merits, 2008) and The National Grand Lodge of Romania ("Grigore Moisil" award for exact sciences, 2015).

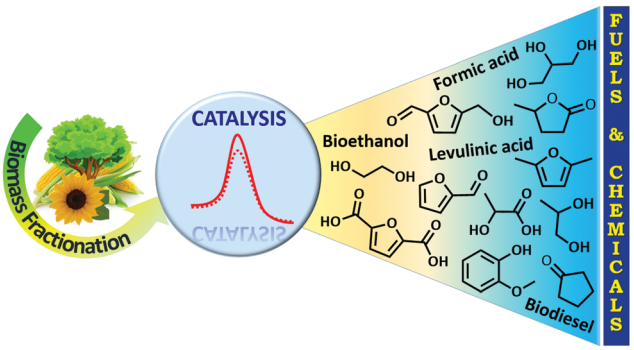

Fig. 1 Catalytic biomass upgrading into high-value fuels and fine chemicals.

challenge due to uncontrolled interactions between the catalyst active sites and the biomass molecules.

The application of heterogeneous solid catalysts, alternative to homogeneous liquid catalysts, in biomass valorization is of great importance because of their versatile physicochemical properties, high hydrothermal stability, and efficient catalyst recovery/reusability.[18,19] Indeed, heterogeneous catalysis field contributes to about 90% of chemical production processes and to more than 20% of all industrial products.[3] The most notable features of a solid catalyst that can play a beneficial role in catalytic reactions are particle size, shape, and porosity. For example, the reduction of a catalyst particle size to nanoscale (1–100 nm size in at least one dimension) can lead to the generation of novel catalytic materials with enriched surface active sites, modified interaction specificities, and improved redox properties that could be substantially different from their bulk counterparts.[20–23] The specific surface area of nanosized catalysts can also be largely improved due to higher surface to volume ratio (Fig. 3), enabling facile accessibility of surface

Bert F. Sels

Bert F. Sels (1972), currently full professor at KU Leuven, obtained his PhD degree in 2000 in the field of heterogeneous oxidation catalysis. He was awarded the DSM Chemistry Award in 2000, the Incentive Award by the Belgian Chemical Society in 2005, and the Green Chemistry Award in 2015. He is currently director of the Centre for Surface Chemistry and Catalysis, designing heterogeneous solid catalysts for future challenges in industrial organic and environmental catalysis. His expertise includes heterogeneous catalysis in bio-refineries, design of hierarchical zeolites and carbons and the spectroscopic and kinetic study of active sites for small-molecule activation. He authored about 310 peer-reviewed journal articles with an h index of 75 and more than 18100 citations, and filed 25 patents.

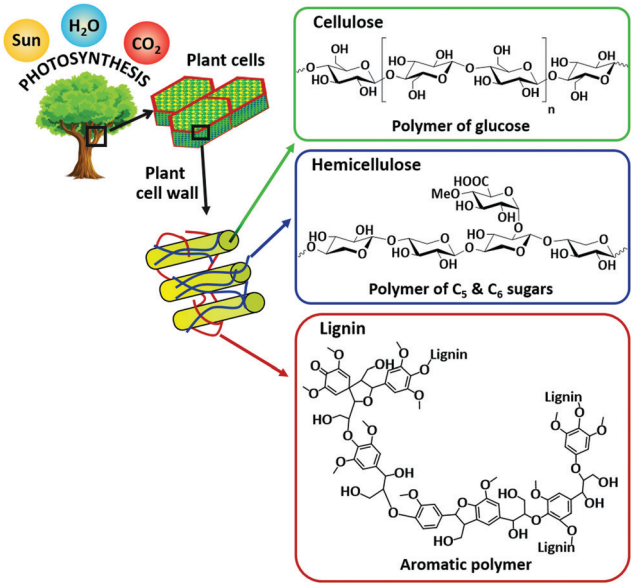

Fig. 2 Structure of lignocellulose biomass with the major components: cellulose, hemicellulose, and lignin.

active sites to biomass molecules.[21] The use of metal nanoparticles (Ag NPs and Pt NPs) in catalysis has already been attempted in the 19th century for photography as well as for H_2O_2 decomposition, respectively.[24] In 1940s, the Nord group reported the catalytic application of nanomaterials for nitrobenzene reduction.[25,26] In 1970s and 1980s, Parravano *et al.*[27] and Haruta *et al.*[28] developed various supported nano-Au catalysts for hydrogen transfer and for low temperature CO oxidation, respectively. On the other hand, fine-tuning the particle morphology of a catalyst, especially of metals or metal oxides, will optimize the electronic and geometrical properties at the catalyst surface. Shape-controlled nanoscale metal oxides can preferentially expose large amounts of surface-active crystal facets. As a result, the interactions between the active sites and the reactive species could be enhanced, which is a key driving force for obtaining improved reaction rates in biomass valorization.

In addition to particle size and morphology, controlling the porosity of solid catalysts is also indispensable for improving catalyst activity and product selectivity (Fig. 3). The pore dimensions of solid catalysts can directly influence the diffusion properties of reactive species during biomass conversion reactions.[21,29] Moreover, the use of well-defined porous materials as catalyst supports can provide specific adsorption sites for stabilizing catalytic active phases.[22] Microporous zeolites and mesoporous silicas are widely studied porous materials in catalytic biomass conversions.[30–34] A major challenge in using these single-mode porous materials as catalysts for biomass-related reactions is the mass transport limitations because biomass molecules are complex and highly viscous. For instance, active sites (*e.g.*, acid sites) are predominantly located inside the micropores of the zeolites, making the diffusion of larger biomass molecules through the confined micropores more difficult. This will lead to low conversion rates, uncontrolled product selectivity, and rapid catalyst deactivation. In

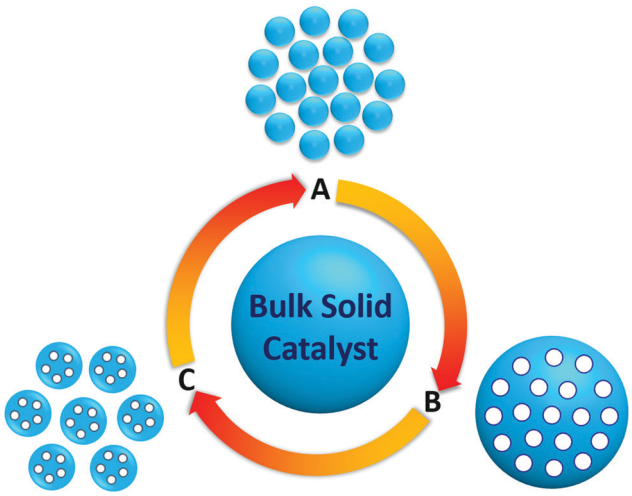

Fig. 3 Exemplary routes to improve surface area and diffusion properties of bulk solid catalysts: (A) reduction of particle size with shape-control, (B) introduction of pores, and (C) combination of both particle size reduction and introduction of pores.

this respect, hierarchically porous materials containing multiple-scale pores (micro, meso, or macro) have attracted great attention because of their favourable catalytic properties compared to single-mode porous analogues.[35,36] These unique porous materials not only combine the advantages of active site accessibility and efficient mass transport effects, but also endow ample space for the incorporation of catalytically active phases, including metal nanoparticles (Au, Pd, Ru, Rh, Cu, Ni, Fe, *etc.*) or acid–base species ($-SO_3H$, $-NH_2$, *etc.*).

1.1 Scope of the review

Over the last ten years, tremendous research endeavors have been undertaken towards developing a variety of novel heterogeneous solid catalysts for the efficient conversion of biomass to sustainable advanced fuels and fine chemicals. These efforts mainly devoted towards fine-tuning of particle size, shape, surface structure, and porosity of solid catalysts with the aim of enriching the surface active sites both electronically and geometrically. This will control the interactions of catalytically active sites with the biomass molecules, directing a preferential reaction pathway to obtain desirable products. These developments have been made largely in hydroprocessing, oxidation, hydrolysis, (*trans*)esterification, isomerization, and dehydration of various biomass feedstocks and their derived compounds. Consequently, several review articles have been published on the topic of catalytic biomass valorization. For instance, the Pierre Gallezot group provided a review article on biomass conversions over metal-based catalysts.[37] Wang *et al.*[34] summarized the catalytic applications of nanoporous materials for biomass valorization. In 2016, the Sels group published a critical review on potential and challenges of zeolites for catalytic biomass upgrading.[8] A few reviews have been also published on the topic of designing mesoporous silica materials for various applications.[33,38] However, the catalytic applications of mesoporous silica materials including for biomass valorization has not yet been summarized in detail. As well, many interesting results have been recently published on catalytic biomass conversion over microporous zeolites and nanoscale metals/metal oxides. Hence, a timely comprehensive review, highlighting the importance of both porosity and nanoscale properties of solid catalysts for biomass valorization, is essential for the benefit of both academia and industry researchers. Based on the above background, this review aims to provide a detailed summary of the recent advances in the catalytic applications of microporous zeolites, mesoporous silica materials, and nanoscale metals/metal oxides for biomass valorization (Fig. 4). In each section, several feasible approaches developed for fine-tuning the particle size, morphology, and the porosity of above-mentioned catalysts are emphasized, while discussing the role of ensuing catalytic effects in biomass conversions. The catalytic processing of both edible (lipids and starch) and non-edible (lignocellulose) biomass substrates and their derived compounds are summarized in detail. We believe that this comprehensive review will act as a useful source to guide researchers towards developing state-of-the-art solid catalysts with well-defined nanoscale and porosity properties for a viable bio-refinery industry.

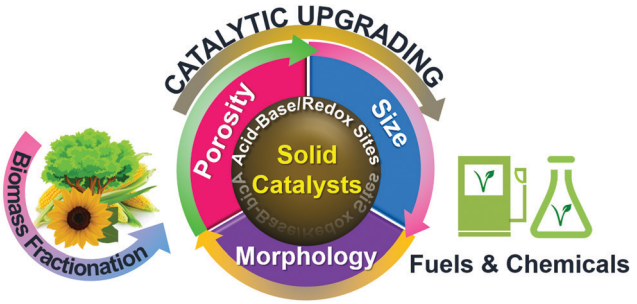

Fig. 4 Schematic overview of this review.

2. Zeolite-based catalysts for biomass valorization

Zeolites are the most extensively used solid catalysts in chemical industry, for instance in catalytic cracking of crude oil, Friedel–Crafts reactions, acid-catalyzed chemical transformations, and recently for biomass conversion.[30,39,40] The application of zeolites in oil refinery resulted in about 30% increase in gasoline yield, indicating their importance in petrochemical industry.[39] The unique ability of zeolites to adsorb water and release it upon heating has paved the way for the development of synthetic zeolites A, B, and X (Linde division of Union Carbide, 1940).[41] Subsequently, the scientific community has recognized the exceptional role of zeolites in shape-selective catalysis. Zeolites are crystalline microporous aluminosilicates, with pore sizes normally in the range of 0.3–2 nm. They typically contain three-dimensional networks of MO_4 tetrahedral units (M = Al, Si), connected *via* corner-sharing oxygen atoms to form highly ordered interconnected pores (Fig. 5). The porous structure of zeolites can accommodate several cations, such as H^+, Na^+, K^+, and Mg^{2+}, along with abundant water molecules.

Hence, zeolites can be represented by an empirical formula, namely $M_{2/n}O{\cdot}Al_2O_3{\cdot}xSiO_2{\cdot}yH_2O$, where M = heterocation, n = cation valence, x = 2–200, and y = number of water molecules. The substituted cations are predominantly located in relatively large cavities formed by negatively charged $[Si_{1-x}Al_xO_2]^{x-}$ framework, where $x \leq 0.5$ (Lowenstein's rule).[42] The International Zeolite Association has recognized over 200 zeolite frameworks so far, but only about 10 types have found practical applications.[40] The value of global zeolite market was about 1.30 billion USD in 2013 and is estimated to reach 1.76 billion USD in 2020, signifying the continuous growth of zeolites industry.[39]

2.1 Catalytic role of zeolite properties in biomass valorization

Zeolite-based catalysts are of great interest for biomass valorization because of their unique porous structure, shape selectivity, and strong acidity.[8,41,43] Especially, the tunable Brønsted/Lewis acidity is a vital feature of zeolites that can significantly determine their catalytic activity and selectivity in biomass upgrading.[40,44] The substitution of Si^{4+} by Al^{3+} in the tetrahedral framework of the zeolite is the driving force for the formation of Brønsted acid sites.[30,45] This is because incorporation of Al^{3+} into the zeolite framework generates a negative charge (Fig. 5), that needs to be compensated by cations to maintain the charge balance.[45] If the substituted cation is a proton (H^+), the resulting zeolite contains strong Brønsted acidity (Fig. 5). It is therefore obvious that with the increase of Al/Si ratio (or decrease of Si/Al ratio) the number of Brønsted acid sites in the zeolite framework increases if all the cation sites are occupied by protons. Nevertheless, when the amount of Al reaches a certain limit, weak Brønsted acid sites can be formed due to the accumulation of excess protons in the zeolite pores. On the other hand, the Lewis acidity of zeolites is dependent on the extra-framework Al and/or the substituted heterocations.[44,46,47] The extra-framework Al can present as isolated Al_2O_3 particles in the zeolite structure,

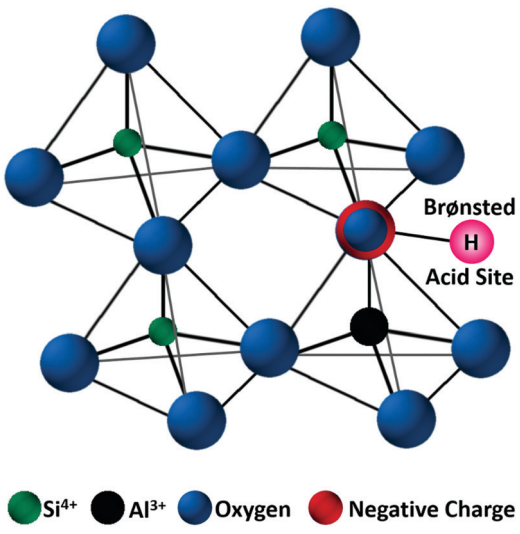

Fig. 5 Representative zeolite framework of a tetrahedral $[SiO_4]^{4-}$, with generation of a negative charge due to the incorporation of Al^{3+} and substitution of a proton to maintain the charge balance. Adapted with permission from ref. 45. Copyright (2002) Elsevier.

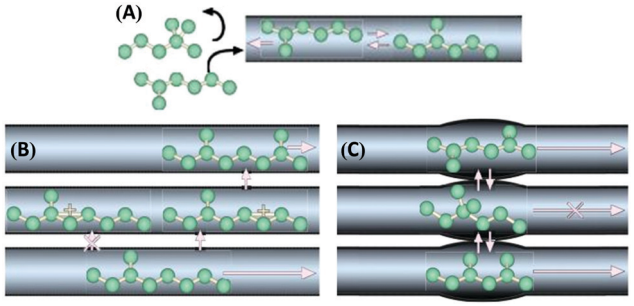

Fig. 6 Different types of shape selectivity in zeolites: (A) reactant shape selectivity, (B) transition state shape selectivity, and (C) product shape selectivity. Reproduced with permission from ref. 50. Copyright (2008) Springer Nature.

which are usually formed during the calcination of zeolites at higher temperatures. Sometimes, these isolated Al_2O_3 particles can also be formed during the synthesis process due to unsuccessful incorporation of excess Al into the zeolite framework. Besides, metals (*e.g.*, Ti, Zr, Hf, Nb, or Ta) incorporated into the zeolite frameworks can act as Lewis acidic sites. The improved hydrophobic nature is an added benefit of these metallozeolites, which is an important criterion for their catalytical applications in hydrothermal biomass conversions.

Shape-selectivity of zeolites, originated by precisely defined pore systems, plays a crucial role in promoting a specific reaction pathway for obtaining desirable chemicals.[40,41,48,49] The different pore window size of zeolites can cause selective active site accessibility and mass transfer effects as shown in Fig. 6.[50] For instance, only reactant molecules with suitable sizes and configurations relative to the pore window size of zeolites can reach internal active sites (reactant shape selectivity, Fig. 6A).[49,50] Similarly, zeolite pores can impose steric hindrance to the reaction and determine the formation of transition state molecules (transition state shape selectivity, Fig. 6B). Simultaneously, products with smaller size than the pore sizes of the zeolite are selectively formed (product shape selectivity, Fig. 6C).

Catalytically active (acid) sites are predominantly present inside the micropores of zeolites. In the case of upgrading larger biomass molecules (polysaccharides, disaccharides, lignin, triglycerides, *etc.*), active site accessibility is a key concern because of severe mass transfer constraints imposed by micropores, which may lead to low conversion rates. For instance, zeolites having a free pore aperture of 0.74 nm do not allow the diffusion of larger sucrose molecules (diameter is 0.88 nm) to reach the internal acid sites.[51] To circumvent this problem, the development of hierarchical porous zeolites containing a multimodal pore size distribution has attracted a lot of attention, as this strategy combines the advantages of micropores (provide active sites and determine shape-selectivity) as well as mesopores (facilitate rapid mass transfer properties).[31,52] New active sites can also be formed in hierarchical zeolites due to structural modifications and perturbations that occur during their synthesis. For example, the alkaline treatment of zeolites led to the formation of a new type of surface basic sites, along with innate acid–base

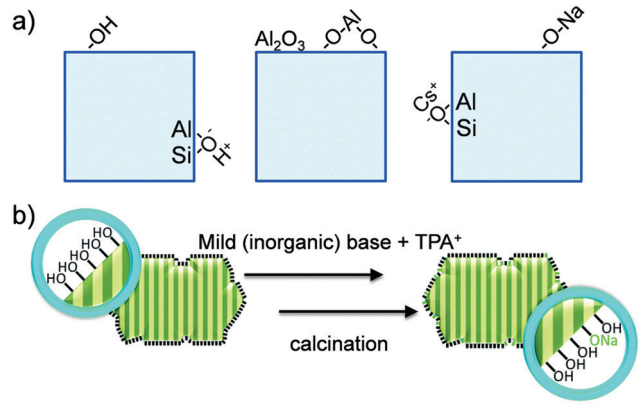

Fig. 7 Formation of various active sites in hierarchical zeolites. (a) Typical Brønsted acid sites and surface hydroxyl groups (left), Lewis acid sites derived from steaming and alkaline-induced surface realumination (middle), and basic sites generated by the framework or by the formation of surface-bound alkali cations (right). (b) Generation of novel surface basic sites by tailored alkaline treatment. Reproduced with permission from ref. 31 and 52. Copyright (2016) Royal Society of Chemistry and Copyright (2014) John Wiley and Sons, respectively.

sites, which may exhibit favourable catalytic effects in biomass valorization (Fig. 7).[31,52]

Owing to their high specific surface area, zeolites are efficient support materials for the stabilization/dispersion of active phase metals/metal oxides (Pd, Pt, Au, Ru, Ag, Ni and V_2O_5).[30,53] Advantages of acid properties of zeolites coupled with the redox properties of metals can lead to the generation of novel, versatile catalysts with improved activities and selectivities. The incorporated heterocations (*e.g.*, Cu) in zeolite structures can also play a vital role in modifying the chemical and surface properties of zeolite supported metal oxide (V_2O_5) catalysts, resulting in optimized host–guest interaction that will direct the formation of desirable bio-based chemicals (*e.g.*, 2,5-diformylfuran).[53] Moreover, the presence of secondary voids in hierarchical zeolites can offer an ideal space for the deposition of adequate amounts of catalytically active metals or metal oxides.

2.2 Pristine and substituted zeolites

Zeolite-Y, developed by Union Carbide (1959), was the first zeolite applied (as isomerization catalyst) in chemical industry and later, zeolite-X (Mobil Oil, 1962) was used as hydrocarbon cracking catalyst.[54] Owing to attractive acid and porous properties, the use of both pristine and modified zeolites has gained paramount attention for catalytic biomass conversions.[55]

2.2.1 Catalytic fast pyrolysis of biomass. Catalytic fast pyrolysis (CFP) is one of most widely used processes to directly valorize lignocellulosic biomass towards fuel grade chemicals in a single-step. This process can provide high-quality bio-oil with low oxygen content, making it potentially more compatible with the current refining infrastructure.[56] Substantial efforts have been made in the CFP of lignocellulose using a variety of zeolite-based catalysts. For instance, the catalytic performance of a HZSM-5 zeolite was investigated for in-situ CFP of woody biomass in a pilot-scale circulating fluidized-bed reactor.[57] A considerable improvement in the conversion of pyrolysis vapors was observed with the increase of catalyst-to-biomass (C/B) ratio. However, preserving bio-oil quality is a great challenge at higher C/B ratio conditions. HZSM-5 zeolite was also found to be effective in the CFP of sugarcane bagasse (both pretreated and raw materials) carried out in a fluidized-bed reactor.[58] About 12.4 and 10.9% yields of aromatics and olefins, respectively, were achieved in the case of pretreated biomass. The presence of inorganic residue elicited rapid catalyst deactivation due to the blockage of zeolite pores. This indicates that by removing the inorganic residue, both zeolite stability and hydrocarbon yields can be improved. Interestingly, higher yields of aromatics *via* co-pyrolysis of bagasse with bio-plastic were obtained over a dual USY/HZSM-5 catalyst layout compared to the corresponding pristine zeolites (USY and HZSM-5).[59] This reveals the synergistic effect of the dual-catalyst design for CFP biomass process. Similar results (higher aromatic yields and low coke formation) in the CFP of cellulose were also achieved over a physically mixed catalyst system of dealuminated HY (Si/Al = 327) and HZSM-5 (Si/Al = 30).[60] This study has shown the significance of interactive effects of zeolites' pore structure and their acidity for efficient CFP of biomass. Chagas *et al.*[61] pointed out that the strongly acidic HZSM-5 zeolite with low SiO_2/Al_2O_3 ratio (Si/Al = 23) is effective towards aromatics production in the CFP of Spirulina. In contrast, less acidic zeolites gave mainly aliphatic hydrocarbons, phenols, and few nitrogenates. The beneficial effect of strong Brønsted acidic sites of HZSM-5 zeolite (SiO_2/Al_2O_3 ratio = 23) towards aromatics production was also noticed in the CFP of red pepper stems.[62] Disparate findings were attained in the case of SAPO-34, ZSM-5, and Y zeolites for the pyrolysis of cellulose.[63] ZSM-5 exhibited higher yields of aromatics, whereas Y zeolite displayed a distinct role towards phenols formation at temperatures above 700 °C. In contrast, greater amounts of water and furfural derivatives were obtained with SAPO-34 catalyst. Zhang *et al.*[64] demonstrated that with increasing Si/Al ratios (ranging from 20 to 300) of HZSM-5, yields of hydrocarbons and light phenols were decreased dramatically during in-situ catalytic conversion of biomass fast pyrolysis vapors.

The catalytic pyrolysis of cellulose, cellobiose, lignin, and switch grass was strongly dependent on the loading of Fe (1.4, 2.8 and 4.2 wt%) in Fe-modified HZSM-5 zeolites synthesized by partial ion exchange of NH_4ZSM-5 with Fe(II).[65] Especially, the 1.4 wt% Fe loaded HZSM-5 was demonstrated to be efficient towards aromatics production (mainly benzene and naphthalene). Like Fe, addition of Zn, Ga, and Ni to HZSM-5 has a profound effect in the CFP of eucalyptus urophylla.[66] Among those, the Ga-modified zeolite gave the highest amount of aromatics (especially xylenes), whereas low yields were achieved over Ni-modified HZSM-5 catalyst. Hydrocarbon yield and heating value of dry oil were largely improved in the CFP of ground corncob catalyzed by ZSM-5 zeolite (Si/Al = 25) coated ceramic honeycomb (ZCCH).[67] In addition, the ZCCH catalyst can prevent the formation of undesirable products including light oxygenates and furans. In USY zeolite catalyzed CFP of de-oiled *Millettia* (*Pongamia*) *pinnata* seed waste, selectivity of monocyclic aromatic hydrocarbons was found to increase from

4.7–17.4% to 52.5–56.5% when the ratio of biomass : catalyst increased from 1 : 1 to 1 : 5 at 500 °C, respectively.[68] Moreover, zeolite catalyst played a crucial role in selective cleavage of carbon chain towards production of only shorter hydrocarbons (C_{5-12}). The Si/Al ratio was found to be a key factor to tune the catalytic performance of MCM-22 zeolite for the CFP of acid-washed wheat straw.[44] The MCM-22 zeolite with the lowest Al content (Si/Al = 40) provided higher bio-oil deoxygenation activity at 450 °C pyrolysis temperature. Interestingly, an increase in the pyrolysis temperature led to the deposition of a lower amount of coke on the zeolite. On the other hand, reducing the Si/Al ratio (which creates abundant acid sites) had a negative effect on product selectivity since acid sites favored the undesirable side reactions, leading to formation of gaseous hydrocarbons and higher coke deposits. A steel slag-derived zeolite (FAU-SL) catalyst afforded maximum yield (47 wt%) of bio-oil from the pyrolysis of oil palm mesocarp fiber, which was carried out in a fixed-bed reactor.[69] High mesoporosity and strong surface acidity of FAU-SL were the primary factors to obtain better activity results in this study. Zeolite structure and its acidity were found to show a great effect in the production of phenols from CFP of lignin.[70] Notably, large-pore-size zeolites (*e.g.*, FAU) with Si/Al = 15 are highly selective towards phenols formation.

2.2.2 Upgrading of carbohydrates and their derivatives. Glucose isomerization, a Lewis acid-catalyzed reaction, is one of the crucial steps in biomass valorization to obtain a number of valuable platform molecules (Fig. 8). Christianson *et al.*[71] performed computational studies to understand the mechanism for glucose isomerization and epimerization over Sn-β based zeolites. An energetically favorable reaction pathway was observed for glucose-to-mannose transformation *via* two subsequent 1,2 intramolecular hydride transfer steps. Interestingly, Na exchange in Sn-β zeolite influences the mechanism of glucose-to-mannose transformation by electrostatic stabilization of 1,2 intramolecular carbon shift with respect to 1,2 intramolecular hydride transfer. Experimental studies revealed an improvement in the conversion of glucose when methanol solvent was used instead of water, due to the difference in solvation of the hydrophobic pores of zeolites. Lengthy crystallization synthesis procedure is a key concern for the large-scale production of Sn-zeolites.[72] To overcome this problem, a feasible, direct hydrothermal procedure was developed for the incorporation of Sn into the germanosilicate framework of a BEC zeolite. The synthesis time required for Sn-BEC is tenfold shortened than that for the traditional Sn-zeolites. The developed Sn-BEC zeolite displayed higher activity and excellent selectivity for glucose isomerization, attributed to homogenous distribution of Sn sites. In contrast, Sn-β promoted both isomerization and epimerization reactions.

5-Hydroxymethylfurfural (HMF) is a vital platform molecule for future biorefineries. The conversion of glucose to HMF (Fig. 8) involves glucose isomerization to fructose (Lewis acid catalyzed step) and its subsequent dehydration to HMF (Brønsted acid catalyzed step). It is obvious that glucose-to-HMF transformation requires both Lewis and Brønsted acid sites. An overview of the most significant catalytic results achieved in liquid phase carbohydrates-to-HMF transformation over porous catalysts is presented in Table 1. The conversion of glucose to HMF in liquid phase was investigated using various ZSM-5 based zeolites (H-, Fe- and Cu-ZSM-5).[73] About 80% glucose conversion with 42% HMF yield was obtained over H-ZSM-5, which was attributed to optimum molar ratio of Lewis/Brønsted acidity (entry 1, Table 1). The importance of Lewis–Brønsted acidity for glucose-to-HMF transformation was also observed over Al-rich β zeolites (entry 2, Table 1),[74] [Sn, Al]-β zeolites (entry 3, Table 1)[75] and H-β-25 zeolite.[76] For fructose dehydration, narrow pore zeolites exhibited superior HMF selectivity (about 90%) at 85–94% fructose conversions (entry 4, Table 1), whereas larger pore zeolites promoted undesirable HMF oligomerization towards humins production.[77] Owing to strong acid properties, HY zeolite was found to be active for fructose-to-HMF transformation.[78] The subsequent hydrogenation of HMF to 2,5-dihydroxymethylfuran or 2,5-dimethylfuran was performed using a $Cu/ZnO/Al_2O_3$ catalyst. One-pot synthesis of 5-ethoxymethylfurfural (EMF) from glucose involves multiple steps as shown in Fig. 8. EMF is a potential next-generation biofuel with a high energy density (8.7 kilowatt-hours per litre, kW h L^{-1}), greater than that of bioethanol (6.1 kW h L^{-1}) and comparable to that of gasoline (8.8 kW h L^{-1}) and diesel (9.7 kW h L^{-1}).[79,80] EMF can be transformed to 5-ethoxymethylfurfuryl alcohol (a promising diesel additive) and to esters of 2,5-furandicarboxylic

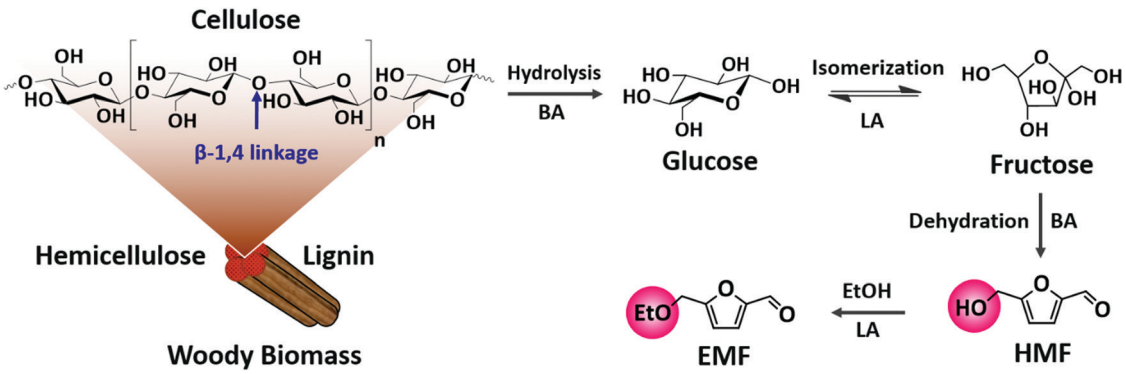

Fig. 8 Upgrading cellulose into various high-value products: glucose, fructose, 5-hydroxymethylfurfural (HMF) and 5-ethoxymethylfurfural (EMF): BA – Brønsted acid and LA – Lewis acid.

Table 1 Liquid phase carbohydrates-to-HMF transformation over porous catalysts

Entry	Catalyst	Biomass substrate	Reaction conditions	Catalytic activity		Key factors for the catalyst activity	Ref.
				Conv. (%)	Yield (%)		
1	H-ZSM-5 zeolite	Glucose	3 : 1 wt% of glucose : catalyst, H_2O/MIBK[a], 195 °C, 30 min	80	42	Optimum amounts of Lewis–Brønsted acid sites	73
2	Al-rich beta zeolite[b]	Glucose	0.1 g catalyst, 0.67 mmol glucose, H_2O, DMSO[c], THF[d], 180 °C, 3 h	86	56	Optimum amounts of Lewis–Brønsted acid sites	74
3	[Sn,Al]-beta zeolite	Glucose	0.05 g catalyst, 10 wt% glucose solution, DMSO, 160 °C, 4 h	60	37	Suitable Sn/Al molar ratio and optimum amounts of Lewis–Brønsted acid sites	75
4	ZSM-5 zeolite	Fructose	0.033 g catalyst, 1 g fructose, 190 °C, 80 min, H_2O-MIBK mixture	85	74.8	Narrow pore dimensions	77
5	Mesoporous AlSiO-20	Glucose	0.2 g catalyst, 0.2 g glucose, THF/H_2O–NaCl, 160 °C, 90 min	91.7	63	High BET surface area and suitable ratio of Brønsted/Lewis acidity	178
6	10Al-MCM-41 silica	Glucose	0.05 g catalyst, 0.15 g glucose, 195 °C, 30 min, $NaCl_{aq}$/MIBK	96	63	Mesoporous structure and optimum amounts of acid sites	185
7	Functionalized hierarchical porous SiO_2	Cellulose	0.04 g catalyst, 120 °C, 30 min, DMSO/H_2O	—	44.5	Hierarchical porous structure, high BET surface area, and abundant acid–base sites	193
8	Nafion/mesocellular SiO_2[e]	Fructose	Catalyst (acid amount: 0.06 mmol H^+), fructose in DMSO (3 wt%, 12.5 g), 90 °C, 2 h	94	89.3	Strong acid strength and open ultra-large pore system	211
9	Sulfated MCM-41 silica	Fructose	0.033 g catalyst, 1 g fructose, 190 °C, 80 min, H_2O-MIBK mixture	94	84.6	Mesoporous structure and weak acidity	77
10	Sulfated KIT-5 silica	Fructose	0.04 g catalyst, 1 mmol fructose, DMSO, 125 °C, 45 min	—	94	Brønsted acid sites	233

[a] MIBK – methyl isobutyl ketone. [b] Calcination at 500 °C. [c] DMSO – dimethyl sulfoxide. [d] THF – tetrahydrofuran. [e] 15 wt% Nafion loading.

acid (an ideal alternative to terephthalic acid for the polymer industry). The dealuminated β zeolite gave reasonably good yields of EMF (37%) from glucose.[81] Interestingly, the combination of H-form zeolite and Amberlyst-15 led to efficient transformation of glucose to EMF (46%). The production of EMF from various mono-, di- and poly-saccharides was also examined in this work. The acidity, adsorption ability, and the internal pore dimensions of zeolites were the crucial factors for the etherification of HMF with isobutene to produce *tert*-butoxymethylfurfural.[82] HY zeolite with a SiO_2/Al_2O_3 mole ratio of 12 is highly selective towards bio-ether product (94%) at 59% HMF conversion. A simple calcination step in air was performed to regenerate the catalyst activity for the next cycle.

Acid-catalyzed dehydration of C5 sugars, such as xylose and arabinose gives furfural, a very important chemical for the production of fuel additives and polyester monomers.[83–85] Cui *et al.*[83] indicated that the co-operative interaction of Hβ zeolite with γ-butyrolactone–water solvent system enables both selective C–C bond cleavage of acyclic hexoses into pentoses and the subsequent dehydration into furfural. The obtained furfural yields from fructose, glucose, and cellulose were 63.5, 56.5, and 38.5%, respectively. Both Lewis and Brønsted acid sites in Sn–Al-β zeolite are essential for the catalytic transfer hydrogenation and hydrolysis of furfural to γ-valerolactone.[86] The degree of dealumination and Sn-incorporation significantly influenced the acid properties of zeolite and consequently its catalytic efficiency. Magnetically recoverable β-zeolites exchanged with transition metals (Pd, Fe and Ir) were demonstrated to be catalytically active for upgrading furfural and furfuryl alcohol into bio-based chemicals.[87] Particularly, Pd-exchanged zeolite showed the best catalytic performance towards isopropyl levulinate production from both furfural and furfuryl alcohol. H-ZSM-5 zeolite is a versatile catalyst for the transformation of furfural to indoles *via* thermo-catalytic route, followed by ammonization.[88] A possible reaction pathway was proposed in which furfural initially reacts with NH_3 to give furfural-imine, subsequent cracking to furan, followed by its conversion to pyrrole and finally to indole. H-ZSM-5 zeolite can also efficiently catalyze furfuryl alcohol hydrolysis to obtain levulinic acid (LA).[89] The remarkable hydrophobic nature of H-ZSM-5 alters the internal solvent microenvironment within the zeolite framework to achieve more than 70% yields of LA. Mahmoud *et al.*[90] studied Diels–Alder reaction of furan and methyl acrylate (or acrylic acid) using Lewis acidic zeolites (Hf-, Zr-, and Sn-β). All zeolites selectively catalyze the thermodynamically controlled reaction of furans with acrylates with higher turnover frequencies compared to other homogeneous and heterogeneous Lewis acid catalysts. The resulting product *i.e.* oxanorbornene was dehydrated to produce methyl benzoate in the presence of methanesulfonic acid and acetic anhydride. The integrated reduction-acid conversion of furfural to valuable bio-products was carried out over a β zeolite possessing Zr and Al sites.[91] The existence of Zr-sites was crucial for initiating the reduction of furfural to furfuryl alcohol as well as for the reduction of alkyl levulinate esters to γ-valerolactone. The co-presence of Al-sites promoted acid-catalyzed steps. DFT calculations suggested

three types of reaction pathways for H-ZSM-5 catalyzed furfural decarbonylation to form furan product.[92] Among them, the protonation of α-carbon to the arenium-ion like intermediate was found to be the preferred pathway for furfural decarbonylation as this pathway requires low activation energy for the rate-determining step. Owing to well-balanced strong Lewis acid sites and an optimal pore size, H-β-zeolite was able to catalyze the transformation of γ-valerolactone to ethyl-4-ethoxy pentanoate, a potential bio-ether fuel.[93] About 86% product yield with 97% selectivity was obtained at optimized reaction conditions. The vapor phase decarbonylation of lactic acid to acetaldehyde was investigated using HMCM-22, HZSM-5 and NaZSM-5 zeolites.[94] Interestingly, the NaZSM-5 zeolite, which contains intermediate strength of Lewis acid sites (Brønsted/Lewis acid sites ratio is 0.4) is highly selective towards acetaldehyde production (yield of acetaldehyde + CO = 96%) by suppressing the formation of lactic acid oligomers and coke (Fig. 9). In contrast, the strong Brønsted acidic zeolites (HMCM-22 and HZSM-5) gave only 39.7% and 57% yields of decarbonylation products (acetaldehyde + CO), respectively, because of the formation of considerable amounts of lactic acid oligomers.

2.2.3 Upgrading of glycerol and its derivatives. Glycerol is obtained as a byproduct (approximately 10 wt%) during biodiesel synthesis *via* catalytic transesterification of triglycerides (oils and fats) with methanol (Fig. 10). Hence, valorizing waste glycerol to value-added products has received a lot of attention for a more sustainable biodiesel industry. Advanced fuel additives can be produced *via* etherification of glycerol with ethyl and *tert*-butyl alcohols in the presence of zeolite-based catalysts (Hβ, USY, and HZSM-5).[95] Results revealed the beneficial role of both Lewis and Brønsted acid sites for glycerol etherification. Hence, USY-650-L-2 (prepared by two consecutive steaming cycles at 650 °C followed by acid leaching) and Hβ zeolite afforded about 70% glycerol conversion with a high selectivity to mono- and di-substituted ethers. Isomerization of dihydroxyacetone (produced by partial oxidation of glycerol) and xylose was strongly dependent on the framework structure and the preparation method of Sn-zeolites (MFI, MOR, BEA, and FAU).[96] Owing to relatively higher amounts of tetrahedral Sn sites and facile mass transfer properties, BEA and FAU zeolites were found to be highly active in aqueous- and, particularly, in methanol based reactions. Moreover, improved turnover frequencies were obtained in the case of hydrothermally prepared zeolites than those obtained by a post-synthetic approach, which

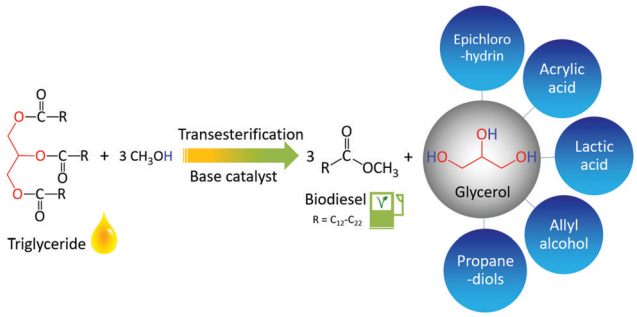

Fig. 10 Catalytic transformation of triglycerides (oils and fats) to produce biodiesel with glycerol as a byproduct, which can be upgraded to a variety of drop-in chemicals.

was attributed to high quality Sn species and greater hydrophobicity of hydrothermally prepared zeolites. For the conversion of 1,3-dihydroxyacetone into ethyl lactate, Brønsted acidic sites (compared to Lewis acidic sites) present in Al-containing Snβ zeolites are more favorable for promoting the rate-determining dehydration of 1,3-dihydroxyacetone into pyruvic aldehyde.[97] Zeolites having moderate amounts of Al (0.3 wt% Al) provided the highest ethyl lactate yields. Zeolites have also been successfully used for glycerol dehydration to acrolein (an acid-catalyzed reaction), a key intermediate for the production of various commodity chemicals, such as acrylic acid, acrylates, acrylonitrile, and acrylamide.[98] Several zeolites, such as HZSM-5, H-ferrierite, HZSM-11, MCM-22, ZSM-23, mordenite, and HY zeolite were evaluated for glycerol-to-acrolein transformation in liquid phase.[99] A high selectivity of 99.5% at 89% glycerol conversion was obtained over HY zeolite after 10 h reaction time. Fast catalyst deactivation elicited by severe mass transfer limitations is the major constraint for using microporous zeolites for several biomass upgrading reactions including glycerol valorization. It has been recently demonstrated that catalyst deactivation and mass transfer problems could be solved by use of hierarchical zeolites.[100–102]

2.2.4 Renewable benzene, toluene and xylene production. Furans, such as 2-methylfuran and 2,5-dimethylfuran are advanced platform molecules that can be obtained by acid-catalyzed hydrolysis of (hemi)cellulose and subsequent dehydration reaction. These furans can be converted into valuable aromatics, such as benzene, toluene, and xylenes (BTX), which have very important applications in chemical industry. The acidic nature of the zeolites has a profound effect on the conversion of 2-methylfuran and BTX selectivity.[103] For instance, strong Lewis acidic

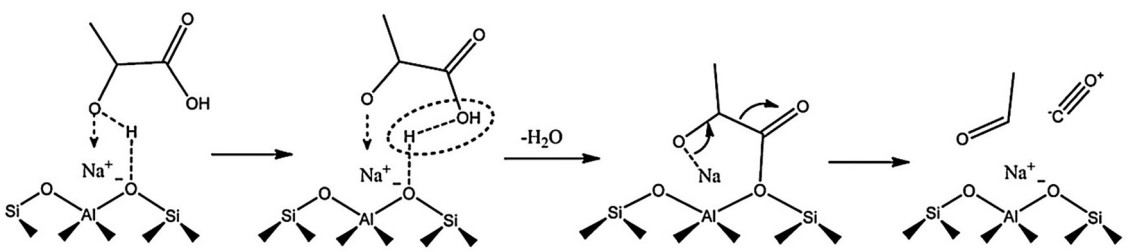

Fig. 9 Probable reaction mechanism for the decarbonylation of lactic acid to acetaldehyde over Na-ZSM5 zeolite. Reproduced with permission from ref. 94. Copyright (2018) Elsevier.

Na-Y zeolite is selective towards toluene formation, while Brønsted acidic zeolites (H-β and H-Y) were proven to be effective for the conversion of 2,5-dimethylfuran to *p*-xylene. This is because Brønsted acidic zeolites can promote side reactions of 2-methylfuran, resulting in lower selectivity of toluene. Lewis acidic zeolites, such as Zr-, Sn-, and Ti-BEA were examined for *p*-xylene production *via* liquid phase tandem [4+2] Diels–Alder cycloaddition of 2,5-dimethylfuran and ethylene to oxanorbornene, followed by a dehydration step.[104] A high selectivity (90%) to *p*-xylene at full conversion of 2,5-dimethylfuran was found over Zr-BEA catalyst, which can strongly suppress the side reactions (hydrolysis and subsequent condensation step) of 2,5-dimethylfuran. Teixeira *et al.*[105] developed an efficient liquid phase catalytic protocol for the synthesis of *p*-xylene from 2,5-dimethylfuran and ethanol using H-USY and H-ZSM-5 zeolites. The proposed reaction pathway involves the *in situ* dehydration of ethanol to ethylene, followed by Diels–Alder cycloaddition of 2,5-dimethylfuran with ethylene to yield *p*-xylene. Particularly, HUSY-12 zeolite with an intermediate acidic content (Si/Al = 6) provided the highest carbon yield for aromatics, due to the existence of a preferred porous structure in HUSY-12 zeolite.

2.2.5 Upgrading of lignin-derived compounds. Lignin, with an annual production of approx. 50 billion tons *via* photosynthesis process, is an abundantly available renewable feedstock for the production of aromatics and their derivatives (Fig. 11).[18] Hence, valorization of lignin and its derived compounds for chemicals synthesis is a hot research topic in the field of lignocellulose biorefinery. Bisphenols, typically synthesized by condensation of phenols with ketones in the presence of hazardous liquid acids (*e.g.*, HCl) or unrecyclable sulfonated resins, are vital precursors for the production of polycarbonate plastics. Ferrini *et al.*[106] developed an efficient liquid phase catalytic route for the synthesis of bio-based bisphenols *via* condensation of lignin-derived compounds (*e.g.*, 4-methylguaiacol) with formaldehyde using zeolite-based catalysts. Particularly, FAU 40 zeolite exhibited high catalytic performance (turnover frequency of 496 h^{-1}) with >95% selectivity to bisphenol A alternatives. The catalytic versatility of FAU 40 zeolite was also demonstrated for the conversion of other lignin-derived molecules to produce bio-based bisphenols. Yuhe *et al.* investigated the steam-assisted gas phase dealkylation of lignin-derived compounds, such as 4-*n*-propylphenol[107] and 4-ethylphenol[108] over a variety of acidic zeolites, including ferrierite, ZSM-22, ZSM-5, beta, and USY, along with several metal oxides (ZrO_2, MgO, ZnO, and Al_2O_3). Both Brønsted and Lewis acidic sites play a key role in dealkylation of lignin-derived compounds to obtain phenol and alkenes. Among those, medium-pore zeolite ZSM-5 was found to be highly selective towards phenol and alkene production because of its excellent pore confinement property that avoids undesired side reactions. Owing to high heat of adsorption (32–40 kJ mol^{-1}) compared to that of phenol (10 kJ mol^{-1}), water prevents the formation of dehydrated products in the pores of ZSM-5, and hence, improved catalyst durability in dealkylation of lignin-derived compounds. In the case of gas phase alkylation of *m*-cresol (lignin-derived compound) with iso-propanol, Zn-loaded HY zeolite gave about 92% *m*-cresol conversion with a high selectivity to thymol product, which was attributed to well-balanced strong Lewis/moderate Brønsted acidic sites and unique three dimensional pore structures.[109] On the other hand, Hβ zeolite was more prone to deactivation by means of coking and pore blocking. Large-pore zeolites (faujasite-type) are the most suitable catalysts for co-cracking of 2-ethylphenol and *n*-decane.[110] In contrast, medium-pore zeolites and β zeolite are only active for *n*-decane cracking, but suffered with rapid deactivation during co-cracking of *n*-decane and 2-ethylphenol. The strong ability of catalyzing H-transfer reaction made the faujasite zeolite the choice of best catalyst for fluid catalytic cracking reactions.

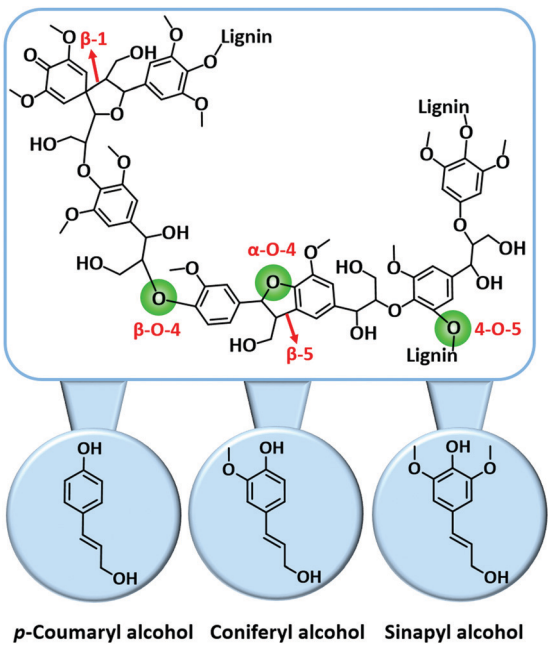

Fig. 11 Key C–O and C–C linkages in lignin and its key building blocks. Adapted with permission from ref. 18. Copyright (2018) Royal Society of Chemistry.

2.2.6 Upgrading of biomass-derived hydrocarbons and alcohols. In this section, upgrading of biomass-derived hydrocarbons and alcohols is mainly discussed. Selective removal of 1,2-propanediol (1,2-PDO) and 1,2-butanediol (1,2-BDO) impurities produced during bio-ethylene glycol synthesis is critical for its full exploitation in chemical industry. To address this issue, a selective dehydration step catalyzed by zeolites was realized, which can convert 1,2-PDO and 1,2-BDO to volatile aldehydes, ketones, and acetals in liquid phase.[111] Micropores of H-β zeolite provide the active sites *i.e.* Brønsted acid sites for the selective dehydration of a mixture containing 73 wt% ethylene glycol, 20 wt% 1,2-PDO, and 7 wt% 1,2-BDO, resulting in 99% and 99.3% conversions of 1,2-PDO and 1,2-BDO, respectively. At the same time, the presence of strong acid sites enhanced the polymerization of ethylene glycol. Both HZSM-5 and SAPO-34 zeolites were found to be promising for the gas phase dehydration of mixed alcohols (*i.e.*, ethanol, 1-propanol, 1-butanol and 2-methyl-1-propanol) to valuable olefins, outperforming the mesoporous SiO_2 based catalysts.[112] This obviously

suggests that Brønsted acidic catalysts are more active than Lewis acidic catalysts for alcohol dehydration. An organosilane-modification strategy was attempted to tune the hydrophobic nature of ZSM-5 zeolite.[113] The resulting zeolite afforded 10-fold higher catalytic activity for the aqueous phase dehydration of alcohols to olefins compared with a conventional ZSM-5 catalyst. This is because the hydrophobic surface of ZSM-5 could enrich the alcohol substrate and keep water away from the acid sites (active sites for dehydration reaction), giving improved reaction rates. A bimetallic InV-ZSM-5 zeolite was employed for the conversion of bio-ethanol to hydrocarbons without using an external hydrogen source.[114] The C_2H_5OD and *in situ* DRIFT studies proposed a hydrocarbon pool-type mechanism, revealing that the dehydration step is not necessary for the production of hydrocarbons from ethanol.

Incorporation of boron had a considerable effect on the acidity of zeolites: the amount of weak acid sites increases proportionally with the amount of incorporated boron.[115] Borosilicalite-1 zeolites synthesized in the presence of alkali hydroxide were catalytically more active in steam catalytic cracking of dodecane due to the formation of an active trigonal coordination system (boron site). The structure–activity properties of four different zeolites, namely MCM-22, MCM-49, MCM-56 and Ce/MCM-22, before and after water treatment, were investigated in the liquid phase tetrahydropyranylation of *n*-propanol or *tert*-butanol with 3,4-dihydro-2*H*-pyran.[55] Water treatment of zeolites at 160 °C for 48 h caused a reduction in both acid site concentration and micropore volume. Except for Ce/MCM-22, all zeolites showed higher catalytic performance in the tetrahydropyranylation of alcohols. Low activity of Ce/MCM-22 was due to the pore blockage by Ce species. The HZSM-5 framework remains unaffected after alkali treatment (NaOH), with a favorable improvement in the pore size and acidity at low NaOH concentrations (<0.5 M).[116] On the other hand, the zeolite structure can be degraded with a significant reduction of micropore size and acidity concentration at higher NaOH concentrations. Results obtained from gas phase oligomerization of biomass-derived ethylene revealed that the proper NaOH treatment not only favors ethylene conversion and product yield, but also improves catalyst stability. The selective aldol condensation of acetaldehyde to C_4 products was examined over NaX and NaY zeolites in liquid phase.[117] Effects of several parameters, such as number and location of exchangeable cations, nature of cations, and post-synthesis modifications were studied towards product selectivity. NaY catalyst displayed higher $C_4/(C_6 + C_8)$ product ratio than NaX, attributed to the presence of optimized basic sites in NaY catalyst.

The acidic sites strength in HZSM-5 based zeolites exhibited a significant effect in the gas phase conversion of bio-ethanol to propylene, which is an important starting chemical for the synthesis of propylene oxide and polypropylene.[118,119] For instance, medium strength acid sites favor the formation of propylene, while weak acid sites are selective towards ethylene formation.[118] On the other hand, strong acid sites promote the formation of other paraffins, C_{5+} aliphatics, and aromatics. The highest yield of propylene obtained over HZSM-5 with Si/Al_2 ratio of 80 was 32%. However, this zeolite suffered from severe catalytic deactivation after 4 h time-on-stream study. Doping of HZSM-5 with zirconium was suggested to improve its stability for propylene production. In another work, a hydrothermally synthesized HZSM-5/SAPO-34 composite was found to show high propylene yield and improved catalytic stability than the parent HZSM-5 and mechanically mixed HZSM-5/SAPO-34 in gas phase ethanol-to-propylene transformation.[120] Interestingly, a high yield of propylene (~50%) was achieved over a β zeolite-In_2O_3 composite, while pure In_2O_3 provided only 32% propylene yield.[121] The improved catalytic performance of β zeolite-In_2O_3 composite was attributed to the promoting role of β zeolite in the conversion of acetone intermediate to propylene *via* an additional reaction pathway. The conversion of bio-ethanol to butadiene is an industrially important process, aiming at bio-based production of butadiene rubber. Butadiene synthesis from ethanol is a complex cascade reaction that typically requires well-balanced amounts of catalytic active sites.[122,123] Promising results in terms of butadiene production were achieved over Zr-containing β zeolites doped with 1 wt% Ag, particularly over the catalyst prepared using a post-synthesis method.[124] The presence of $Zr(OSi)_3OH$ open sites (Fig. 12) with high Lewis acidity is key for improved conversion of ethanol to butadiene in continuous-flow conditions. As a result, Ag/Zr-β zeolite (Si/Al ratio of 75 in parent zeolite and 3.5 wt% Zr) afforded higher production rate of butadiene (3 μmol g^{-1} s^{-1}).

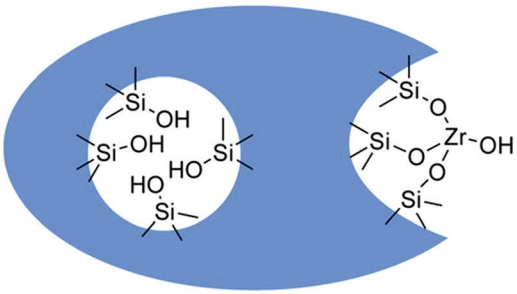

Fig. 12 Schematic representation of Zr grafting by treatment of dealuminated zeolites with $ZrOCl_2$ in DMSO. Reproduced with permission from ref. 124. Copyright (2016) John Wiley and Sons.

2.3 Zeolite-supported catalysts

The presence of unique pore dimensions and structures allow the zeolites to accommodate a wide range of catalytically active metals and metal oxides. This adds multifunctional properties to the final catalytic materials with synergistic interactions, which may have important applications in biomass conversion.

2.3.1 Catalytic fast pyrolysis of biomass. The catalytic fast pyrolysis (CFP) of palm kernel shell with a high lignin content (50 wt%) was studied using H-β and Fe/H-β catalysts.[125] The Fe active sites promoted the deoxygenation of lignin-derived phenolics during CFP of palm kernel shell. However, both H-β and Fe/H-β catalysts gave nearly similar hydrocarbon yields from cellulose. Sun *et al.*[126] performed a comparative study of CFP processing of wood sawdust over ZSM-5 and Fe/ZSM-5 catalysts. The Fe/ZSM-5 catalyst provided higher yields of monocyclic

aromatic hydrocarbons (MAHs) than the pure ZSM-5 catalyst. The incorporated Fe species in ZSM-5 zeolite are the selective active sites towards MAHs formation and concurrently suppressed the further polymerization of MAHs and other oxygenates. HZSM-5 supported bimetallic Co–Mo catalysts were found to be promising for the CFP of prairie cordgrass to hydrocarbon biofuels in a two-stage reactor system.[127] This CFP process considerably improved the water content, chemical composition, heating value, viscosity, and the density of bio-oils compared to non-catalytic method. Among the catalysts examined, a maximum 41% hydrocarbon yield was achieved with 2%Co–4%Mo/HZSM-5 catalyst. For catalytic upgrading of pine pyrolysis vapors, improved conversion rates and higher yields of aromatic hydrocarbons were attained over Ni/ZSM-5 catalyst compared to pure zeolite, which are more pronounced with the increase of Ni loading.[128] Remarkably, similar kinds of Ni active species formed by the pre-reduction treatment of the catalyst are also generated during the reaction. Reason is that biomass pyrolysis vapors are able to induce the *in situ* reduction of NiO to Ni. Hence, pre-reduction of Ni/zeolite catalysts is unnecessary for this CFP process.

2.3.2 Upgrading of carbohydrates and their derived compounds. A continuous-flow process by means of a zeolite supported metal catalyst was developed for the direct conversion of cellulose to C_3 + C_4 hydrocarbons without using hydrogen or other expensive reagents.[129] Pt supported on NH_4^+-form ultra-stable Y-type (NH_4-USY) zeolite afforded 14.5 C-% yield of C_3 + C_4 hydrocarbons. The acidic strength of the zeolite as well as Pt particle size were the main factors favorably affecting the cellulose conversion and the reaction rates. The conversion of glucose to levulinic acid in aqueous phase was highly dependent on the loading of Fe (5, 10, and 15 wt%) in Fe/HY zeolite.[130] Particularly, the 10% Fe/HY catalyst gave the highest yield (62%) of levulinic acid, which was attributed to larger BET surface area, high concentration of acid sites, and suitable Brønsted/Lewis acidity. This catalyst was reused for five cycles without much loss in catalytic activity. Higher amounts of humins were also formed over the catalysts having excess amount of Lewis acid sites. This 10% Fe/HY zeolite was also found to be effective for the conversion of oil palm fronds to levulinic acid in aqueous phase and the leaching of Fe was negligible after the reaction.[131] VO_x supported on Si-rich mordenite (MOR) zeolite is a versatile catalyst to valorize a variety of carbohydrates (*e.g.*, glucose, sucrose, inulin, raffinose, maltose, and starch) into 2,5-diformylfuran using molecular oxygen in DMSO–HCl solvent system.[132] The catalytic performance of V_2O_5@MOR zeolite is ascribed to unique structure of MOR zeolite that enabled the formation of high dispersion of isolated tetrahedrally coordinated $[V_2O_8]^{6-}$ active species and optimum concentration of acid sites.

Modification of HZSM-5 using a mesoporous silica (MCM-41) was attempted to improve its porous structure and acidity and consequently the catalytic efficiency of Ni/HZSM-5 for the transformation of sorbitol into aromatic compounds in gas phase.[133] The acid sites of zeolite and its shape selectivity promoted the dehydration and aromatization of sorbitol, whereas Ni metal centres catalyzed the hydrogenation and cracking steps. The catalyst acidity determines the carbon distribution of products, resulting in 66.3% carbon yield in aromatic compounds at full conversion of sorbital. For the hydrogenation of ethyl levulinate, the 1% Pt/ZSM-35 catalyst provided 100% ethyl levulinate conversion and 99% γ-valerolactone selectivity, outperforming Pt catalysts supported on SAPO-34, ZSM-35, ZSM-5, HY, USY, and MOR zeolites.[134] Abundant metallic Pt NPs and optimum surface acidity of ZSM-35 were the primary reasons for achieving high yields of γ-valerolactone. The synergistic effect of metal sites and zeolite acid sites was also observed in Zn/ZSM-5 catalysts for the conversion of γ-valerolactone to aromatic compounds.[135] A Cu–MOR zeolite, synthesized by a one-pot template-free route, was used as an efficient support for stabilizing vanadium oxide species.[53] The investigated aerobic oxidation of HMF over the $10V_2O_5$@Cu–MOR(125) catalyst demonstrated a high yield of 2,5-diformylfuran (91.5%) and excellent catalyst reusability performance (entry 1, Table 5). The synergy between the guest V sites and the framework Cu species contributed to the exceptional performance of $10V_2O_5$@Cu–MOR(125) catalyst in the liquid phase oxidation of HMF. Owing to high dispersion of Ru NPs on NaY zeolite, the 2 wt% Ru/NaY catalyst displayed about 78% yield of 2,5-dimethylfuran at nearly 100% HMF conversion during liquid phase HMF hydrogenation (entry 1, Table 4).[136] Furthermore, no considerable loss in HMF conversion and 2,5-dimethylfuran yield was found even after fifth recycle of the catalyst. Pd NPs encapsulated inside of silicalite-1 zeolite (Pd@S-1-OH) exhibited high selectivity to furan (>99.9%) at complete conversion of furfural, outperforming the conventional Pd/zeolite catalysts (entry 1, Table 3).[137] This superior catalytic efficiency was due to the controlled diffusion of molecules within the hydrophilic micropores of zeolite, enabling efficient adsorption of furfural and by-products as well as facile diffusion of furan product.

2.3.3 Upgrading of lignin-derived compounds. Lignin-derived bio-oil obtained *via* catalytic fast pyrolysis can contain highly oxygenated species, which can adversely affect bio-oil properties, including heating value and chemical/thermal stability.[138,139] Catalytic hydrodeoxygenation (HDO) using a hydrogen source and a multifunctional catalyst is a viable strategy to remove the chemically bonded oxygen from lignin-derived oil, enabling its use directly or in combination with a petroleum fraction. Both metallic and acidic sites are essential for the efficient HDO of lignin-based model compounds, as shown in Table 2. For instance, the synergy between the Pt reducibility and the acid strength of H-MFI-90 zeolite elicited the selective cleavage of guaiacol to obtain cyclohexane (93% yield) in liquid phase (entry 1, Table 2).[138] A probable HDO mechanism involving a hydrogenation step (on metal sites), followed by an acid-catalyzed dehydration combined with a hydrogenation step was proposed in this work. Wang *et al.*[139] developed a hydrogen-free process for the conversion of phenol into fuel grade chemicals over TiO_2–CeO_2/ZSM-5 catalyst under both ultrasound and ultraviolet conditions. The ZSM-5 structure remains unaffected after modification, and the Ti and Ce

Table 2 Hydrodeoxygenation of lignin model compounds over porous and nanoscale catalysts

Entry	Catalyst	Reactant	Reaction conditions	Product	Catalytic activity		Key factors for the catalyst activity	Ref.
					Conv. (%)	Yield (%)		
1	1 wt% Pt/H-MFI-90	Guaiacol	Liquid phase, 0.05 g catalyst, 2 mmol substrate, *n*-hexadecane, 180 °C, 5 h, 50 bar H_2	Cyclohexane	100	93	Pt reducibility and acidic strength of zeolite	138
2	Fe–Ni/H-beta	Anisole	Vapor phase, 0.1 g/min feeding rate, 18 g catalyst, 0.32 L min^{-1} flow rate of H_2, 350 °C	BTX[a]	100	24.9	Pore size, BET surface area, and acid sites	140
3	5 wt% Ni/Ce-SBA-15[b]	Anisole	Vapor phase, H_2/feedstock ratio (300 Nm^3 m^{-3}), 290 °C, 7 bar H_2, WHSV[c] (163.2 h^{-1}), 6 h	Benzene	7.9×10^3 (TOF, s^{-1})[d]	—	High metal dispersion and specific Ni sites in contact with Ce surface species	174
4	5 wt% Ni/Al-SBA-15	Anisole	Liquid phase, 50 mL of a solution containing 3 wt% anisole, 220 °C, 50 bar H_2, 2 h	Cyclohexane	99.8	95	Acidity of support and synergy of metallic and acid sites	226
5	CuNi/Ti-MCM-41	Guaiacol	Liquid phase, 0.1 g catalyst, 3 wt% guaiacol of heptane, 100 bar H_2, 260 °C, 6 h	Cyclohexane	90	45	Abundant acid/redox sites and high metal dispersion	228
6	Co/Al-MCM-41	Guaiacol	Vapor phase, 1 atm, 1.67 h contact time, 30 min, 300 °C H_2/guaiacol molar ratio = 25	Phenol	96	39	Optimum amounts of acid and metal sites	229
7	MoO_3	phenol	Liquid phase, 1 g catalyst, octane, 340 °C, 5 bar H_2 + 30 bar N_2	Benzene	98	97	Oxygen vacancies in MoO_3	392
8	10.5 wt% MoO_x/Al_2O_3	*m*-Cresol	Liquid phase, 0.12 g catalyst, 340 °C, 40 bar H_2	Toluene	20 ± 1 (TOF, h^{-1})	—	Reducibility of Mo species	394
9	10 wt% Co/TiO_2	Eugenol	Liquid phase, 1 mmol eugenol, 0.065 g catalyst, *n*-dodecane, 10 bar H_2, 200 °C, 2 h	Propylcyclohexanol	100	99.9	High dispersion of Co and strong metal–support interaction	395
10	0.4 wt% Pt/20Nb–Al_2O_3	Diphenyl ether	Vapor phase, W/F = 15.2 min, 0.05 g catalyst, 30 bar H_2, H_2/oil = 300, 240 °C	Cyclohexane	100	99.2	Abundant water-tolerant Lewis acid sites	397
11	NiCo[e]/γ-Al_2O_3	Guaiacol	Liquid phase, 5 g guaiacol, 45 g water, 2 wt% of catalyst, 8 h, 200 °C, 50 bar initial H_2	Cyclohexanol	96	65.2	High acidity and strong metal–support interaction	398
12	$Ti_{2.0}Pd/SiO_2$	Guaiacol	Vapor phase, 0.20 g catalyst, 3 wt% guaiacol in *n*-dodecane, 300 °C, 20 bar H_2	Cyclohexane	100	80	Smaller Pd particles and high deoxygenation activity of TiO_2	400
13	Ru[f]/ZrO_2–$La(OH)_3$	Guaiacol	Liquid phase, 5 mmol guaiacol, 0.10 g catalyst, H_2O, 40 bar H_2, 4 h	Cyclohexanol	100	91.6	High metal dispersion and basic strength of the support	403

[a] BTX – benzene, toluene, xylene. [b] Ce/Si = 0.03. [c] WHSV – weight hour space velocity. [d] TOF – turnover frequency. [e] Ni : Co = 1 (20 wt% total loading). [f] Ru = 5 wt% and Zr : La = 2.

are partly incorporated into the zeolite structure. Several reaction conditions, such as temperature, pressure, space velocity, and phenol/catalyst ratio were optimized. The phenol conversion reached 98.5% with 50% and 44% yields of gasoline and diesel oil, respectively. Bimetallic Fe-Ni catalysts supported on three types of zeolites (Hβ, ZSM-5, and HY) were found to show good catalytic activities in the gas phase HDO of anisole to BTX (benzene, toluene, and xylene).[140] Results indicated the significance of pore size, BET surface area, and acid sites for the product distribution. The Fe-Ni/Hβ catalyst (Ni = 10.82% and Fe = 8.64%) gave a 24.9% yield of BTX at 100% anisole conversion, while the Fe-Ni/ZSM-5 catalyst promoted the transalkylation pathway (entry 2, Table 2). Interestingly, the strong adsorption of phenol molecules on the acid sites of Hβ and Fe/Hβ zeolites led to higher amounts of coke and rapid catalyst deactivation during continuous flow deoxygenation of phenol and *m*-cresol, which could be prevented by increasing the reaction temperature.[141]

2.3.4 Glycerol valorization. The chemoselective conversion of glycerol into value-added chemicals was carried out in gas phase using ZnO modified Sn/HZSM-5 catalysts prepared by atomic layer deposition (ALD) and incipient wetness impregnation methods.[142] The presence of Zn species allowed the conversion of alkenes, derived from deoxygenation of glycerol, into aromatics through dehydrogenation reaction. The 20 ALD cycles facilitated the formation of a precise ZnO thin film, which not only stabilized the oxidation state of active SnO_x species, but also improved the aromatization activity, catalyst lifetime, and reusability compared with the results obtained over ZnO impregnated Sn/HZSM-5 catalyst. However, when the ALD cycle number reached 40, the ZnO film could block the Sn active sites in Sn/HZSM-5, leading to reduction in both aromatics yields and catalyst lifetime. Priya *et al.*[143] demonstrated a noticeable effect of Cu loading on the performance of Pt–Cu/H-mordenite catalysts for the vapor phase hydrogenolysis of glycerol. Owing to highly dispersed Pt–Cu particles, synergistic metal–support interaction and strong Brønsted acidity of H-mordenite, about 90% and 58.5% of glycerol conversion and 1,3-propanediol selectivity, respectively, were attained over the 2%Pt–5%Cu/H-mordenite catalyst (entry 1, Table 6).

2.3.5 Upgrading of other biomass-derived compounds. A variety of Pt/zeolite catalysts were screened for the liquid phase hydrocracking of biomass-derived compounds (n-$C_{28}H_{58}$ and n-$C_{36}H_{74}$) to obtain jet fuel.[144] Several parameters, such as reaction pressure, reaction temperature, and Pt content were optimized for enhancing hydrocracking activity of Pt/β-type zeolite catalyst, which afforded good yields of jet fuel from both model compounds. Bimetallic Au–Pd NPs encapsulated within S-1 zeolite crystals were found to be promising for the continuous-flow aerobic oxidation of bioethanol, giving 100% conversion and 99% acetic acid selectivity.[145] Moreover, this catalyst exhibited remarkable hydrothermal stability, with a bioethanol conversion higher than 80% and acetic acid selectivity of 95% even in the presence of 90% water. Monometallic Pd/HY zeolite catalysts were also active for the gas phase aerobic oxidation of ethanol to acetaldehyde and ethyl acetate.[146]

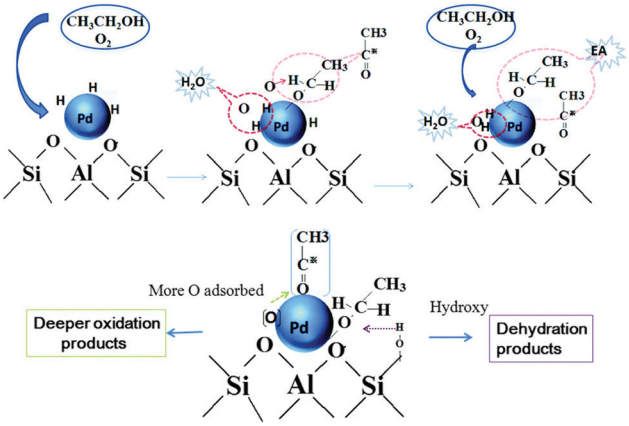

Fig. 13 Mechanism of ethyl acetate formation from ethanol through reverse hydrogen spillover process and the mechanism of dehydration and deeper oxidation over the Pd catalyst. Reproduced with permission from ref. 146. Copyright (2016) Royal Society of Chemistry.

Product selectivity can be readily tuned by controlling the oxidation state of Pd species. For example, 2 wt% Pd/HY (metallic Pd) catalyst displayed a 98.6% ethanol conversion with a 94.7% ethyl acetate selectivity, while about 89% acetaldehyde selectivity was obtained over 2 wt% PdO/HY (Pd^{2+}) catalyst. The synergy between metallic Pd NPs and the acidic zeolite *via* a reverse hydrogen spillover process was crucial for achieving improved catalytic activity and higher selectivity to ethyl acetate (Fig. 13).[146] Among the tested catalysts for the co-aromatization of biomass-derived acetic acid and methane, the 5%Zn–1%Ga/ZSM-5 catalyst provided excellent performance in terms of improved light aromatic yields, less phenol formation, lower coke production, and higher methane conversion.[147] Homogeneous dispersed metal particles, stable metal oxidation state, moderate surface acidity, and an appropriate ratio of weak/strong acidic sites are indispensable for this reaction. Physical mixing of CeO_2 with Cu/HY led to a hybrid catalyst that enabled the conversion of biomass-derived acetic acid to propylene *via* keto-hydrodeoxygenation pathway in continuous flow conditions.[148] About 85% acetic acid conversion with 49% selectivity to propylene was obtained over the CeO_2–Cu/HY (25 wt% of Cu/HY) catalyst due to the presence of highly dispersed Cu species.

2.4 Hierarchical porous zeolites

Hierarchical porous zeolites, having at least two levels of porosity, are of increasing research interest for catalytic biomass valorization because of their favorable mass transport properties compared to that of conventional microporous zeolites.[30,52] As shown in Fig. 14 (right side, hierarchical zeolite), the introduction of secondary pores into the zeolite structures can provide three key advantages: (1) enhanced active site accessibility due to controllable diffusion of molecules (orange and green spheres).[8] (2) Improved product selectivity (green spheres) driven by the presence of larger external surface. (3) A higher number of active sites (*i.e.* pore mouths) available for the reaction of bulky molecules (red spheres). Various facile strategies have been developed for the synthesis of hierarchical porous zeolites,

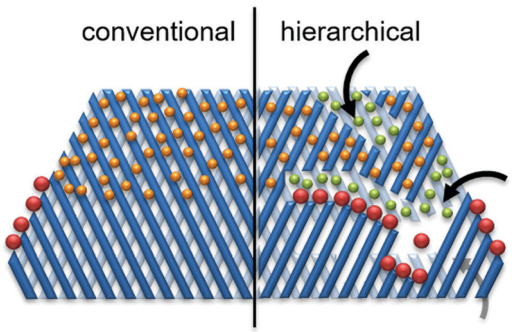

Fig. 14 Schematic representation of advantages of hierarchical zeolites towards active sites accessibility and transport/diffusion of reactants/products. Reproduced with permission from ref. 8. Copyright (2016) Royal Society of Chemistry.

including removal of framework atoms, surfactant-assisted procedure, hard-templating, zeolitization of preformed solids, and organosilane-based methods.[8,30,52]

2.4.1 Catalytic fast pyrolysis of biomass. The significance of a hierarchical porous HZSM-5 zeolite, obtained by means of desilication using an alkaline solution (NaOH), over the conventional zeolite is evidenced in the catalytic fast pyrolysis (CFP) of oak biomass.[149] The existence of open mesopores in hierarchical zeolite enables the facile diffusion of larger biomass molecules (*e.g.*, levoglucosan) to reach microporous mouths, which contain Brønsted acid sites, where the selective transformation of larger molecules to smaller fragments occurs due to the shape selectivity of micropores. The mesopores can stimulate the diffusion of formed products, thus enhancing the selectivity of mono-aromatic hydrocarbons. A similar desilication strategy was used to introduce mesopores into the ZSM-5 zeolite.[150] Owing to improved mass transport effects and a higher number of accessible Brønsted acid sites, the resulting hierarchical zeolite exhibited high aromatic yield (27.9%) from CFP of red oak compared to that obtained over the parent zeolite (23.9%). Hierarchical mordenite framework inverted (MFI) zeolites, developed by both top-down and bottom-up approaches, were also found to be active for the CFP of cellulose and *miscanthus x giganteus*.[151] Good aromatic yields were obtained over the hierarchical MFI catalysts because of their strong capacity in hindering the formation of coke and char. Optimum mesoporous volume is essential for achieving enhanced acid site accessibility. Although lower yields of bio-oil were obtained (32.6 wt%), the meso-H-ZSM-5 zeolite showed high catalytic activity in aromatization and deoxygenation during *in situ* CFP of palm kernel shell vapors.[152] The incorporation of Ga (1 wt%) into the meso-HZSM-5 zeolite led to an enhancement in the bio-oil yield from 32.6 wt% to 35.8 wt%, with improved selectivity to aromatics.

2.4.2 Upgrading of carbohydrates and their derived compounds. The catalytic efficiency of a wide variety of zeolites having distinct micropore topologies (BEA, FER, FAU, MOR, MFI, and MWW) and mesoporosities (pillared MFI, PMFI and pillared MWW, PMWW) was evaluated for the hydrolysis of inulin to produce sucrose, glucose, or fructose.[153] It was found that fructose production from inulin occurs at a much faster rate than that of sucrose followed by glucose. The role of pore mouth catalysis of zeolites for inulin hydrolysis was also examined in this work. Li *et al.*[154] reported the microwave-assisted conversion of carbohydrates to methyl levulinate in methanol over metal–zeolite hybrid catalysts. Especially, the Zr-zeolite hybrid ZrY6(0.5) catalyst gave 67–73%, 78%, 53%, and 27% yields of methyl levulinate from monosaccharides (*e.g.*, glucose, mannose, and galactose), sucrose, starch, and cellulose, respectively. Ample amounts of acid–base sites, high stability, and unique mesoporous structure (average pore size is 6.2 nm) are the key reasons for high performance of ZrY6(0.5) catalyst. It was shown that the hierarchically porous structure of Sn-β zeolite (Sn-β-H) facilitates the selective conversion of sugars to high yields of alkyl lactate, while inhibiting the undesirable side reactions, thus outperforming conventional Sn-zeolite catalysts.[155] In addition, Sn-β-H zeolite can be efficiently reused for at least five times with constant catalytic activities and product selectivity. A multiple-step post-synthesis strategy composed of controllable dealumination, desilication, and metal incorporation was employed for the synthesis of a hierarchical *meso*-Zr–Al-β zeolite, which contains well-balanced Brønsted/Lewis acid sites and abundant mesopores.[156] As a result, the *meso*-Zr–Al-β zeolite displayed good catalytic activity and excellent recyclability in the conversion of furfural to γ-valerolactone. The sequential dealumination and alkaline treatment is another attractive strategy to obtain hierarchical NaY zeolite with optimized Lewis acidity and basicity.[157] The resulting zeolite afforded high product selectivity (75%) and tremendous recyclability for lactic acid-to-acrylic acid transformation. The combination of BEA topology, mesoporosity, and framework metal sites (Zr and Al) was demonstrated to be promising for the liquid phase catalytic conversion of furfural to useful bio-products, such as furanic ethers, levulinate esters, and angelica lactones.[158] In this work, post-synthesis acid/alkaline/impregnation treatments were performed to introduce defect sites, mesopores, and framework Zr sites into the zeolite structures, respectively.

2.4.3 Upgrading of lignin-derived compounds. A hierarchical porous ZSM-5 zeolite coupled with Pd/C acted as a bi-functional catalyst for the aqueous phase hydrodeoxygenation (HDO) of eugenol.[159] Mesopores were introduced into the ZSM-5 zeolite *via* an alkaline treatment, and hence, higher eugenol conversion and superior selectivity to hydrocarbons were obtained compared with the parent ZSM-5 zeolite. In addition, the alkaline treatment led to the formation of a greater amount of weak acid sites in ZSM-5 zeolite, which promoted the hydrolysis and dehydration reactions. The synergistic effect of hierarchical porous structure and exposed acid sites present in a mesoporous ZSM-5 zeolite-supported Ru catalyst was also noted for the liquid phase HDO of both small and bulky phenolic molecules.[160] The modified ZSM-5 zeolite contains both microporosity and b-axis-aligned mesoporous structure.

2.4.4 Conversion of edible biomass-derived compounds. Nanostructured hierarchical ZSM-5 zeolites (Fig. 15) were found to be extremely stable in continuous-flow dehydration of glycerol

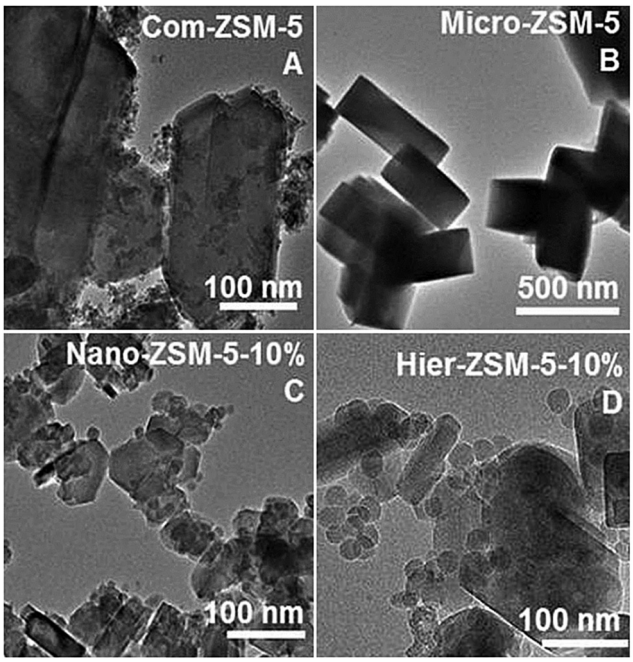

Fig. 15 TEM images for (A) Com-ZSM-5, (B) Micro-ZSM-5, (C) Nano-ZSM-5-10%, and (D) Hier-ZSM-5–10%. Reproduced with permission from ref. 102. Copyright (2017) John Wiley and Sons.

to acrolein, exhibiting a high level of glycerol conversion and acrolein selectivity up to 10–24 h, while conventional ZSM-5 zeolite rapidly deactivated already after 2–3 h on stream.[102] This remarkable catalytic stability was attributed to hierarchical structure of micro-, meso-, and macro-pores, which enhance the resistance of ZSM-5 against coke formation. A spongy structured titanosilicate zeolite having mesopores with a diameter of 3–5.5 nm was developed by combining pore extending and post-treatments.[161] The investigated liquid phase epoxidation of methyl oleate with *tert*-butyl hydroperoxide demonstrated the excellent catalytic efficacy of spongy structured zeolite with >99% conversion and >90% selectivity to the epoxy product, outperforming the corresponding conventional zeolite (39% conversion). Zr-modified hierarchical mordenite catalysts, prepared by HF and NH_4F etching, followed by incipient wetness impregnation, are useful catalysts for the glycerol esterification with acetic acid to produce biodiesel additives.[162] The addition of Zr led to improved turnover activity compared to pure zeolite, due to the presence of well-balanced Brønsted-Lewis acid sites.

3. Mesoporous SiO_2 based catalysts for biomass valorization

Over the last two decades, mesoporous materials have been tremendously used in heterogeneous catalysis because of their exceptional porosity and surface area properties.[33,163,164] Mesoporous materials have also found plentiful applications in adsorption, sensing, drug delivery, nanodevices, and lithium-ion batteries. According to IUPAC, mesoporous materials (the Greek prefix 'meso' means 'in between') are defined as those

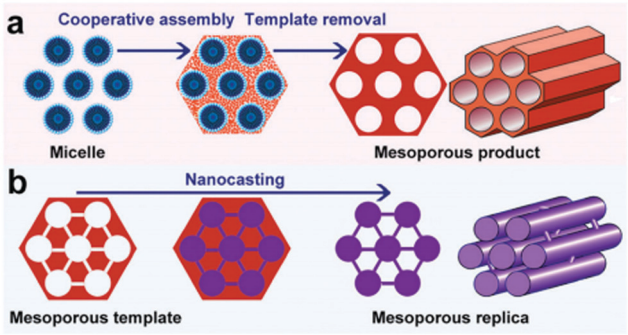

Fig. 16 (a) soft-templating and (b) hard-templating synthesis routes for the design of ordered mesoporous materials. Reproduced with permission from ref. 166. Copyright (2011) Royal Society of Chemistry.

having pore diameters (*i.e.* 2–50 nm) in between micropores (<2 nm) and macropores (>50 nm).[165] Two types of synthesis methods, namely soft-templating and hard-templating, are often used for the production of mesoporous materials with monodispersed pores in a long-range ordered structure (Fig. 16).[166] The strategic motivation to develop mesoporous materials was to overcome the mass transport limitations associated with the zeolites whose pore dimensions are usually below 2 nm. Porous materials with similar textural and acid characteristics to zeolites, but with larger pores could mitigate the barrier for the diffusion of bulky molecules, leading to improved reaction rates.[165]

The pioneering work of Mobil's scientists in the 1990s led to the discovery of mesoporous silica materials, popularly known as the M41S family.[32,33,164,167] This breakthrough finding has inspired the scientific community towards developing a variety of novel mesoporous materials, including non-silica metal oxides (Al_2O_3, ZrO_2, Co_3O_4, NiO, Fe_2O_3, and Mn_3O_4), mesoporous carbons, mesoporous organic polymers, and mesoporous inorganic non-oxide materials (metal nitrides, metal chalcogenides, carbides, and fluorides). The use of supramolecular aggregates as structure-directing agents in a sol–gel synthesis medium plays a crucial role in the formation of ordered mesoporous silica structures, with controlled pore size distribution in hexagonal, cubic or lamellar structures (Fig. 17).[32] By modifying synthesis methodologies and self-assembly mechanisms, a wide variety of mesoporous silica materials have been developed, including SBA (Santa Barbara Amorphous, University of California, Santa Barbara),[168] KIT (Korean Institute of Technology, currently known as Korea Advanced Institute of Science and Technology),[169] MSU (Michigan State University, USA)[170] and COK (Centre for Surface Chemistry and Catalysis, KU Leuven, Belgium)[171] families.

3.1 Catalytic role of mesoporous SiO_2 properties in biomass valorization

Mesoporous silica materials exhibit a broad spectrum of fascinating features, such as unique textural properties, negligible mass transport limitations, and diversified functionalization.[29] Notably, they show tailorable pore diameters (2–50 nm), large pore volumes, and high specific surface areas (400–1400 $m^2\ g^{-1}$). Owing to these exceptional characteristics, mesoporous silica

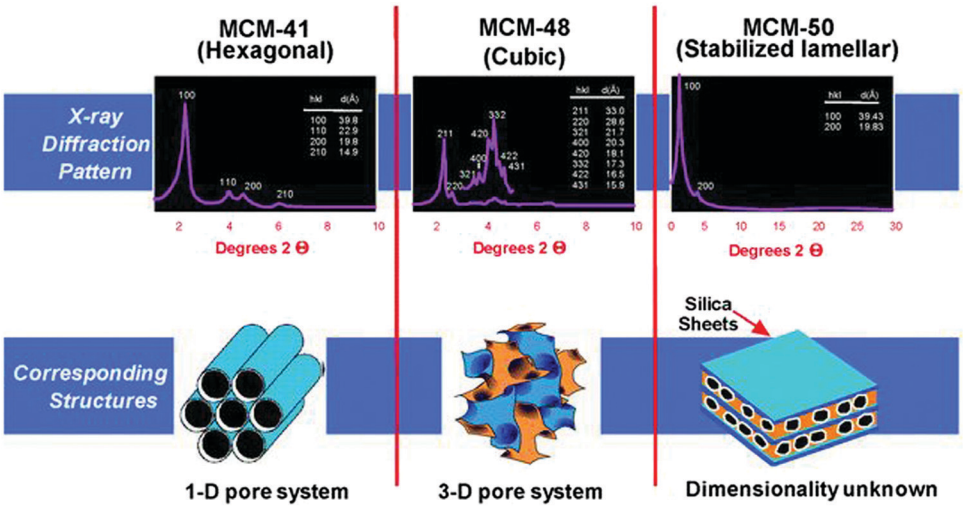

Fig. 17 Powder XRD patterns and structures of mesoporous SiO_2 materials (MCM-41, MCM-48, and MCM-50). MCM – Mobil Composition of Matter or Mobil Crystalline Material. Reproduced with permission from ref. 32. Copyright (2013) Royal Society of Chemistry.

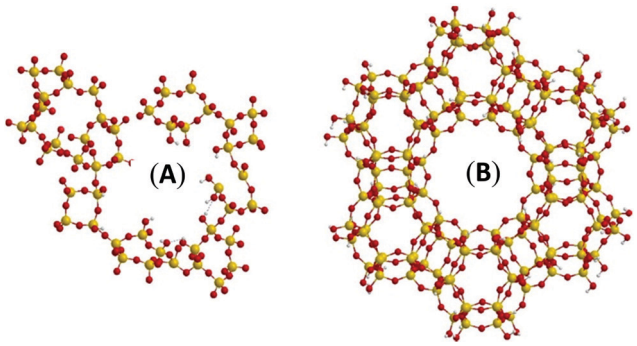

Fig. 18 (a) Disordered and (b) ordered mesoporous structures. Reproduced with permission from ref. 172. Copyright (2013) American Chemical Society.

can efficiently interact with atoms, molecules, or ions, not only at the external surface, but also through the internal pores.[33,164] The high specific surface area of mesoporous silica enables homogeneous dispersion of catalytically active metal species (Ru, Ni, Cu, Co, Mn, Pt, Pd, Fe, *etc.*), which could be readily accessible throughout the catalyst matrix. The ordered mesoporous silica materials with relatively large pores are particularly important for catalytic biomass upgrading as they can allow the bulky biomass molecules to access the active sites inside the pores (Fig. 18).[172] The significance of hierarchical SiO_2 materials, having interconnected mesopore–macropore networks and sometimes micropores, is also recognized in biomass valorization. The key advantage of hierarchical porous materials in catalysis is that micro/mesopores can offer active sites for reactants, whereas macropores can provide feasible routes for reactants/intermediates accessing the active sites, as well as for the facile desorption of products, resulting in high turnover frequency rates.[36] These multimodal porous structures can tremendously facilitate mass-transport in viscous liquid phase biomass conversions, such as biodiesel synthesis.[173] Morphology of mesoporous silica materials is also a pivotal parameter, together with pore structure and surface area, for fine-tuning their activities and selectivities in biomass upgrading. Precise shape control of catalyst particles allows preferential exposure of active species on the catalyst surface, which is a vital criterion for heterogeneous catalysis. In addition, the surface-exposed active species can provide an advantageous basis for the systematic investigation of structure–activity relationships, which could provide new insights for the design of high-performing shape-controlled mesoporous catalysts for efficient biomass conversion.

In order to improve the catalytic activity of mesoporous silica, incorporation of metals into the silica framework has been frequently attempted.[174–177] Aluminium was the first metal incorporated into the framework of mesoporous silica (*e.g.*, MCM-41) to develop a potential alternative to zeolites for petrochemical industry.[177] Since then, various metals including Zr, Co, and Sn have been incorporated in order to obtain high-performing mesoporous silica catalysts. For example, by carefully varying the composition of Al/Si ratio, new mesoporous silica–alumina catalysts were developed with high BET surface area and abundant acid properties. The resultant composites showed excellent catalytic activities in the production of HMF from carbohydrates.[178] Incorporation of acid or base functional species in the framework of mesoporous silica is also a promising strategy to multiply its applications in catalysis. The large pore volume of mesoporous silica provides ample room to accommodate these functional species.[179] For instance, acid functionalized ($-SO_3H$, $-SO_3H/C_2H_5$, –COOH, and –CN) SBA-15 catalysts were found to show high performance for the esterification of fatty acids as well as for the transesterification of triglycerides to produce biodiesel fuel. Therefore, by controlling the surface and the internal porous structures, a variety of advanced mesoporous silica materials have been developed and their catalytic applications in biomass conversions are reviewed in the following paragraphs.

3.2 Pristine and doped mesoporous SiO_2 catalysts

Mesoporous silica-based materials can exhibit Lewis acidity originating from Si as well as from incorporated metals.

Hence, the Lewis acidity and ordered mesoporous structures are the key factors for the catalytic efficiency of mesoporous silicas, mainly for acid-catalyzed biomass conversions.

3.2.1 Valorization of cellulose and its derived compounds. Catalysts' acid properties play a crucial role in the hydrolysis of cellulose to glucose, one of the vital transformations in bio-refinery process. A mesoporous MCM-48 silica, prepared by a sol–gel method, was found to be effective in cellulose hydrolysis.[180] Owing to adequate surface acidity of MCM-48 silica, about 14% glucose yield was achieved, which is higher than that obtained with activated carbon (6.4% glucose yield) and commercial SiO_2 (7% glucose yield). Biomass-derived lactates are novel green solvents with a potential to replace hazardous organic solvents in the chemical, cosmetic, and pharmaceutical industries.[181,182] For the synthesis of ethyl lactates from cellulose, the Hongfei Lin group developed a Zr incorporated SBA-15 catalyst having relatively strong Lewis and weak Brønsted acid sites, as well as a superior surface hydrophobicity.[181] Particularly, the water-tolerant Lewis acidity of Zr-SBA-15 catalyst is essential to attain good yields of ethyl lactate (33%). They also used similar types of Zr-SBA-15 catalysts for the production of methyl lactate from various carbohydrates, such as pentoses, hexoses, disaccharides, cellulose, and starch.[182] The effect of reaction temperature, reaction time, and the catalyst loading was examined towards methyl lactate production. The Si/Zr ratio of Zr-SBA-15 catalysts strongly affects the Lewis acidity and hence the catalyst performance as well as product selectivity. On the other hand, the pore size of Zr-SBA-15 catalysts markedly determines the formation of solid organic residues on the catalyst surface. The Sn-incorporated MCM-41 catalyst is active for the conversion of glucose to methyl lactate (40.3% yield) in subcritical methanol conditions.[183] The mesoporous structure and acid sites of reused catalyst remained unaffected with a negligible amount of Sn leaching (0.15%). The significance of Lewis acidity of Sn-SBA-15 catalysts was also noticed for the conversion of carbohydrates to methyl lactate.[184] About 57% yield of methyl lactate was obtained from inulin over Sn-SBA-15 catalyst (Si/Sn molar = 150), which contained 45.9 μmol/g Lewis acid density. A mesoporous SiO_2-Al_2O_3 catalyst with Si/Al ratio of 18 provided improved HMF yields (63%) from glucose (entry 5, Table 1).[178] This mesoporous catalyst was also able to convert bulky biomass molecules (*e.g.*, disaccharides, polysaccharides, and lignocellulose) to HMF. High BET surface area, ample amounts of acid sites and optimized Brønsted/Lewis acid ratio are the key factors for achieving improved HMF yields from glucose and other carbohydrates. Compared to protonated zeolites (H-ZSM-5, H-Y and H-beta), high HMF yields (63%) from glucose were obtained over an Al doped mesoporous MCM-41 silica catalyst (Si/Al molar ratio of 10).[185] This study reveals the positive effect of mesoporous structure in glucose-to-HMF transformation (entry 6, Table 1).

3.2.2 Catalytic fast pyrolysis of biomass. The catalytic fast pyrolysis (CFP) of lignin was studied using Al-MCM-41, Al-SBA-15, and Al-MSU-J catalysts.[186] A high fraction of aromatics and relatively low amount of char/coke were obtained. Both the milder Brønsted and the stronger Lewis acid sites play an indispensable role in the conversion of pyrolysis intermediates towards fewer oxygenated phenols and aromatic hydrocarbons. Especially, the Al-MCM-41 (Si/Al ratio = 50) catalyst was found to be promising in CFP of lignin, which was attributed to large pore volume and small particle size. The significance of SiO_2/Al_2O_3 mole ratio on the performance of Al-doped SBA-15 catalysts was also markedly observed for corncob pyrolysis.[187] Al-SBA-15 catalyst with Si/Al ratio of 20 was selective towards 2-methoxy phenyl acetate (59.4%), an important chemical for food industry. Owing to weak acidity and medium porosity, the SiO_2-Q10 catalyst (pore diameter of 16 nm) gave better activity for CFP of Jatropha residue compared with SiO_2-Q3, -Q30, and -Q50 having pore diameters of 3, 45, and 68 nm, respectively.[188] In addition, the SiO_2-Q10 catalyst can efficiently remove various oxygenated compounds, such as acids, ketones, and aldehydes as well as inhibit the formation of coke and polycyclic aromatics.

3.2.3 Other biomass upgrading reactions. *p*-Xylene is a versatile chemical widely used in polymer industry, which can be produced from 2,5-dimethylfuran using mesoporous SiO_2–Al_2O_3 catalysts.[189] The conversion and product yields were strongly dependent on the Si/Al ratio. The catalyst, with a higher Al content, provided high production rates of *p*-xylene due to the presence of abundant Brønsted acid sites. Mesoporous Nb_2O_5–SiO_2 catalysts with varying Nb amount were found to be active for the epoxidation of soybean oil with H_2O_2.[190] Interestingly, the epoxidation activity of Nb_2O_5–SiO_2 catalysts decreases with the increase of Nb content, but the selectivity to epoxide increases due to the presence of strong Brønsted acid sites in higher Nb content catalysts. Andas *et al.*[176] found a noticeable effect of Co loading (5–15 wt%) on the structure–activity performance of mesoporous Co–SiO_2 catalysts for the liquid phase oxidation of lignin-derived compound (phenol). Results indicated the successful insertion of Co ions into the silica framework, without affecting its mesoporous structure. Well-defined pore channels and spherical shaped nanoparticles with an average particle size of 9.44 nm were found for Co–SiO_2 catalysts, especially for 10 and 15 wt% Co loadings. The resulting catalysts displayed good activity in the oxidation of phenol and the catalysts were stable up to five recycles without much loss in catalytic activity. Nowadays, ethanol is a readily available sustainable chemical from biomass feedstocks for the production of a large spectrum of important drop-in chemicals, including ethylene, propylene, 1,3-butadiene, isobutene, acetone, acetaldehyde, acetic acid, butanol, *etc.* Teruki *et al.*[191] found that ethanol can be quantitatively converted into ethylene over MCM-41 silica at temperatures above 350 °C and gas hourly space velocity (GHSV) of 400 h^{-1}. The presence of Al in MCM-41 had no impact on its catalytic performance, while increasing pore size from 2.1 nm to 3.3 nm led to a drastic decrease in ethanol conversion from 75% to 50%, respectively, at 400 °C and GHSV of 20 000 h^{-1}. Furthermore, MCM-41 catalyst was active for more than 50 h time-on-stream study, with a remarkable resistance to water, allowing the use of crude ethanol without further purification.

3.3 Shape-controlled and hierarchical porous SiO_2-based catalysts

Mesoporous silica-based materials with well-defined shapes have attracted paramount attention for catalytic biomass upgrading,

as reaction rates and product selectivity can be controlled by shape-dependent properties.[178,192] As well, hierarchical porous silica materials have been featured in forefront research towards catalytic biomass conversions because of their synergistic meso–macro porous structures.[36,179] Several studies also reported the cooperative effect of shape-control and pore hierarchy in enhancing the catalytic performance of porous silica materials. In this section, we focus on the catalytic applications of shape-controlled and hierarchical porous SiO_2-based materials for various biomass conversions.

3.3.1 Upgrading of cellulose and its derived compounds. An efficient catalytic route was developed for the direct conversion of cellulose to HMF using a hierarchical macro-/mesoporous silica based catalyst anchored with both acid ($-SO_3H$) and base ($-NH_2$) species (entry 7, Table 1).[193] The particle size of porous silica material was found to increase after functionalization. However, reasonable good yields of HMF (44.5%) were obtained over the functionalized mesoporous silica catalyst, attributed to its hierarchical porous structure and ample amounts of acid–base sites. Both the chelating agent used during the catalyst synthesis and the metal composition exhibited a substantial effect on the performance of bimetallic Ni–W catalysts dispersed on mesoporous SiO_2–OH nanospheres for the transformation of cellulose to ethylene glycol.[194] Higher conversion rates and improved product yields (63.3%) were achieved in the case of 15%Ni–20%W/SiO_2 catalyst prepared by using ethanediamine (chelating agent) and ethylene glycol (reducing agent), due to the existence of uniformly dispersed metal particles. Owing to the presence of smaller sized Ru NPs (average particle size of <1.5 nm) and the acidity of Zr sites, Ru catalyst supported on mesoporous Zr–SiO_2 spheres showed good hydrogenation activity for levulinic acid-to-γ-valerolactone transformation, outperforming a conventional silica based catalyst.[195] The Li group developed a facile strategy for the encapsulation of Ru–B amorphous alloys in yolk–shell shaped mesoporous silica structure (Fig. 19).[192] The resulting shape-controlled catalyst, in combination with an enzyme, was able to catalyze the one-pot synthesis of sorbitol from dextrin (obtained *via* hydrolysis of starch). By controlling the pore size, the outer SiO_2 shell allowed facile diffusion of glucose molecules obtained from dextrin to directly access the Ru–B cores and the produced sorbitol can readily exit through these pores. The porous outer silica shell also inhibits the accessibility of Ru–B sites for larger amyloglucosidase and colloidal hydrolysis substances, preventing catalyst deactivation, and hence, improved yields of sorbitol and excellent catalyst durability were obtained. Similar methodology was also used for the design of yolk–shell nanoarchitectures with a Ru-containing core supported on carbon and a radially oriented mesoporous silica shell, which was shown to be efficient for dextrin-to-sorbitol transformation.[198]

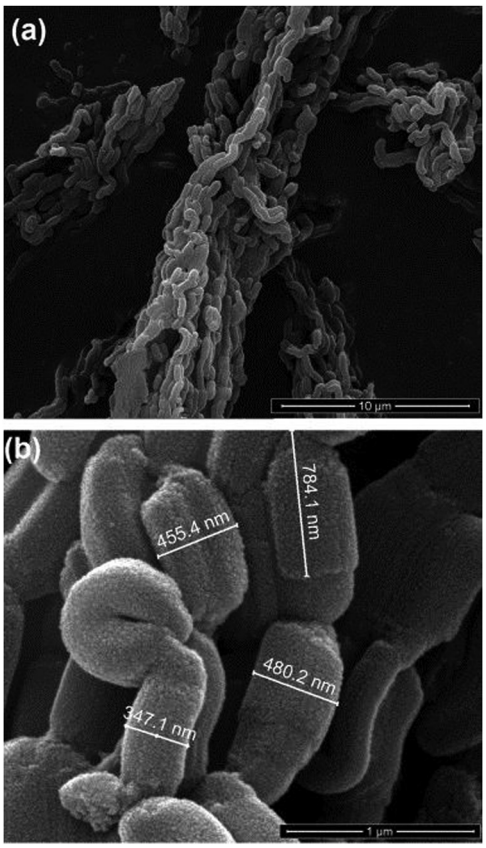

Fig. 20 SEM images of SBA-15-SO_3H catalyst. Reproduced with permission from ref. 196. Copyright (2014) John Wiley and Sons.

A propylsulfonic acid-functionalized SBA-15, containing fiber-like domains with an average particle size of 430 nm aggregated into macrostructures (Fig. 20), was investigated for the condensation of furfuryl alcohol with 1-butanol to give butyl levulinate.[196] The successful incorporation of sulfonic acid groups into the SBA-15 structure was confirmed by FT-IR analysis. This catalyst showed about 96% yield (and 100% selectivity) of butyl levulinate and no leaching of the active species was noticed. A strong relationship of surface-decorated active species with the catalytic activity of Co–Mn oxide/nanospherical porous silica was found in liquid phase, base-free oxidation of HMF to 2,5-furandicarboxylic acid.[197] The optimized

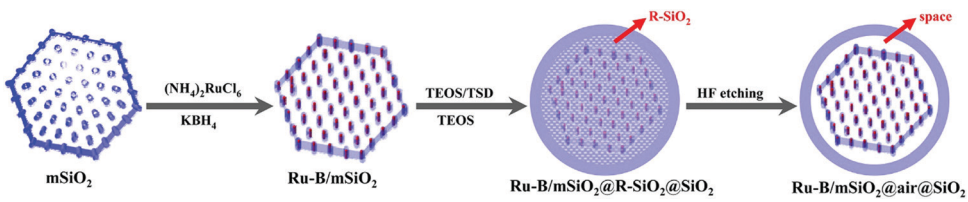

Fig. 19 Illustration of the synthesis process of yolk–shell structured Ru–B/$mSiO_2$@air@SiO_2 catalyst. Reproduced with permission from ref. 192. Copyright (2014) American Chemical Society.

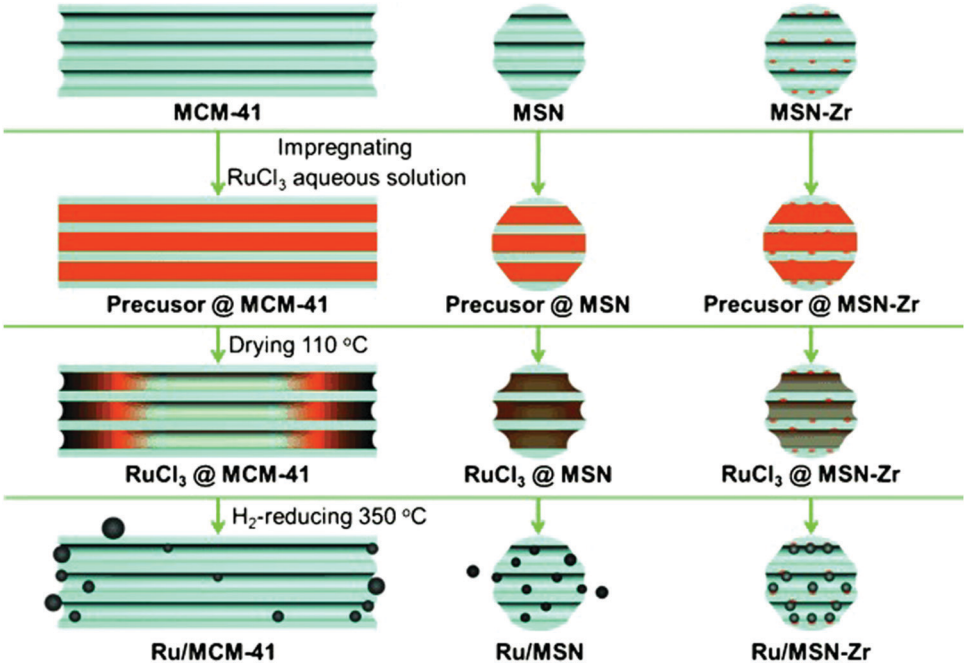

Fig. 21 Mechanism for the channel-length effect of mesoporous silica on the synthesis of supported Ru catalysts. Reproduced with permission from ref. 199. Copyright (2013) John Wiley and Sons.

catalyst (Mn : Co = 1 : 2) displayed ~100% HMF conversion with a 72.4% yield of 2,5-furandicarboxylic acid as well as a durable catalytic activity for several recycles (entry 2, Table 5). Uniformly dispersed and thermally stable Ru nanoclusters were found within mesoporous zirconium silica nanospheres, which are the primary factors for achieving improved catalytic results in the aqueous-phase hydrogenation of furan derivatives.[199] The reaction temperature also played a determinant role in controlling product selectivity over the Ru cluster catalyst. A plausible mechanism was proposed for the channel-length effect of mesoporous silica on the size of Ru clusters (Fig. 21).

3.3.2 Valorization of edible biomass and its derived compounds. Various flower shaped catalysts composed of tungsten (with varied loadings up to 25%) dispersed on mesoporous Ti/SiO_2 were studied for the transesterification of waste cottonseed oil to produce biodiesel.[200] The impregnation of tungsten led to decreased BET surface area and low pore volume of Ti/SiO_2 due to pore blockage by isopolyanions. However, about 98% yield of biodiesel was obtained over the 20%-$W/TiO_2/SiO_2$ catalyst. Dhainaut *et al.*[173] developed hierarchical porous silica catalysts, containing well-defined, interconnecting macro-/mesoporous networks with narrow size distribution. Owing to enhanced mass transport properties, the developed silica catalysts showed good catalytic efficiencies in the esterification of long chain palmitic acid as well as in the transesterification of bulky glyceryl trioctanoate to biodiesel. Spherically shaped SnSi-*x* catalysts (x = 37 and 74, Si/Sn atom ratio) with calibrated mesopores of 5–6 nm were found to be effective for the synthesis of ethyl lactate from dihydroxyacetone and ethanol.[201] Dihydroxyacetone is produced by partial oxidation of glycerol. A remarkable turnover number (TON = 173) was obtained for ethyl lactate production over SnSi-74 catalyst, outperforming various MCM-41 based catalysts. The catalyst is recyclable and no leaching of active phases was found after several recycles.

3.4 Mesoporous SiO_2 supported catalysts

The dispersion of metal NPs into the framework of porous materials is a widely used strategy for the development of highly stable, efficient supported metal catalysts. As a result, aggregation and leaching of active phase particles can be prevented, while maintaining active site accessibility to reactants/intermediates.[177] Mesoporous silica is regarded as an ideal supporting carrier for stabilizing metal particles because of its unique characteristics, such as large surface area and suitable pore dimensions.[177,197]

3.4.1 Upgrading of carbohydrates and their derived compounds. The hydrogenolysis of cellulose to polyols (*e.g.*, ethylene glycol) has attracted much attention because of multiple applications of the resulting products in plastic, food, and pharmaceutical industries. A variety of Ni–WO_3/SBA-15 catalysts with varied metal compositions and catalyst synthesis conditions was developed for the hydrogenolysis of cellulose to polyols.[202–204] Cao *et al.*[202] demonstrated that the presence of strong NiO–WO_3 interactions in Ni–WO_3/SBA-15 catalyst not only promotes the reduction of WO_3, but also controls the NiO reduction. As a result, a 70.7% yield of ethylene glycol at complete conversion of cellulose in aqueous phase was obtained over 3%Ni–15%WO_3/SBA-15 catalyst. In another study, the effect of pH of the solution, employed during the catalyst synthesis, was studied on the performance of Ni–W/SBA-15 catalysts for the aqueous phase hydrogenolysis of cellulose to polyols.[203] Interestingly, all the catalysts showed high thermal stability and

superior BET surface area values in the range of 330–450 $m^2 g^{-1}$. The reduction of NiO and the phase states of nickel and tungsten were highly dependent on the pH of the solution. Among the catalysts employed, 10%Ni–20%W/SBA-15 catalyst, prepared at pH = 1, displayed a 74.5% yield of total low carbon polyols including ethylene glycol, 1,2-propylene glycol, and glycerol. Xiao *et al.*[204] developed Ni–W/SBA-15 catalysts by means of biomass-based sucrose as the reducing agent without using any conventional reduction step. Notably, the 10%Ni-15%W/SBA-15 catalyst calcined at 400 °C exhibited about 68% conversion of cellulose with a 61% selectivity to ethylene glycol. An appropriate reaction pathway for cellulose hydrogenolysis to polyols was proposed in this study.

Hydrogen is one of the highly appealing energy sources for our modern world. However, it is mainly produced from traditional carbon-sources *via* steam reforming of natural gas or coal gasification. As an alternative process, the direct conversion of cellulose to hydrogen rich gas was performed using Ni catalysts supported on different mesoporous silica materials, such as SBA-15, SBA-16, KIT-6, and MCM-41.[205] Among them, Ni/SBA-15 and Ni/KIT-6 catalysts afforded the highest hydrogen yield, outperforming the Ni catalyst supported on commercial silica. The presence of high BET surface area, pore volume, and larger pore diameter facilitates the easy diffusion of complex reactant/intermediate molecules towards the active sites, hence increasing hydrogen formation. For selective hydrogenation of glucose to sorbitol, comparable activity results were achieved over Ru/MCM-48 catalyst with respect to Ru/TiO_2 and Ru/C catalysts.[180] In recent work, bimetallic Ru–Ni particles (total metal loading is 3 wt%) supported on MCM-48 were demonstrated to be efficient catalysts for the hydrogenation of glucose to sorbitol.[206] Importantly, catalysts with Ru : Ni ratios higher than 0.45 displayed the best performance compared to monometallic Ni/MCM-48 catalyst. The Ru–Ni/MCM-48 catalyst was reused for three cycles without much loss in catalytic activity.

García-Sancho *et al.*[207] demonstrated a considerable effect of Nb_2O_5 on the catalytic performance of Nb_2O_5/MCM-41 for the dehydration of xylose to furfural. About 74.5% conversion with a 36.5% furfural yield was achieved over a 16 wt% loaded Nb_2O_5 catalyst. Moreover, the optimized catalyst was reused for three runs with no significant loss of catalytic activity. Catalytic hydrogenation of furfural can provide several valuable chemicals and solvents, including furan, furfuryl alcohol, and tetrahydrofuran. The most significant results obtained for furfural hydrogenation catalyzed by porous and nanoscale materials are presented in Table 3. For instance, bimetallic Co–Cu particles supported on SBA-15 with a fixed Cu loading (10 wt%) and various Co loadings (2.5, 5, and 10 wt%) were developed for the liquid phase hydrogenation of furfural to furfuryl alcohol.[208] The effect of several reaction parameters, such as catalyst dosage, pressure, temperature, and furfural concentration was evaluated for this reaction. Compared to the catalysts supported on conventional silica, the Co–Cu/SBA-15 catalyst (Cu 10 wt% and Co 10 wt%) was found to show a high catalytic performance with 99% furfural conversion and 80% furfuryl alcohol selectivity, which was attributed to high dispersion of active Cu sites (entry 2, Table 3). The beneficial effect of both metal–metal and metal–support interactions was noticed for the liquid phase hydrogenation of furfural to tetrahydrofurfuryl alcohol.[209] The reaction was carried out over Ni–Co catalysts supported on short channeled SBA-15, MCM-41, MCM-4, MCF-2 and conventional SBA-15. Interestingly, Ni–Co catalyst (Ni/Co molar ratio = 0.67) supported on short channeled SBA-15 showed a higher yield of tetrahydrofurfuryl alcohol (92%) at full conversion of furfural, due to the unique structure of the short channels as well as the appropriate and uniform pore size distribution (entry 3, Table 3). The formation of $NiCo_2O_4$ species favored the homogenous distribution of active sites (Ni and CoO) in bimetallic catalysts, which also contributed greatly to obtain improved product yields in the hydrogenation of furfural. A series of Cu/mesoporous SiO_2 catalysts (Cu loadings from 2.5 to 20 wt%) were evaluated for the gas phase hydrogenation of furfural.[210] The catalyst with 10 wt% Cu loading provided an appropriate balance between the tendency to form carbonaceous deposits and the resistance to particle sintering, giving good yields of 2-methylfuran (95%) after 5 h (entry 4, Table 3).

The combination of mesocellular silica foam (MCF) with Nafion-resin nanoparticles was found to show good catalytic performance in the liquid phase dehydration of fructose to HMF (entry 8, Table 1).[211] The effects of Nafion loading, reaction temperature, time, and solvent were investigated for this reaction. A 89.3% yield of HMF was obtained over a Nafion(15)/MCF catalyst, which was attributed to strong acid strength and open large pore system. A possible reaction mechanism was proposed for fructose dehydration to HMF over Nafion-modified MCF catalysts as shown in Fig. 22. A three-phase catalytic system, including a solid acid catalyst (nanostructured vanadium phosphate and mesostructured cellular silica foam) was developed for the conversion of fructose to HMF.[212] Pyridine-adsorption FT-IR studies revealed the presence of both Brønsted and Lewis acidic sites in the developed catalyst. A high selectivity to HMF (91%) at 89% fructose conversion was obtained over this catalytic system because of its ability to inhibit undesired side reactions of HMF in the presence of H_2O. A direct correlation of the γ-valerolactone production rate with the dispersion state of Zr species was observed for the catalytic transfer hydrogenation of levulinic acid and its esters over ZrO_2/SBA-15 catalysts.[213] A plausible reaction mechanism was proposed, in which basic Zr–OH sites promote the catalytic transfer hydrogenation reaction involving a six-membered ring transition state.

3.4.2 Valorization of edible biomass and its derived compounds. Several 12-tungstophosphoric acids (HPW) deposited on a mesoporous titania–silica composite (TSC) were examined for the esterification of oleic acid with methanol to produce biodiesel.[214] Especially, the 20%HPW/TSC catalyst was found to be highly active and a maximum 95% conversion of oleic acid was achieved due to the uniform dispersion of HPW species on TSC support. The steam reforming of glycerol is one of the widely studied reactions to produce sustainable hydrogen. Carrero *et al.*[215] found that incorporation of Zr, Ce and La into the SBA-15 framework can enhance the structure–activity performance of Co/SBA-15 catalyst for the production of hydrogen

Table 3 Hydrogenation of furfural over porous and nanoscale catalysts

Entry	Catalyst	Reaction conditions	Product	Catalytic activity		Key factors for the catalyst performance	Ref.
				Conv. (%)	Yield (%)		
1	Pd NPs@silicalite-1 zeolite	Gas phase, 0.1 g catalyst, 5 wt% furfural (mass ratio of furfural/*n*-butyl alcohol at 1/19), feed rate at 0.5 mL h^{-1}, 10% H_2/Ar at 10 mL min^{-1}, 250 °C, atmospheric pressure	Furan	100	99.9	Controlled diffusion of molecules within the hydrophilic zeolite micropores	137
2	Co–Cu/SBA-15[a]	Liquid phase, 1 g catalyst, 170 °C, 20 bar H_2, furfural-to-isopropanol molar ratio of 1 : 7, 4 h	FOL[b]	99	80	High dispersion of active Cu sites	208
3	Ni–Co/SBA-15[c]	Liquid phase, 0.8 g catalyst, 5.82 g furfural, ethanol, 90 °C, 50 bar initial H_2, 2 h	THFA[d]	100	92	Short pore channels, appropriate and uniform pore size distribution of SBA-15, uniform and high dispersion of Ni^0 and CoO	209
4	10 wt% Cu/ mesoporous SiO_2	Gas phase, 5 h, 210 °C, H_2/furfural molar ratio of 11.5, weight hourly space velocity of 1.5 h^{-1}	MF[e]	—	95	Higher amounts of accessible active Cu sites as well as appropriate balance between the tendency to form carbonaceous deposits and resistance to particle sintering	210
5	Pd–Pt/TiO_2	Liquid phase, 0.3 M furfural, substrate/metal molar ratio = 500, 3 bar H_2, 30 °C, 240 min	THFA	100	95	Synergistic Pd–Pt interaction	336
6	CuNi/MgAlO (Cu/Ni = 1 : 1)	Liquid phase, 5 mmol furfural, methanol, 0.01 g catalyst, 100 °C, 4 h, 4 MPa H_2	FOL	100	99	High metal dispersion, homogeneous composition of CuNi alloys, and catalyst basicity	337
7	CuZnAl mixed oxide (Cu/Zn = 0.5)	Liquid phase, 0.2 g catalyst, 5 mmol furfural, 150 °C, 4 MPa H_2, 6 h, H_2O	Cyclopentanone	97.9	62	Smaller sized Cu particle with homogeneous dispersion and high specific surface area	339
8	CuFe[f]/γ-Al_2O_3	Gas phase, 1 mL catalyst, 175 °C, LHSV[g] 1 h^{-1} with respect to furfural and GHSV[h] 1200 h^{-1} with respect to H_2, 1 atm. pressure	FOL	93	91	Synergistic bimetallic particles and abundant oxygen vacancies in iron oxide	340

[a] (Cu – 10 wt% and Co – 10 wt%). [b] FOL – furfuryl alcohol. [c] (Ni/Co molar ratio = 0.67). [d] THFA – tetrahydrofurfuryl alcohol. [e] MF – 2-methylfuran. [f] (Cu – 10 wt% and Fe – 10 wt%). [g] LHSV – liquid hourly space velocity. [h] GHSV – gas hourly space velocity.

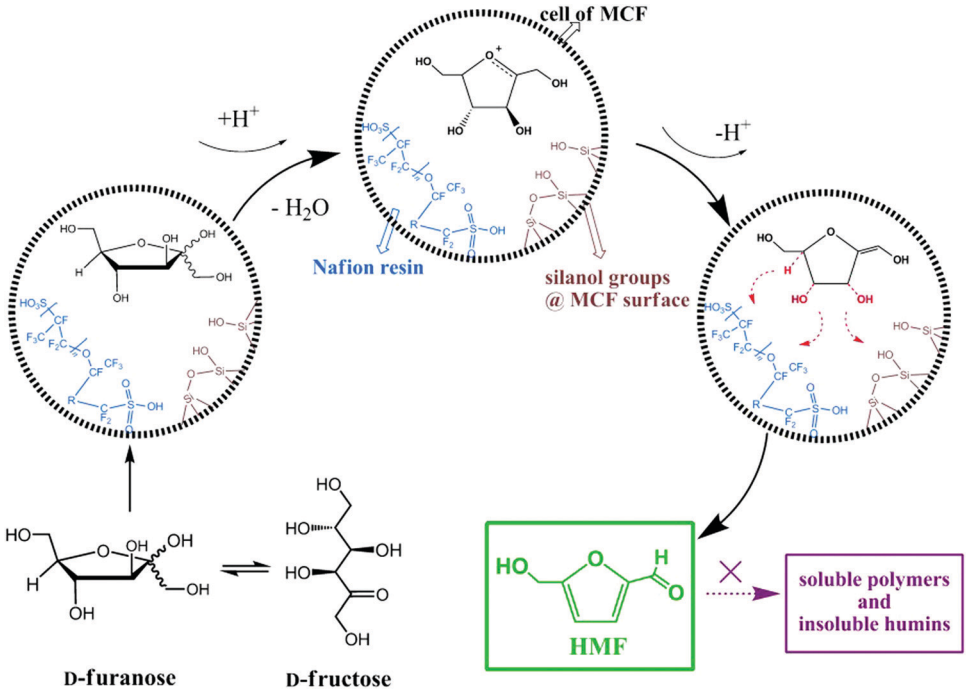

Fig. 22 Mechanism for the dehydration of fructose to HMF over Nafion-modified MCF catalysts. Reproduced with permission from ref. 211. Copyright (2013) John Wiley and Sons.

from steam reforming of glycerol. Notably, the Co/Ce-SBA-15 catalyst displayed a higher glycerol conversion with large amounts of hydrogen production, which was attributed to smaller Co crystallites, improved metal dispersion, and stronger metal–support interactions. The catalytic efficiency of Cu/SBA-15 for the vapor phase hydrogenolysis of glycerol to propanediols was strongly dependent on the Cu loading (2.5 to 20 wt%).[216] Highly dispersed copper oxide species were formed at lower Cu loadings ($\leq$5 wt%). As well, the acidity of the catalysts increases with the increase of Cu loading up to 5 wt% and then decreases at higher Cu loadings. As a result, the 5 wt% Cu/SBA-15 catalyst exhibited higher glycerol conversion (90%) with 84% selectivity to 1,2-propanediol (entry 2, Table 6). Hydrogen can also be produced *via* steam reforming of propylene glycol, a major product obtained from glycerol hydrogenolysis reaction. Various promoters, such as CeO_2, ZrO_2 and CeO_2–ZrO_2 were added to enhance the activity of Ni/SBA-15 catalyst in propylene glycol reforming.[217] The incorporation of CeO_2 and ZrO_2 effectively controlled the size of Ni particles. The promoted Ni/SBA-15 catalysts indicated superior activity and long-term stability compared to the pristine Ni/SBA-15 catalyst, which was attributed to the strong Ni-promoter interaction and the confinement effect of SBA-15 support. The presence of surface oxygen species in CeO_2 and ZrO_2 assisted to suppress carbon deposition, hence improved long-term catalytic performance of promoted Ni/SBA-15 catalyst in propylene glycol reforming.

3.4.3 Upgrading of biofuels. In this section, the catalytic upgrading of biofuels, such as bioethanol and lignin-derived fuel grade chemicals was discussed. Chae *et al.*[218] examined the effect of pore organization of various silicas in tuning the catalytic activity of tantalum oxide for the conversion of ethanol–acetaldehyde mixture to butadiene. Results revealed that compared to pore dimension and pore shape, pore size of silicas (especially in the range of 8–11 nm) shows a great influence on the efficiency of tantalum oxide towards 1,3-butadiene production. This is because larger pores are less prone to deactivation by coking. Mesocellular siliceous foam (MCF) was demonstrated to be a fascinating support for dispersing copper and zirconium oxide clusters towards ethanol-to-butadiene transformation in a dual-bed catalytic system.[219] In the first catalytic bed reactor, Cu/MCF catalyst was used to convert ethanol feed into ethanol–acetaldehyde mixture, which is subsequently converted into butadiene over Zr/MCF catalyst. Fine-tuning of Zr content in Zr/MCF catalyst led to a high butadiene selectivity (70%) at almost full ethanol conversion, together with an excellent stability for at least 120 h catalytic run. In ternary Ag/MgO–SiO_2 catalysts, synthesized by varying Ag content and SiO_2 source (commercial silica gel, MCM-41, and COK-12), both Ag species and basic sites (Mg–O pairs and basic OH groups) are crucial for 1,3-butadiene production from ethanol.[220] Metallic Ag species catalyze the ethanol dehydrogenation to acetaldehyde, while the subsequent aldol condensation is catalyzed by basic sites. On the other hand, only acetaldehyde was obtained during both dehydrogenation and oxidative dehydrogenation of ethanol over Ag/SiO_2 and Ag/CeO_2/SiO_2 catalysts.[221] The addition of CeO_2 improved the activity of Ag/SiO_2 catalyst in ethanol dehydrogenation, because of the increased amount of active sites or the spillover of active oxygen species from ceria to the Ag–CeO_2 interface. The formation of 1,3-butadiene was not observed in this work, which could be due to the lack of basic sites in Ag/CeO_2/SiO_2 catalyst.

The effect of direct growth of isolated α-MoC_{1-x} NPs (1.9 ± 0.4 nm) inside the pores of mesoporous SBA-15 was investigated for the hydrodeoxygenation (HDO) of acetic acid.[222] The resulting catalysts are bi-functional, and exhibit both H_2-activating sites and acid sites, with adequate amounts of stronger acidic sites when compared to the bulk α-MoC_{1-x} and β-Mo_2C. Owing to its greater acid-site : H-site ratio, the α-MoC_{1-x}/SBA-15 catalyst showed excellent decarbonylation selectivity in the HDO of acetic acid. Compared to Ru particles supported on conventional SiO_2, Ru/SBA-15 catalyst (0.2–2 wt% Ru) was found to display a good activity for the aqueous phase hydrogenation of three bio-based molecules: acetol, 2-butanone, and methyl 2-acetamidoacrylate.[223] High dispersion of Ru NPs, unique structure of SBA-15, along with improved reducibility of the oxidized surface layer formed at the surface of Ru metal nanocrystals are vital for achieving high product yields from all three bio-based molecules.

Various aromatic chemicals, including benzene, toluene, xylenes, phenol, cresols, and alkyl phenols were obtained from the hydroprocessing of lignin pyrolysis vapors carried out over a mesostructured Fe/SiO_2 catalyst.[224] Owing to larger mesoporous dimensions, Fe/SiO_2 catalyst inhibited the accumulation of carbon particles, whereas coke deposits completely blocked the micropores in Fe/activated carbon catalyst. The activity of Fe/SiO_2 catalyst could be regenerated by a controlled oxidation process, which can remove carbon deposits and reduce iron in sequential fixed or fluidized beds. The Co/SBA-15 catalyst is selectively promoted the hydrogenolysis of methoxy functional group of anisole.[225] In contrast, hydrogenation of aromatic ring of anisole to methoxycyclohexane was found in the presence of Ni/SBA-15 catalyst because of high hydrogenation ability of nickel species. Yang *et al.*[174] revealed the effect of Ce/Si molar ratio (from 0 to 0.08) on the efficiency of Ni/Ce-SBA-15 catalyst for the vapor phase HDO of anisole. Incorporation of Ce enhances the Ni dispersion and the specific active sites in 5% Ni/Ce-SBA-15 (Ce/Si = 0.03), resulting in improved yields of benzene (entry 3, Table 2). Both the metal dispersion (Co and Ni) and the metal–support interaction were strongly dependent on the support nature (SBA-15 and Al-SBA-15).[226] Compared with Co-based catalysts, 5 wt% Ni catalyst supported on Al-SBA-15 provided higher anisole conversion (99.8%) with 95% selectivity to cyclohexane (entry 4, Table 2). The strong interaction of Co with the support hinders the total Co reduction prior to the reaction, and hence a lower activity in the HDO of anisole.

Surprisingly, monometallic Co/Al-MCM-41 catalyst was found to show high activity in terms of deoxygenation products yield for the vapor phase HDO of guaiacol, compared to bimetallic Co–Ni/Al-MCM-41 catalyst (10 wt% of total metal loading).[227] This was attributed to nickel's ability to promote multiple hydrogenolysis of guaiacol C–C bonds, leading to carbon loss *via* methanation, especially at high temperatures. On the other hand, Ambursa *et al.*[228] demonstrated the favorable effect of both bimetallic interactions and incorporated metal for the liquid phase HDO of guaiacol over Cu–Ni/Ti-MCM-41 catalysts (entry 5, Table 2). The incorporation of Ti into the catalyst matrix led to abundant acid-redox properties and enhanced metal dispersion. As a result, 10 mol% CuNi/TiMCM-41 (Cu : Ni = 3 : 1) catalyst presented 90% guaiacol conversion and 50% cyclohexane selectivity, outperforming the unpromoted CuNi/MCM-41 catalyst. Hamid *et al.*[175] also investigated the effect of Ti amount (Ti/Si = 10, 20 and 30%) on the structure–activity properties of bimetallic Cu–Ni/Ti-MCM-41 catalysts for the liquid phase HDO of guaiacol. Although Ti loading indicated an adverse effect on the BET surface area, large amounts of acid sites and better redox properties were found for a 20% Ti loaded Cu–Ni/Ti-MCM-41 catalyst, which gave 74.2% guaiacol conversion with 48.8% cyclohexane selectivity. The authors propose that acid sites initiate the removal of oxygen *via* dehydration, while redox sites promote hydrogenation of guaiacol to cyclohexane. A continuous-flow strategy was developed for the vapor phase HDO of guaiacol over M/Al-MCM-41 (M = Co and Ni) catalysts (entry 6, Table 2).[229] The acidic Al-MCM-41 support stimulates the methyl transfer reaction to obtain methylated products. The Co/Al-MCM-41 catalyst is particularly selective towards C–O hydrogenolysis of guaiacol to obtain phenol. Compared with a conventional Ni/γ-Al_2O_3 catalyst, the 10 wt% Ni catalyst supported on mesoporous SiO_2 (broad pore size distribution) exhibited high hydrocarbon yields and excellent catalytic stability for the liquid phase HDO of lignin-derived compounds.[230] The Ni/SiO_2 catalyst preferentially promotes the hydrogenation of aromatic rings to yield fuel grade hydrocarbons.

3.5 Sulfated mesoporous silica catalysts

Sulfated mesoporous silica catalysts not only combine the unique characteristics of individual candidates, but also endow new catalytically active sites, depending on the configurations of sulfate species on porous channels of silica. Particularly, these materials can show both Lewis and Brønsted acid properties due to the existence of metal centers and the immobilized $–SO_3H$ species, respectively, which could play a vital role in acid-catalyzed biomass conversions. Impregnation, grafting or immobilization have been largely used for the synthesis of these type of materials.[179]

Many efforts have been undertaken to develop efficient sulfated mesoporous silica catalysts for the production of various bio-based chemicals, including 5-hydroxymethylfurfural (HMF). For instance, Cheng *et al.*[77] revealed the beneficial role of a sulfated mesoporous silica, synthesized by impregnation of H_2SO_4 on MCM-41, followed by calcination at 550 °C, for the dehydration of fructose to HMF. Owing to well-balanced pore size and acidity, the sulfated mesoporous silica afforded about 90% HMF selectivity at 94% fructose conversion (entry 9, Table 1). The combination of a $–SO_3H$ functionalized mesoporous silica and an immobilized enzyme with $–NH_2$ functionalized mesoporous silica is greatly useful for the direct conversion of glucose to HMF.[231] About 61% and 30% yields of fructose and HMF, respectively, were obtained in a monophasic solvent system composed of tetrahydrofuran and H_2O (4 : 1 v/v). Catalyst preparation method exhibited a great effect on the performance of sulfated mesoporous silica for fructose-to-HMF transformation.[232] Markedly, the sulfated MCM-41 catalyst prepared by H_2SO_4 impregnation, followed by calcination at 550 °C provided 98%

and 77% fructose conversions with 94% and 88% HMF selectivities when using 10% and 30% concentrations of fructose, respectively. Owing to abundant Brønsted acid sites, KIT-5-SO_3H catalyst gave higher yields of HMF (94%) from fructose dehydration in liquid phase, while the Al incorporated KIT-5 catalyst afforded a 88.3% HMF yield (entry 10, Table 1).[233]

Several mesoporous silica materials coated by functionalized carbon with –SO_3H or –COOH species were investigated for the production of useful bio-based chemicals.[234] The resulting catalysts with abundant acid site content and strength displayed good yields of furanic ethers and levulinate esters from HMF, fructose, and furfuryl alcohol with ethanol. Owing to favorable textural properties and enhanced active site accessibility, these mesoporous catalysts showed higher reaction rates than Amberlyst™-15 (on the same catalyst mass basis), carbon based catalyst, aluminosilicate, non-porous silica and H-β zeolite. Manayil *et al.*[235] developed octyl co-grafted $PrSO_3H$/SBA-15 solid acids for the esterification of acetic acid with methanol. Results revealed that turnover frequencies for the targeted reaction improved with the increase of both surface acid site density and hydrophobicity of the catalysts. The nature of the acidic group (–SO_3H, –SO_3H/C_2H_5, –COOH, and –CN) has a huge effect on the activity of mesoporous silica for the transesterification of triglycerides to produce biodiesel.[236] Among them, SBA-15/SO_3H catalyst was found to be highly efficient for biodiesel production, which was attributed to high concentration of acid sites.

4. Nanoscale metal/metal oxide based catalysts for biomass valorization

Metals, metal oxides, or combinations of both are the most widely used heterogeneous catalysts in several industrially important applications, including auto-exhaust purification,[237,238] petrochemicals production, as well as in biomass valorization.[23,37,239] The ability of metals to exhibit multiple stable oxidation states is the primary factor for their widespread catalytic applications, especially in oxidation and hydrogenation processes. The coupling of a metal with another metal or metal oxide could lead to improved redox properties due to the synergistic metal–metal interactions, stimulated by the interplay of electron transfer at the interface structures. The addition of Cu, Ni or Co to Mo/Al_2O_3 catalyst, for instance, led to an enhanced reducibility, which played a crucial role for the formation of allyl alcohol with respect to hydroxyacetone in glycerol dehydration reaction.[240]

The performance of a solid catalyst is greatly dependent on its outermost surface composition and geometry.[241] Hence, fine-tuning the energy distribution and electronic structure of the catalyst surface could control the activation energy barrier and determine the catalyst activity/selectivity.[242] Several crucial parameters have been suggested for precise modification of the catalyst surface, both electronically and geometrically (Fig. 23).[23] Particularly, when the size of a catalyst particle is reduced to nanoscale range (1–100 nm in at least one dimension), the textual and redox properties at the catalyst surface can be greatly augmented, which can provide unusual catalytic activities. A classic example to illustrate this size-dependent effect is gold, which is considered as catalytically inactive in the bulk state, due to its insignificant chemisorption and redox properties. In contrast, uniformly dispersed gold nanoparticles (2–5 nm) on a metal oxide exhibit outstanding catalytic activity for several oxidation reactions.[243–249] This pronounced size-dependent catalytic performance was evaluated based on the enhanced surface electronic and geometric properties of the smaller sized gold nanoparticles.[250] In addition, shape-controlled nanoscale metals/metal oxides can provide exceptional catalytic properties because of the co-operative effect of size- and shape-dependent properties.[250,251] In this section, the most important properties of metals, metal oxides, and metal oxide supported metals are highlighted, while discussing their ensuing catalytic effects in biomass valorization. For a deeper understanding, the catalytic performance of nanoscale metals/metal oxides achieved in biomass conversions is compared with that of the corresponding bulk analogues.

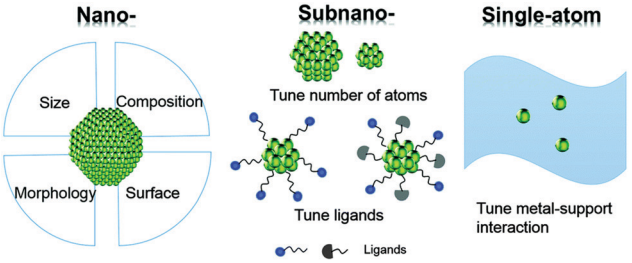

Fig. 23 Illustration of key parameters for the synthesis of nanoscale metal catalysts. Reproduced with permission from ref. 23. Copyright (2016) Royal Society of Chemistry.

4.1 Nanostructured metals

Mono- and bi-metallic nanoparticles have gained unprecedented importance in catalysis because of their energetic structural and redox properties that could be substantially differ from their bulk counterparts.[14,23,239,252,253] An active site in a metal catalyst could be a single atom or a collection of atoms that directly participate in a catalytic reaction through chemical bond cleavage and formation, during which the neighboring atoms could influence the energetics of these processes.[254] The variation of particle size and surface structure of a metal catalyst can markedly affect the coordination number of surface metal atoms.[255] Consequently, nanoscale metal particles contain a high percentage of coordinatively unsaturated atoms located preferentially at the surface, edges, or corners. Low coordinated atoms are highly energetic and can readily participate in catalytic redox processes because of their strong tendency to coordinate with reactant molecules in their vicinity.[255]

Catalytic oxidation is one of the widely used methods for biomass valorization.[256,257] The catalytic activity of metals in oxidation reactions is mainly determined by their affinity towards adsorbing molecular oxygen or other oxidants (*e.g.*, H_2O_2). The estimated adsorption energy profiles revealed that oxygen could make strong bonds with metals present on the left side of

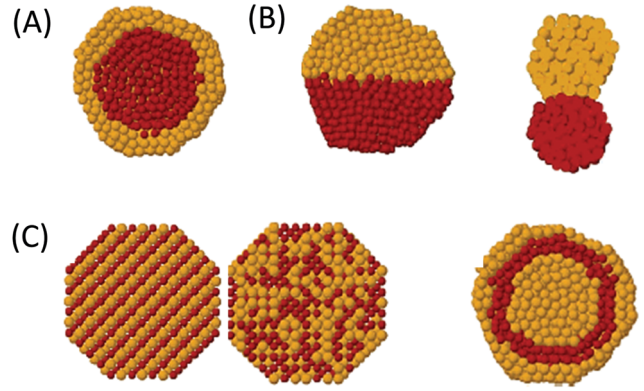

Fig. 24 Schematic representation of some possible mixing patterns of nanoalloys: (A) core–shell, (B) subcluster segregated, (C) mixed, and (D) three shell. The pictures show cross sections of the clusters. Reproduced with permission from ref. 263. Copyright (2008) American Chemical Society.

transition metal series. Moreover, oxygen shows a strong affinity towards 3d metals compared to 4d and 5d metals.[258] Accordingly, Ru binds the oxygen much stronger than Pd and Ag, while Au exhibits weak binding energy per oxygen atom, which is even less than the binding energy of O_2 molecule.[259] However, by reducing the size of the metal to nanoscale, the oxygen adsorption efficiencies can be improved, as observed perceptibly in the case of Au NPs.[28,260,261] Hence, the selection of a metal catalyst for oxidation reactions not only depends on its position in the Periodic table, but also on its size-dependent properties.

The coordination of a metal with another metal can lead to new, selective catalytically active sites due to synergistic metal–metal interactions.[262] In addition, the presence of an another metal can improve catalyst stability against adverse conditions, including low or high pH and aqueous or oxygen environments. Such synergistic interactions could be more pronounced in nanoalloy catalysts, as the probability of metal–metal interactions increases with enhanced electron sharing and larger surface areas.[262,263] Based on the mixing pattern and geometric structure, nanoalloys can be classified as core–shell (A), subcluster segregated (B), mixed (C), and three shell (D) nanoalloys (Fig. 24).[263] Interestingly, the particle size also influences the ability to form nanoalloys. Fe and Ag, for example, are immiscible in the bulk state, but they readily form alloys in a finite nanocluster state.[263]

4.2 Nanostructured metal oxides

Metal oxides, that can play the role of both active phase as well as catalyst support, are essential components for the development of several industrial heterogeneous catalysts.[264–266] Particularly, transition and inner transition metal oxides occupy a paramount place in heterogeneous catalysis as they exibit vastly diverse configurations and fascinating properties. The catalytic activity of metal oxides is dependent mainly on three parameters: (1) acid–base strength, (2) oxygen vacancy defects, and (3) hydrothermal stability.[264,267,268] The acid- or base-strength of metal oxides is largely dependent on charge-to-radius ratio of cations and the metal oxide phase. For example, Ce^{4+} exhibits a higher acidic-strength than Ce^{3+} because of the higher charge-to-radius ratio (Ce^{4+}), and hence pure ceria (CeO_2) is acidic in nature.[268–270] Metal oxide phase can also influence the acid–base strength and the catalytic performance as evidenced for TiO_2 and ZrO_2 catalysts.[271] Anatase TiO_2 containing adeque amounts of acid–base sites was able to catalyze glucose-to-HMF reaction, while rutile TiO_2 has no significant effect at similar reaction conditions. In the case of ZrO_2, monoclinic/tetragonal mixed phase exhibited good catalytic activity in isomerization of glucose to fructose, due to the presence of abundant basic sites in mixed phase oxide.

The presence of oxygen vacancies in metal oxides can influence their catalytic activity/selectivity in biomass upgrading. Oxygen vacancy defects can be generated during synthesis process, catalytic reaction, or by post-synthesis hydrogen treatment.[272–274] Oxygen vacancies and the corresponding reduced metal centers could play a beneficial role in lowering the activation energy barriers and stabilizing reaction intermediates, leading to improved biomass conversion rates. Xiao *et al.*[273] demonstrated that oxygen vacancies present in reducible metal oxides could act as the active sites for biomass deoxygenation reactions. They found that oxidized zinc (without oxygen vacancies) was almost catalytically inactive (Fig. 25a), while the presence of oxygen vacancies led to an enhanced deoxygenation of bio-derived acetic acid to acetaldehyde (Fig. 25b). The significance of oxygen vacancies in biomass valorization is also noticed over other metal oxides, such as TiO_2 and ZrO_2,[274] MoO_3,[275] CeO_2,[276] and CeO_2–ZrO_2.[277] An added benefit of oxygen vacancies is their mild acidic strength that can direct a specific reaction pathway towards the formation of desirable bio-based chemicals. For example, compared to the hydrogenation route the direct deoxygenation of lignin-derived compounds is greatly favored over oxygen vacancy sites (acid sites) of MoO_3.[278]

Mixed oxides composed of two or more different metals can exhibit unusual catalytic efficiencies compared to individual metal oxides. This is because of their attractive acid or base, redox, and surface area properties, enriched by cooperative metal–metal interactions.[264,268,278] As stated previously, pristine ceria contains a high number of acid sites. However, incorporation of lower valent cations (*e.g.*, La^{3+} or Mg^{2+}) into the ceria lattice can generate considerable amounts of basic sites due to the variation in the charge-to-ionic radii of Ce^{4+} (0.097 nm) and La^{3+} (1.10 nm) or Mg^{2+} (0.072 nm). Concurrently, it must be noted that the strong basicity of the doped species may show a negative effect on catalyst's performance, since the basic centers often tend to donate their electrons to the adjacent electron acceptors (acidic centers). As a result, the oxidizing ability of the active components will decrease, leading to low catalytic activity in biomass oxidation reactions. Mixed oxides can also show enhanced oxygen mobility and textural properties (particle size and surface area) due to the synergistic interactions of heteroatoms, as noticed in the case of CeO_2–ZrO_2 mixed oxide.[245,277,279–281] Consequently, CeO_2–ZrO_2 mixed oxides were found to be catalytically active in various biomass upgrading reactions, such as ketonization of carboxylic acids and esters,[279] hydrodeoxygenation of guaiacol,[277] and deoxygenation of oleic acid.[282]

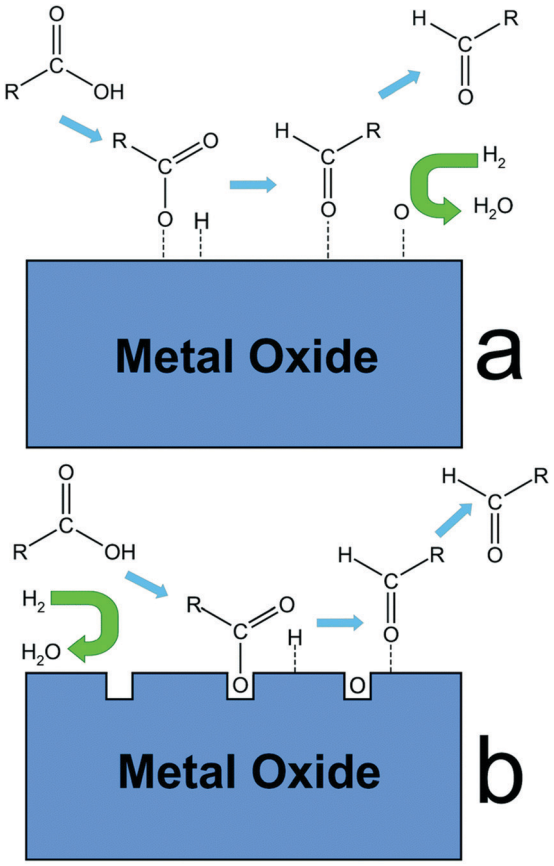

Fig. 25 Mechanisms for the deoxygenation of bio-derived acetic acid over zinc oxide. (a) Surface-driven mechanism: acetic acid molecules adsorb on the catalyst surface to react with hydrogen. (b) Vacancy-driven mechanism: catalyst facilitates the dissociative adsorption of the acetic acid molecules through the vacant site on the catalyst surface. Reproduced with permission from ref. 273. Copyright (2018) Royal Society of Chemistry.

Hydrothermal stability of metal oxides is another attractive property that boosts their catalytic applications in biorefinery research since most biomass conversions are often carried out at harsh hydrothermal conditions and sometimes in sub- or super-critical liquid environments.[283,284] Xiong *et al.*[284] evaluated the stability of various solid materials including metal oxides under superheated steam conditions (Fig. 26). It was demonstrated that TiO_2, ZrO_2 and CeO_2–ZrO_2 exhibit higher hydrothermal stabilities for biomass gasification in supercritical water, while silica and activated carbon were unsuitable for this reaction.[285] The improved hydrothermal stability of mixed oxides (silica–alumina) in comparison to pristine metal oxides was also noticed in cellobiose hydrolysis at 200 °C.[286]

4.3 Nanostructured metal/metal oxide catalysts

Despite of their interesting structural and redox properties, it remains a great challenge to control the aggregation of metal nanoparticles at high temperature conditions during catalyst synthesis or catalytic reaction, resulting in lower catalytic efficiencies. A plausible solution to circumvent this problem is to deposit metal nanoparticles on a high surface area

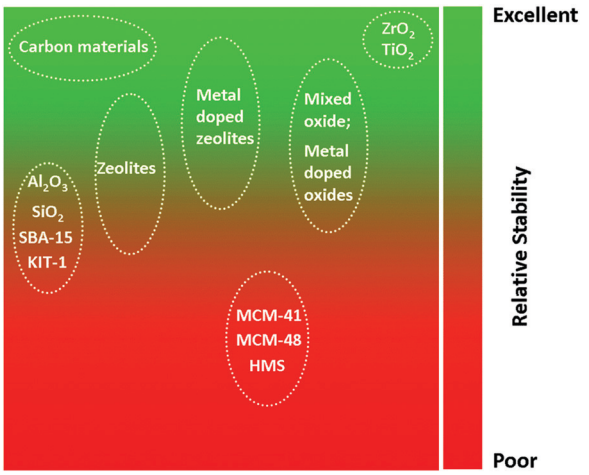

Fig. 26 Hydrothermal stability of different heterogeneous solid catalysts in superheated steam conditions (T > 400 °C). Reproduced with permission from ref. 284. Copyright (2014) Royal Society of Chemistry.

metal oxide.[287–290] The aim of using this route is to obtain uniformly dispersed metal nanoparticles and to improve their stability *via* strong metal–support interactions.[287] Tauster *et al.*[291] introduced this metal–support interaction concept and emphasized the importance of the support role in enhancing the properties of metal nanoparticles.

In addition to specific surface area, the morphology of metal oxides can play a significant role in tuning the structure–activity performance of supported metal catalysts. For example, ceria can form different nanosized shapes with preferentially exposed crystal facets, such as nanocubes ({100}), nanorods ({110} & {100}), and nanopolyhedra ({111} & {100}).[292–297] These shape-dependent crystal facets can selectively influence the surface active sites, such as oxygen vacancies and redox couple (Ce^{4+}/Ce^{3+}). Hence, unusual catalytic activities can be achieved when a transition metal is deposited on these shape-controlled metal oxides. The importance of these shape-controlled ceria supports is evident in various biomass upgrading reactions, such as production of acrylic acid from glycerol,[292] oxidative transformation of 1,3-propanediol into methyl esters[293] and hydroprocessing of rice straw biomass.[276]

Heterogeneity of particle size distribution is a key concern of conventionally synthesized supported metal catalysts, which not only adversely affects the atom efficiency, but also enables unwanted side reactions.[245,246,248,298,299] Uniquely identifying and controlling the location of active metal centers is also quite difficult in conventional supported metal catalysts, however it is essential to promote a specific reaction pathway towards desirable chemicals. In this context, the development of heterogeneous single-atom catalysts, also denoted as SACs, consisting of isolated metal atoms singly dispersed on supports, has recently attracted much attention for several catalytic applications including biomass upgrading. These novel catalytic systems can maximize the efficiency of metal atoms and offer great potential for achieving exceptional catalytic activity/selectivity compared with that of conventional supported metal catalysts.[299]

4.4 Valorization of lignocellulose biomass

Reductive catalytic fractionation (RCF) is a promising process for the full exploitation of lignocellulosic biomass to lignin oil (phenolic monomers, dimers, or oligomers) as well as a solid hemi(cellulose) pulp for paper, chemicals or fuels production. The Sels group has made substantial advances in RCF process to improve lignin oil yield and selectivity of the phenolic monomers.[300] For instance, they developed a potential RCF process for the valorization of birch wood in supercritical methanol using Ni–Al_2O_3 catalyst pellets.[301] The catalyst was placed in a reactor basket to allow facile catalyst recovery/reusability and hence, catalyst-free pulp production. About 90% delignification of birch wood was achieved and the obtained lignin oil contained over 40% phenolic monomers with a high selectivity to 4-*n*-propanolguaiacol and 4-*n*-propanolsyringol products. The catalytic efficiency of spent Ni–Al_2O_3 pellets could be regenerated by applying a simple thermal H_2-treatment. The delignified carbohydrate pulp was used to produce bioethanol (73% yield) through simultaneous enzymatic saccharification and yeast fermentation. RANEY® nickel or spongy nickel, a fine-grained nickel solid derived from a Ni-Al alloy, showed good activity in RCF process of lignocellulose using 2-PrOH as a hydrogen-donor.[302] The key advantage of this process is that RANEY® Ni can be efficiently removed from the reaction mixture using a magnet. The catalyst-free carbohydrates pulp can thus be subsequently used for the production of glucose and xylose *via* enzymatic hydrolysis. In another work, the combination of RANEY® Ni with NaOH is used for the transformation of various biomass sources (fir, pine, bamboo, and corncob) into bio-oil in a 2-propanol/H_2O system.[303] The conversion of biomass could reach up to 97–99% at optimized reaction conditions. In the case of fir feedstock, about 64% yield of bio-oil and a heating value of 30.1 MJ/kg were achieved. Results revealed that NaOH is crucial to achieve higher yields of bio-oil and RANEY® Ni can catalyze the subsequent removal of oxygen species in bio-oil *via* hydrodeoxygenation reaction.

Tathod *et al.*[304] observed the beneficial effect of Sn in Pt/γ-Al_2O_3 catalyst towards sugar alcohols production from agricultural waste (bagasse, rice husk, and wheat straw). Compared to carbon support, high yields of sugar alcohols were obtained over γ-Al_2O_3 supported PtSn catalysts. The PtSn/γ-Al_2O_3 catalyst was also able to convert mono- (glucose, fructose, xylose, arabinose, and galactose) and poly-saccharides (xylan, arabinogalactan, and inulin) into sugar alcohols. The presence of electron deficient Sn species, which helped in polarizing carbonyl bonds of sugars, was the key factor for improved performance of supported PtSn catalysts. He *et al.*[305] proposed a potential strategy for the direct conversion of raw corn stover to lactic acid using ethanol/H_2O and oxalic acid in the presence of MgO catalyst. Results revealed that ethanol/H_2O solvent system could efficiently fractionate corn stover into 88 wt% of hemicellulose and 89.2 wt% of lignin, while retaining a stable cellulose pulp. Oxalic acid played a favourable role in the cleavage of intermolecular linkages between hemicellulose and lignin. On the other hand, MgO catalyzed the conversion of dissolved hemicellulose derivatives to lactic acid with 79.6 wt% yield and 90% selectivity. In recent work, the hydro-liquefaction of rice stalk to bio-crude oil was carried out by means of hydrogen generated *in situ* during the oxidation of aluminium (gives Al_2O_3) under supercritical ethanol conditions.[306] The generated Al_2O_3 can also act as a catalyst for the transformation of ethanol to provide additional H_2 for the hydro-liquefaction of rice stalk. About 75% energy recovery and 33 wt% yield of bio-oil were achieved at optimized conditions. Ni nanoparticles dispersed on CeO_2 nanorods, synthesized by a one-pot hydrothermal method, exhibited good catalytic activity in hydroprocessing of rice straw biomass.[276] Shape-controlled CeO_2 nanorods preferentially expose a large fraction of reactive (110) and (100) crystal planes, which can provide a high concentration of redox active sites.[269,307] Ni/CeO_2 catalyst with a Ni/Ce molar ratio of 2/10 afforded 89% conversion of rice straw and 66.7% yield of bio-oil, which was attributed to homogeneous dispersion of Ni metal sites and abundant oxygen vacancies in cerium oxide.[276] Biomass to MoO_3 mass ratio played a pivotal role on the deoxygenation activity of MoO_3/TiO_2 and MoO_3/ZrO_2 catalysts (10 wt% MoO_3 loading) for catalytic fast pyrolysis of pine biomass.[56] Owing to adequate amounts of surface reduced Mo species (Mo^{3+} and Mo^{5+}), the supported MoO_3 catalysts converted approx. 27 mol% of the original carbon into hydrocarbons, mainly containing aromatics (7 C%), olefins (18 C%), and paraffins (2 C%), outperforming a bulk MoO_3 catalyst.

4.5 Upgrading of carbohydrates and their derived compounds

In this section, the catalytic processing of polysaccharides (cellulose and hemicellulose), monosaccharides (glucose and xylose), and their derived compounds (alcohols, acids, esters, and furans) is discussed.

4.5.1 Catalytic hydroprocessing reactions. Ethylene glycol (EG) and 1,2-propylene glycol (1,2-PG) are very important chemicals for polymer, antifreeze, and fine chemical industries.[308] About 23 million tons of EG and 1.8 million tons of 1,2-PG were produced in 2015, and this productivity is expected to increase at a rate of 5% in the following 10–20 years. EG and 1,2-PG are currently produced from petroleum-derived ethylene and propylene, respectively, *via* selective formation of epoxy compounds. An alternative potential process for the synthesis of EG and 1,2-PG chemicals is one-pot hydrogenolysis of cellulose, which is an acid-redox site-catalyzed reaction. Hence, the combination of acid sites (*e.g.*, WO_3 based solid acids) with redox sites (metal catalysts) is of great importance for cellulose hydrogenolysis. Tai *et al.*[309] revealed that, for instance, RANEY® Ni catalyst coupled with tungsten based solid acids, including WO_3 play a prominent role in the conversion of cellulose to EG in liquid phase. However, WO_3 was found to dissolve partially under the reaction conditions, forming a homogeneous H_xWO_3 compound, which could be the catalytically active phase for the selective cleavage of C–C bonds in cellulose to yield EG product. In relation to catalyst reusability and process costs, the use of a single versatile catalyst having both acid and redox properties would be preferable rather than using two catalysts. In addition, multicomponent catalysts could exhibit improved stability due to the presence of strong metal–metal interactions. In view

of these benefits, Ru/Zr–W–O catalysts, which exhibit high hydrothermal stability at 220 °C and 65 bar H_2, were developed for the liquid phase hydrogenolysis of cellulose.[310] About 31.9% and 4.5% yields of EG and 1,2-PG, respectively, were obtained over 4.5 wt% Ru/Zr–W–O catalyst at optimized reaction conditions.

Selective hydrogenation of monosaccharides, such as glucose into 1,2-PG and EG was also studied using a variety of nanoscale metal/metal oxide catalysts. It was pointed out that both Lewis acid and metal sites in Pd–WO_x/Al_2O_3 catalysts are vital to achieve high yields of 1,2-PG from glucose.[311] In contrast, Brønsted acid sites surprisingly have no contribution in the 1,2-PG production. The Pd–WO_x(5 wt%)/Al_2O_3 catalyst, which has well-balanced Lewis acid and metal sites, afforded 92.2% glucose conversion and 60.8% 1,2-PG selectivity. A combined experimental and computational study was performed to understand the role of the support (MgO and ZnO) on the performance of Ni-based catalysts for the selective conversion of glucose into 1,2-PG and EG products.[312] Remarkably, the MgO support promoted glucose conversion into fructose as well as the subsequent retro-aldol reaction of fructose at the C3–C4 position, resulting in high yields of 1,2-PG. The production of C3 polyols, including EG and 1,2-PG, from sorbitol was also studied over Cu/CaO–Al_2O_3 catalysts.[313] By optimizing several parameters, such as Cu loading, catalyst pre-treatment, reaction temperature, and H_2 pressure a combined selectivity of 84% to glycols and linear alcohols was obtained with Cu/CaO–Al_2O_3 catalyst. A possible reaction mechanism involving β-ketose formation on Cu–Ca^{2+} sites was proposed. The significance of metal–metal interactions in tailoring the efficiency of bimetallic Pd–Cu/ZrO_2 catalysts was markedly noticed in sorbitol hydrogenolysis.[314] A combined selectivity of 61.7% to EG, 1,2-PG, and glycerol was obtained at nearly 100% sorbitol conversion over Pd–Cu/ZrO_2 (Cu/Pd = 5) catalyst, outperforming monometallic counterparts. Sugar alcohols (xylitol and arabitol) have plentiful applications in food, oral hygiene, and pharmaceutical industries. These sugars can be selectively synthesized *via* hydrogenolysis of xylose (monosaccharide) and hemicellulose (xylan, polysaccharide) over supported MP catalysts (M, metal = Pt & Ru and P, promoter = Sn, Ga, & Fe).[315] Three supports, namely γ-Al_2O_3, SiO_2–Al_2O_3, and carbon were used in this work. Among these catalysts, Pt(3.5)Sn(0.43)/γ-Al_2O_3 catalyst showed good activity with a 2.8 times higher yield of sugar alcohols from a polysaccharide compared to the corresponding monometallic Pt(3.5)/γ-Al_2O_3 catalyst. The improved activity of bimetallic catalysts is due to the existence of electron deficient Sn species, which promote polarization of the carbonyl groups, resulting in high yields of sugar alcohols. In addition, Pt(3.5)Sn(0.43)/γ-Al_2O_3 catalyst is efficiently reused for five cycles without considerable loss in catalytic activity. NiO addition has a great effect on the performance of Ru/TiO_2 catalyst for the liquid phase xylose hydrogenation.[316] Particularly, Ru(1%)/NiO(5%)–TiO_2 catalyst showed excellent performance in terms of xylose conversion (99.9%) and xylitol selectivity (99.8%), outperforming Ru/TiO_2, Ru/C, and RANEY® Ni catalysts.

The catalytic hydrogenation of levulinic acid (LA), a key platform chemical derived from carbohydrates, into γ-valerolactone (GVL) is one of the most crucial reactions in bio-refinery industry.[317,318] Various nanostructured metal/metal oxide catalysts were developed for LA-to-GVL transformation. Ftouni *et al.*[318] observed durable performance of Ru/ZrO_2 catalyst towards GVL production even after multiple recycling tests. In contrast, Ru/TiO_2 catalyst showed an abrupt deactivation after the first catalytic test, which was due to undesirable reduction of TiO_2 in combination with partial coverage of Ru NPs on the support. The addition of water to the reaction mixture indicated a favorable effect in promoting the selective hydrogenation of LA to GVL product. Ru/ZrO_2 catalyst exhibited outstanding stability in liquid phase LA hydrogenation in the presence of H_2SO_4 impurity compared to Ru/carbon catalyst due to preferential adsorption of sulfate species on the surface of ZrO_2, preventing deactivation of Ru phase.[319] The significance of Ru/ZrO_2 catalyst in catalytic transfer hydrogenation of LA to GVL was also noticed.[320] An equimolar mixture of formate/formic acid in water was used as hydrogen source. Doping with 0.1 wt% SiO_2 was found to stabilize the tetragonal phase of ZrO_2, resulting in improved catalyst stability in the liquid phase LA hydrogenation, even after four recycles. Ru precursor ($RuCl_3$, $RuNO(NO_3)_3$, and $Ru(NH_3)_6Cl_3$) used for the catalyst synthesis has a profound influence on the structure–activity performance of Ru/TiO_2 (anatase) catalyst for the aqueous phase LA-to-GVL transformation.[321] Best results in terms of turn-over frequency (TOF) and initial rate based on Ru intake were obtained over the catalysts synthesized using $RuNO(NO_3)_3$ and $RuCl_3$ precursors, respectively. Alkali cations (Na^+, K^+, and Cs^+) exhibited a substantial effect on the activity of Ru/Al_2O_3 catalyst for the liquid phase hydrogenation of LA to GVL.[322] As the most polarizable cation, Cs^+ strongly enhances the electron density on the Ru metal surface, which is essential for achieving higher reaction rates in LA hydrogenation.

Nanostructured bimetallic Au–Pd/TiO_2 and Ru–Pd/TiO_2 catalysts, prepared by a modified wet-impregnation method, were found to show improved GVL selectivity compared to the monometallic analogues, which was attributed to synergistic effect of nano-alloying.[323] In addition, both supported nano-alloy catalysts showed exceptional stability in the liquid phase LA hydrogenation, even after three consecutive recycles. Al-Naji *et al.*[324] studied LA hydrogenation under microwave-assisted, batch scale, and continuous flow conditions using Ni–Pt and Ni–Ru catalysts supported on ZrO_2 and γ-Al_2O_3. Results revealed that Ni–Ru/γ-Al_2O_3 catalyst exhibits the highest LA conversion, due to the presence of high concentration of metallic Ru^0 species on the surface of γ-Al_2O_3, together with its improved textural properties. However, Ni–Ru/γ-Al_2O_3 catalyst suffered rapid deactivation after four consecutive catalytic runs. This can be explained by a drastic loss in specific surface area (from 259 to 53 m^2 g^{-1}) and pore volume (0.7 to 0.2 cm^3 g^{-1}). The transformation of γ-Al_2O_3 to a soluble boehmite phase (AlOOH) was also a key reason for the deactivation of Ni–Ru/γ-Al_2O_3 catalyst. Effects of both metal oxides (ZrO_2, Al_2O_3, Cr_2O_3, and BaO) and mixed oxides (Cr_2O_3–Al_2O_3 and BaO–Al_2O_3) on the activity of nanoscale Cu catalysts were investigated in the liquid phase hydrogenation of LA and its ester to GVL product.[325]

Among the supports studied, best catalytic results were obtained in the case of ZrO_2 and Al_2O_3 supported Cu catalysts. In addition, Cu/ZrO_2 catalyst can be reused for at least three cycles without much loss in catalytic activity. An efficient catalytic cascade strategy was developed for the synthesis of GVL, 1,4-pentanediol, and 2-methyl tetrahydrofuran from LA in water solvent using a $Pd–Cu/ZrO_2$ catalyst.[326] The addition of 1% Pd to 30% Cu/ZrO_2 catalyst significantly improved its catalytic stability, revealing the importance of nano-alloying in catalytic biomass upgrading. Furthermore, $Pd–Cu/ZrO_2$ catalyst exhibited good hydrothermal stability.

The catalytic vapor phase (or continuous-flow) hydrogenation of LA to GVL is a hot research topic because of its advantages (*e.g.*, low consumption of catalysts, waste minimization, cost efficiency, improved product quality, and the integration of downstream processes) over batch scale catalytic processes. Varkolu *et al.*[327] developed an efficient continuous-flow process for the selective hydrogenation of LA to GVL with formic acid as the hydrogen source. Among the catalysts tested, Ni/Al_2O_3 catalyst showed the best performance, which was attributed to high concentration of uniformly dispersed metallic Ni species on the surface of Al_2O_3 support. In another work, Varkolu *et al.*[328] demonstrated the role of preparation method (impregnation, co-precipitation, deposition–precipitation, and citric acid assisted impregnation combustion) on the performance of Ni/SiO_2 catalysts for LA hydrogenation. The authors found that Ni/SiO_2 catalyst prepared by citric acid assisted method followed by calcination in inert gas flow displays good catalytic performance in LA-to-GVL transformation, due to the presence of optimum porosity, along with highly dispersed Ni NPs. The effect of support (Al_2O_3, SiO_2, TiO_2, ZSM-5 and $SiO_2–Al_2O_3$) was evident on the structure–activity performance of Cu catalyst for the vapor phase hydrogenation of LA with formic acid as the hydrogen source.[329] Owing to strong metal–support interactions, the $Cu–SiO_2$ catalyst gave the highest LA conversion (56%) with 87% selectivity to GVL at 250 °C. The influence of both supports (SiO_2, γ-Al_2O_3 and ZrO_2)[330] and the promoter (W)[331] on the efficacy of Ni and Ni/TiO_2 catalysts, respectively, was observed for the vapor phase hydrogenation of aqueous LA to GVL. Pyridine adsorption DRIFT studies were undertaken to understand the role of Brønsted- and Lewis-acid sites in tuning GVL selectivity over Ni based catalysts.

Selective hydrogenation of furans (furfural and 5-hydroxymethylfurfural) is of great importance since the resulting products have a myriad of applications in the chemical industry.[332–334] Rogers *et al.*[335] developed tandem site- and size-controlled Pd NPs immobilized on TiO_2 for the hydrogenation of furfural to tetrahydrofurfuryl alcohol. The size of Pd NPs could be controlled by varying the temperature of the colloidal solution. However, no linear correlation was found between the Pd particle size and the product selectivity in furfural hydrogenation. Interestingly, a higher proportion of corner and edge sites, which are able to tune product selectivity in furfural hydrogenation, can be obtained by adjusting the solvent system (water–ethanol) of the colloid preparation. Both support nature (TiO_2, carbon, MgO, Fe_3O_4, and Al_2O_3) and Pt addition had a notable effect on the efficiency of Pd catalysts for the liquid phase hydrogenation of furfual.[336] The distribution of Pd–Pt nano-alloys on TiO_2 surface is shown in Fig. 27. Among the supports used, TiO_2-supported Pd catalyst exhibited the highest selectivity to tetrahydrofurfuryl alcohol. The activity of Pd/TiO_2 catalyst (Pd = 0.47 wt%) could be improved by Pt addition (0.49 wt%), giving 95% yield of tetrahydrofurfuryl alcohol, which was attributed to synergistic Pd–Pt interactions stimulated by facile electron transfer effects (entry 5, Table 3). Cu_xNi_y (x/y = 7 : 1, 3 : 1, 1 : 1, 1 : 3, 1 : 7) nano-alloys supported on Mg–Al–O mixed oxide were demonstrated to be efficient catalysts for the liquid phase furfural hydrogenation.[337] The reduction temperature of the catalyst precursor played a crucial role in tuning the dispersion and composition of CuNi nanoalloys as well as the surface basicity of catalysts, which are vital for achieving improved product yields (99%) in furfural hydrogenation (entry 6, Table 3). By tuning the metal composition as well as changing the reaction solvent, the selectivity of the catalyst could be changed from tetrahydrofurfuryl alcohol to furfuryl alcohol. King *et al.*[338] reported that Pd/TiO_2 catalysts are highly selective towards 2-methylfuran product in the liquid phase furfural hydrogenation. However, Sn addition (1 wt%) to Pd/TiO_2 catalyst led to a shift in product selectivity from 2-methylfuran to tetrahydrofurfuryl alcohol. This indicates the effect of Sn–Pd interactions in tuning product selectivity. An efficient catalytic process was developed for the direct conversion of furfural to cyclopentanone using CuZnAl mixed oxides.[339] Effects of Cu/Zn molar ratio and the calcination temperature towards cyclopentanone production were investigated. Notably, the CuZnAl-0.5 (Cu/Zn = 0.5) catalyst calcined at 500 °C afforded about 62% yield of cyclopentanone (entry 7, Table 3). Moreover, CuZnAl-500–0.5 catalyst could be reused for at least five times without much loss in catalytic activity. The addition of Fe considerably enhanced the performance of Cu/γ-Al_2O_3 catalyst for the vapour phase hydrogenation of furfural.[340] About 91% furfuryl alcohol yield was achieved over $CuFe/\gamma$-Al_2O_3 (Cu – 10 wt% and Fe – 10 wt%) catalyst, due to the presence of synergistic bimetallic particles and abundant oxygen vacancies in iron oxide (entry 8, Table 3).

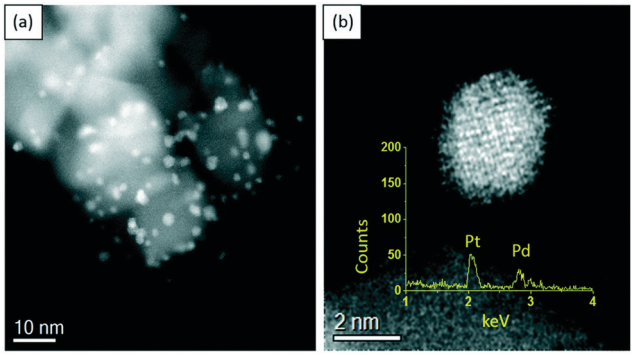

Fig. 27 Scanning transmission electron microscopic images of $Pd–Pt/TiO_2$ catalyst at different magnifications. The formation of random Pd–Pt nanoalloys is confirmed from the *Z*-contrast high-angle annular dark-field imaging and the X-ray energy-dispersive spectrum (inset image, b) taken from an individual particle. Reproduced with permission from ref. 336. Copyright (2018) Royal Society of Chemistry.

In recent work, Gupta *et al.*[341] developed a feasible catalytic process for the room-temperature total hydrogenation of furans and furan/acetone aldol adducts over Ni–Pd nano-alloy catalysts. Promising catalytic results were obtained in the presence of $Ni_{0.90}Pd_{0.10}$ nano-alloy catalyst. The possibility of scaling-up this catalytic process was also demonstrated in this work. The significance of atomic ordering on the structure–activity properties of spherically shaped Ni_xSn_y–Al_2O_3 catalysts was noticed for the vapor phase furfural hydrogenation.[342] In addition, crystal structure and metal composition of Ni_xSn_y–Al_2O_3 catalysts played a crucial role in furfural hydrogenation. Particularly, Ni_3Sn_2–Al_2O_3 catalyst showed the best performance with ~65% furfural conversion and good selectivity (57–62%) to furfuryl alcohol at optimized reaction conditions. Doping of La into the ZrO_2 led to the formation of active tetragonal phase zirconia with smaller particle size and high BET surface area.[340] Besides, improved Co–ZrO_2 interactions and abundant acid sites were found in Co/La–ZrO_2, which are crucial for the efficient adsorption of carbonyl feedstock. As a result, 95% yield of furfural alcohol was obtained *via* aqueous phase furfural hydrogenation over Co/$ZrLa_{0.2}O_x$ catalyst at 40 °C, 2 MPa H_2 in 10 h.

The hydroprocessing of 5-hydroxymethylfurfural (HMF) can give 2,5-dimethylfuran (DMF), 2,5-bis(hydroxymethyl)furan (BHF), or 2,5-dimethyltetrahydrofuran (DMTHF), depending on the catalysts and the reaction conditions used. DMF is considered as a sustainable fuel additive and BHF is a key chemical for the production of polymers and fine chemicals. Table 4 presents the notable catalytic results obtained for the liquid phase hydrogenation of HMF over porous and nanoscale catalysts. By transforming Co_3O_4 using a controlled reduction step into a bi-functional Co–CoO_x catalyst with well-balanced Co metal (hydrogenation site) and CoO_x species (acid site), a high efficiency in the liquid phase hydrogenolysis of HMF to DMF (83.3% yield) was obtained (entry 2, Table 4).[343] Cu–Zn nanoalloy with particle size <150 nm showed good catalytic activity in HMF hydrogenolysis with a 97% combined yield of DMF and DMTHF at optimized reaction conditions (entry 3, Table 4).[344] This nanoalloy catalyst also converts 10 wt% HMF in cyclopentyl methyl ether solvent to DMF (90% yield). Kong *et al.*[345] achieved improved reaction rates for HMF hydrogenolysis by adding Zn to a NiAl catalyst. The structure evolution of the NiZnAl catalyst is shown in Fig. 28A. The resulting NiZnAl mixed oxide catalyst provided a significantly enhanced DMF yield (93.6%) compared with that of NiAl catalyst (63.5%), which was attributed to electron modification and isolation of Ni atoms (entry 4, Table 4). Moreover, NiZnAl catalyst showed three times higher activity than that of NiAl catalyst in C=O/C–O hydrogenolysis over C=O/C–C hydrogenation at similar HMF conversions (Fig. 28B). Ohyama *et al.*[346] demonstrated that addition of Fe (up to 10 wt%) to Au/Al_2O_3 catalyst could improve its catalytic efficiency by 3–4 times in the hydrogenation of HMF to BHF, due to the formation of abundant surface-exposed Au nanoclusters (entry 5, Table 4). However, the activity of Au/FeO_x/Al_2O_3 catalyst was decreased drastically with further increase of Fe content (greater than 10 wt%), because of

Table 4 Liquid phase hydrogenation of 5-hydroxymethylfurfural (HMF) over porous and nanoscale catalysts

Entry	Catalyst	Reaction conditions	Product	Catalytic activity		Key factors for the catalyst activity	Ref.
				Conv. (%)	Yield (%)		
1	2 wt% Ru/NaY zeolite	Molar ratio of HMF to metal is 200, 220 °C, 15 bar H_2, THF, 1 h	DMF[a]	100	78	High dispersion of Ru NPs	136
2	Co_3O_4	0.5 g HMF, 0.1 g catalyst reduced at 400 °C, 170 °C, 12 h, 10 bar H_2, 1,4-dioxane	DMF	100	83.3	Well-balanced metal (Co) and acid (CoO_x) functionalities	343
3	Cu–Zn nanoalloy	0.5 g HMF, 0.1 g CuZn, 220 °C, 18 h, 20 bar H_2, cyclopentyl methyl ether	DMF + DMTHF[b]	100	97	Synergistic Cu–Zn interaction	344
4	NiZnAl mixed oxide	1.5 g HMF, 0.15 g catalyst, 15 bar H_2, 180 °C, 15 h, 1,4-dioxane	DMF	100	93.6	Electron modification and isolation of Ni atoms due to the formation of NiZn alloy	345
5	Au/FeO_x/Al_2O_3 (Fe = 10%)	0.1 M HMF (aq. 2 mL), 0.01 g catalyst, 80 °C, 30 bar H_2, 2 h	BHF[c]	96	96	Ample amounts of surface exposed Au nanoclusters	346
6	5 wt% Ni/WO_3	3 mmol HMF, 0.05 g catalyst, H_2O, 10 bar H_2, 180 °C, 6 h	DMF	99	95	High dispersion of Ni nanoparticles	347
7	20 wt% Ni/$LaFeO_3$ catalyst	1 mmol HMF, 0.1 g catalyst, *n*-tetradecane, 6 h, ethanol, 50 bar H_2, 230 °C	DMF	99	98.3	Ample amounts of active metal sites	348
8	Cu (5 wt%)–Ni (5 wt%)/TiO_2	0.5 g furfural loading, 0.25 g HMF loading, 0.3 g catalyst, 1,4-dioxane, 200 °C, 25 bar H_2, 8 h	DMF	—	87.5	Selective segregation of Cu and Ni sites	349

[a] DMF – 2,5-dimethylfuran. [b] DMTHF – 2,5-dimethyltetrahydrofuran. [c] BHF – 2,5-bis(hydroxymethyl)furan.

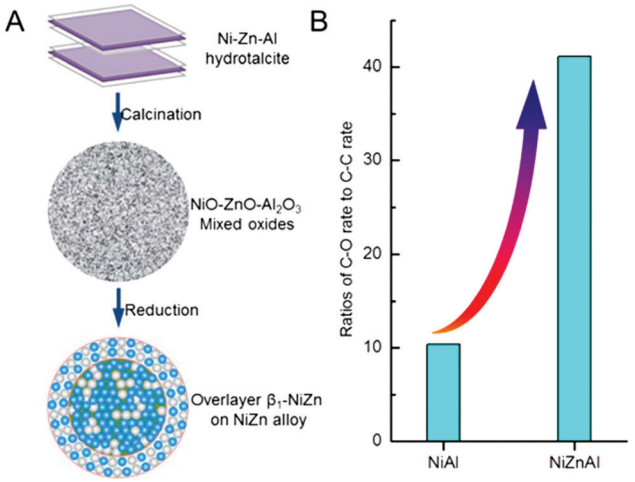

Fig. 28 (A) Structure evolution of NiZnAl catalyst and (B) comparison of reaction rates for C–O *vs.* C–C bond scission over NiAl and NiZnAl catalysts at similar HMF conversions. Reproduced with permission from ref. 345. Copyright (2017) American Chemical Society.

the formation of inactive buried structures of Au nanoclusters in FeO_x. Nickel oxide NPs supported on nanostructured tungsten oxide were demonstrated to be efficient for the aqueous phase conversion of HMF to DMF.[347] With optimized parameters, such as Ni loading, reaction temperature, and H_2 pressure, about 95% yield of DMF was achieved over 5% Ni/WO_3 catalyst, due to the presence of highly dispersed Ni nanoparticles (entry 6, Table 4). Moreover, this catalyst could be successfully reused for at least five cycles without much loss in its activity and selectivity. Ample amounts of active Ni sites in 20 wt% $Ni/LaFeO_3$ catalyst are crucial to achieve high yields of DMF (98.3%) from aqueous phase HMF hydroprocessing (entry 7, Table 4).[348] Co-hydroprocessing of HMF and furfural was successfully investigated over mono- and bi-metallic Cu–Ni/TiO_2 and Cu–Ni/Al_2O_3 catalysts.[349] The Cu–Ni/TiO_2 catalyst displayed 87.5% yield of DMF from HMF and 88.5% yield of methyl furan from furfural in a one-pot reaction (entry 8, Table 4). The selective segregation of Cu (enriched at the catalyst surface) and Ni sites (enriched at the TiO_2 interface) played a crucial role on the activity and stability of the Cu–Ni/TiO_2 catalyst.

4.5.2 Catalytic oxidation reactions. The catalytic oxidation of monosaccharides (*e.g.*, glucose) is of paramount research interest in biorefinery due to the significance of the resulting products in pharmaceutical, polymer, food, and paper industries (Fig. 29e). Based on the catalysts and the reaction conditions used, three major acid products, namely gluconic acid, glucaric acid or glucuronic acid can be obtained from glucose oxidation. Several polymer-protected Au-based bi- and tri-metallic NPs based catalysts were used for aerobic glucose oxidation.[350–353] To understand the role of redox and morphology properties of colloidal catalysts in glucose oxidation, thorough structure–activity studies have been undertaken. Results suggested that the activity of bi- or tri-metallic NPs was much higher than that of monometallic Au NPs, attributed to the presence of highly dispersed particles and abundant negatively charged top Au atoms.

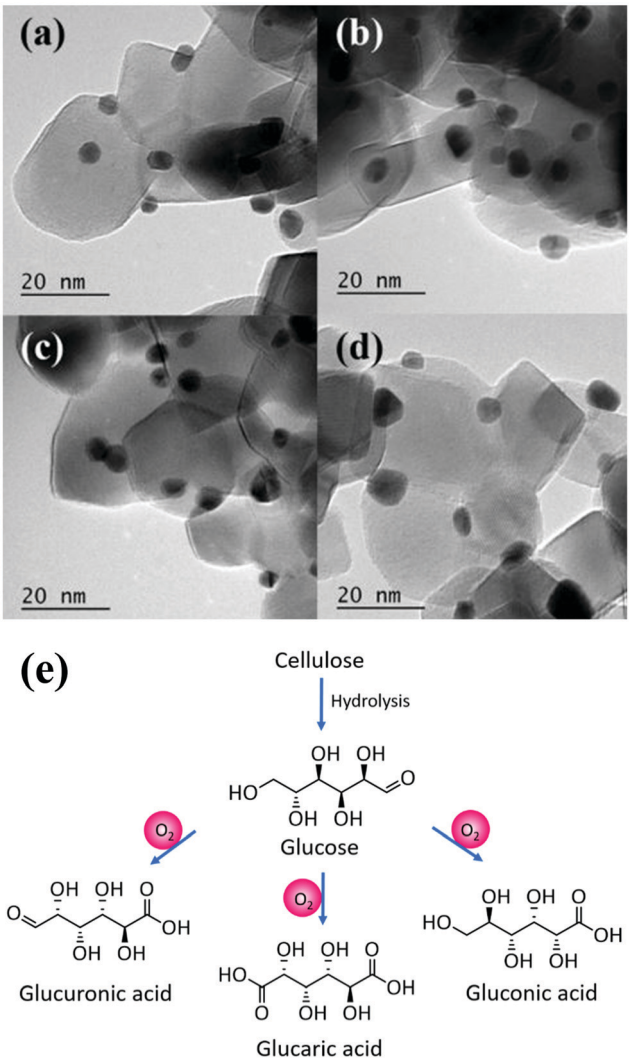

Fig. 29 Representative TEM images of 1% Au/TiO_2 catalyst synthesized by sol-immobilization method and then calcined at (a) 250 °C, (b) 350 °C, (c) 450 °C and (d) 550 °C. Reproduced with permission from ref. 355. Copyright (2015) Royal Society of Chemistry. (e) Possible products from glucose oxidation.

The Hutchings group has made significant advances towards glucose oxidation using metal oxide supported Au-based catalysts. They demonstrated that the selective, aerobic oxidation of glucose to gluconic acid can be carried out over supported Au–Pd catalysts without using a sacrificial base or pH control if a basic support (MgO) is used.[354] Effects of both the preparation method and the post-synthesis treatment on the efficiency of 1% Au/TiO_2 catalyst were also studied for base-free oxidation of glucose.[355] The catalyst prepared by sol-immobilization method and calcined at 250 °C (Fig. 29a) showed the highest activity in terms of glucose conversion and gluconic acid selectivity, due to the presence of smaller sized Au nanoparticles. The particle size of Au increases with the increase of calcination temperature (Fig. 29). Moreover, the amount of stabilizing ligand used in the sol-immobilization method is a key parameter for improving the activity of Au/TiO_2 catalysts. They also found that

bimetallic Au–Pd/TiO_2 and Au–Pt/TiO_2 catalysts display good activity in the oxidation of cellobiose (a disaccharide) to gluconic acid under base-free conditions.[356] Among Al_2O_3, CeO_2, and ZrO_2, Au NPs supported on Al_2O_3 were found to be highly active for base-free aerobic oxidation of glucose.[357] Using this catalyst, several reaction parameters, such as reaction time, temperature, and stirring rate were optimized to achieve improved gluconic acid yields. In case of non-Au based catalysts, for instance with Pt–Pd/TiO_2 catalysts, glucaric acid is mainly obtained in glucose oxidation reaction, outperforming monometallic catalysts.[358] However, Darrien *et al.*[359] reported selective formation of glucaric acid in the presence of supported Au–Pt and Au–Pd catalysts. This indicates that the presence of Pt NPs is key for the formation of glucaric acid instead of gluconic acid, a commonly observed product in Au-catalyzed glucose oxidation reactions. On the other hand, Wojcieszak *et al.*[360] noticed glucuronic acid production *via* base-free oxidation of various carbohydrates (glucose, fructose, and maltose) over Au/CeO_2 catalyst. The addition of caesium led to improved activity of the Au/CeO_2 catalyst. In contrast, base addition (K_2CO_3) to the reaction mixture resulted in the formation of various by-products, including gluconic acid.

The catalytic oxidation of biomass-derived furans, especially 5-hydroxymethylfurfural (HMF) gives a number of high-value chemicals, such as 2,5-diformylfuran (DFF), 5-hydroxymethyl-2-furancarboxylic acid (HMFCA), 5-formyl-2-furancarboxylic acid (FFCA), and 2,5-furandicarboxylic acid (FDCA), which can be used for the production of drugs, fungicides, and biopolymers (Fig. 30d).[361–363] Both noble and non-noble metal-based nanocatalysts were demonstrated to be efficient for liquid phase HMF oxidation, while product selectivity could be controlled by varying the catalyst compositions and reaction conditions, as shown in Table 5. Lei *et al.*[251] pointed out the crucial role of the particle morphology and the preferentially exposed crystal facets on the catalytic performance of Pd nanocrystals for liquid phase HMF oxidation. Pd nano-octahedra enclosed by {111} facets were more efficient than Pd nanocubes enclosed by {100} facets in HMF oxidation, outperforming a commercial Pd/C catalyst. Pt NPs, stabilized by an ionic polymer, were also catalytically active in the liquid phase, base-free oxidation of HMF under mild conditions.[362] To optimize the process towards FDCA production, thorough mechanistic and kinetic investigations were conducted. The aqueous phase oxidation of HMF to FDCA or HMFCA was carried out using TiO_2 supported mono- and bi-metallic AuPd nanoalloys.[364] An appropriate amount of polyvinylpyrrolidone was added during the catalyst synthesis to stabilize Au and Pd nanoparticles. Both Au and Pd NPs were able to convert HMF to HMFCA. Surprisingly, Pd NPs were inactive for further oxidation of HMFCA, while Au-containing catalysts showed good activity in the subsequent oxidation of HMFCA to FDCA. The combination of Au NPs and ordered mesoporous CeO_2 was found to be promising for the liquid phase HMF oxidation (entry 3, Table 5).[365] Controlled removal of silica template during CeO_2 synthesis was vital to achieve abundant structural defect sites and enhanced catalytic properties, giving high yields of FDCA (92%). Pt NPs supported on ceria solid solution ($Ce_{0.8}Bi_{0.2}O_{2-\delta}$) efficiently catalyze the liquid phase HMF-to-FDCA transformation, outperforming a Pt/CeO_2 catalyst (entry 4, Table 5).[366] About 98% yield of FDCA was achieved within 30 min at room temperature. Moreover, this catalyst was reused for five times without much loss of FDCA selectivity, attributed to superior oxygen activation ability of Bi-doped ceria support. Comparable Au particle sizes were found on both TiO_2 and CeO_2 supports.[367] However, Au/CeO_2 catalyst showed a higher activity than the Au/TiO_2 catalyst due to the existence of synergistic Au–CeO_2 interface and abundant defects in the cerium oxide lattice. Nanostructured Ru/$MnCo_2O_4$ is a selective catalyst for the liquid phase oxidation of HMF towards DFF product.[368] Both the Brønsted acidity of $MnCo_2O_4$ support and the Lewis acidity of Ru NPs were key to obtaining high yields of DFF (99%, entry 5, Table 5). The Ru/$MnCo_2O_4$ catalyst could also be reused for several consecutive cycles without much loss in catalytic activity.

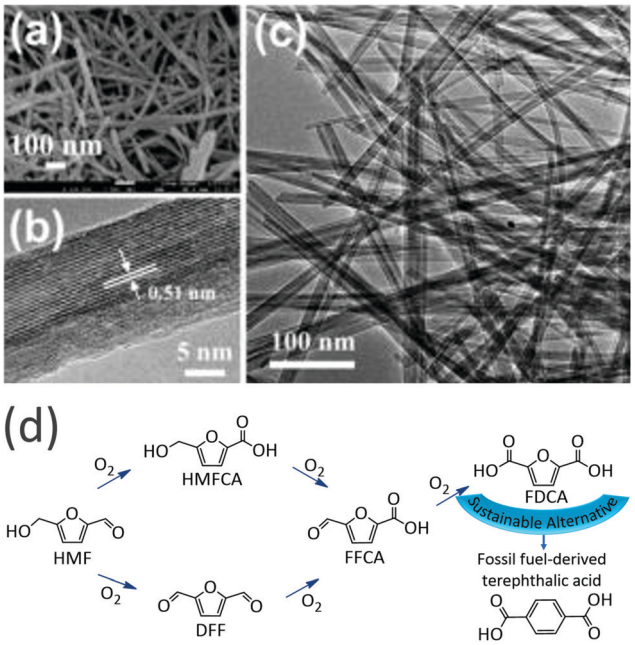

Fig. 30 (a) SEM, (b) high-resolution TEM, and (c) TEM images of Ni–MnO_x nanowires. The measured *d*-spacing of 0.51 nm corresponds to the (200) planes in the MnO_2-type unit cell. Reproduced with permission from ref. 371. Copyright (2018) Royal Society of Chemistry. (d) Possible major products from oxidation of 5-hydroxymethylfurfural (HMF): 5-hydroxymethyl-2-furancarboxylic acid (HMFCA), 2,5-diformylfuran (DFF), 5-formyl-2-furancarboxylic acid (FFCA), and 2,5-furandicarboxylic acid (FDCA).

Several non-precious metal catalysts, especially manganese-based catalysts, were demonstrated to be efficient for the liquid phase HMF oxidation. For instance, MnO_x–CeO_2 mixed oxides, prepared by a co-precipitation method, exhibited good activity for the aerobic oxidation of HMF to FDCA using $KHCO_3$ base.[369] Especially, MnO_x–CeO_2 (Mn/Ce = 6) mixed oxide afforded high yields of FDCA (84%), which was attributed to the presence of ample amounts of surface Mn^{4+} and Ce^{3+} sites (entry 6, Table 5). A series of Mn_xFe_y mixed oxides, along with pristine metal oxides were studied for HMF-to-FDCA transformation in aqueous

Table 5 Liquid phase oxidation of 5-hydroxymethylfurfural (HMF) over porous and nanoscale catalysts

Entry	Catalyst	Reaction conditions	Product	Catalytic activity		Key factors for the catalyst activity	Ref.
				Conv. (%)	Yield (%)		
1	$10V_2O_5$@Cu–MOR (125)	0.05 g HMF, 0.1 g catalyst, DMSO, 120 °C, 7 h, O_2 balloon	DFF[a]	100	91.5	Strong interaction between the framework Cu species and the guest V sites	53
2	Co–Mn/nanospherical porous silica	1 mmol HMF, 0.05 g catalyst, MeCN, 12 h, 120 °C, 7 mmol *t*-BuOOH	FDCA[b]	100	72.4	Strong metal–support interaction and high metal dispersion	197
3	1.5 wt% Au/CeO_2	HMF/metal/NaOH molar ratio 1 : 0.01 : 4, 70 °C, 10 bar O_2, 4 h	FDCA	—	92	Strong Au–ceria interaction and ceria defects	365
4	1 wt% Pt/$Ce_{0.8}Bi_{0.2}O_{2-\delta}$	Pt: HMF = 5×10^{-3} mol mol^{-1}, 4 equiv. NaOH, 10 bar O_2, 23 °C, 30 min	FDCA	100	98	High metal dispersion and oxygen vacancies of ceria	366
5	1.8% Ru/$MnCo_2O_4$	HMF/Ru ratio (50), 2 mmol HMF, toluene, 3 h, 130 °C, 10 bar O_2	DFF	99	99	Brønsted acidity of $MnCo_2O_4$ support and Lewis acidity of Ru NPs	368
6	MnO_x–CeO_2 (Mn/Ce = 6)	0.5 mmol HMF, 0.1 g catalyst, H_2O, 20 bar O_2, 110 °C, 6 h, $KHCO_3$/HMF = 2	FDCA	98	84	High concentration of surface Mn^{4+} and Ce^{3+} sites	369
7	Mn_xFe_y (Mn/Fe = 3)	HMF : NaOH molar ratio (1 : 4), 1 mmol HMF, water, 8 bar O_2, 0.05 g catalyst, 24 h, 90 °C	FDCA	93	30	Synergy of Mn^{3+} and Mn^{4+} species and hematite phase	370
8	Ni-Doped MnO_x nanowires	0.126 g HMF, 0.336 g $NaHCO_3$, 0.1 g catalyst, H_2O, 100 °C, 8 bar O_2, 28 h	FDCA	100	94	$Ni^{3+}O(-Mn^{4+})_2$ clusters	371
9	Mn–Co binary oxides (Mn/Co = 1/1)	1 mmol HMF, 0.05 g catalyst, 140 °C, 10 g ethanol, 30 bar air, 2 h	DFF	42.6	41.7	High Mn^{4+}/Mn^{3+} atomic ratio and exposed lattice oxygen species on the catalyst surface	372
10	Cu (4.8 mol%)–MnO_2	0.252 g HMF, 0.1 g catalyst, ethanol, 3 bar O_2, 140 °C, 5 h	DFF	86	82.6	Synergistic effect of Cu and MnO_2	361

[a] DFF – 2,5-diformylfuran. [b] FDCA – 2,5-furandicarboxylic acid.

medium using NaOH base.[370] Several reaction parameters, such as nature and amount of base, oxygen pressure, temperature, and catalyst composition were optimized for this reaction. The synergy of Mn^{3+} and Mn^{4+} species, coexisting with a hematite phase in Mn_xFe_y (Mn/Fe = 3) played a favorable role towards FDCA production (entry 7, Table 5). Yu *et al.*[371] indicated the beneficial effect of metal doping in MnO_x nanowires (M = Fe, Co, and Ni) for the aerobic oxidation of HMF in the presence of $NaHCO_3$ base. Results revealed that $M^{3+}O(-Mn^{4+})_2$ clusters in the doped MnO_x catalysts act as the active sites for HMF oxidation (entry 8, Table 5). Fig. 30 shows (a) SEM and (b, c) TEM images of Ni–MnO_x nanowires. The activity order of the catalysts follows as MnO_x < Fe–MnO_x < Co–MnO_x < Ni–MnO_x, in line with order of their enhanced redox property and oxygen activation capacity. The promoting role of Mn^{4+}/Mn^{3+} redox couple, along with surface exposed lattice oxygen species was distinctly observed in the Mn–Co binary oxide catalyzed HMF oxidation towards DFF product (entry 9, Table 5).[372] A nanostructured Cu–MnO_2 catalyst with rod morphology was found to be effective for the liquid phase HMF-to-DFF transformation (entry 10, Table 5).[361] A 82.6% yield of DFF was obtained over Cu (4.8 mol%)–MnO_2 catalyst, which can be reused for at least 5 times without much loss in catalytic activity. Nanocrystalline $Li_2CoMn_3O_8$ spinel, developed by a gel pyrolysis method, exhibited good catalytic performance in HMF oxidation.[373] About 80% isolated yield of FDCA was obtained in a gram scale reaction. The direct conversion of fructose to DFF *via* simultaneous dehydration and aerobic oxidation was also successfully carried out using 3D flower-like Ce–Mo micro/nano composite oxides.[374] The catalytic activities of $Ce_{10-x}Mo_xO_\delta$ oxides were highly dependent on their composition, structure, and physicochemical properties. Especially, $Ce_9Mo_1O_\delta$ displayed the highest catalytic activity with 94% and 74% yields of DFF from HMF and fructose, respectively. Ni–Pd nanoalloys played a versatile catalytic role in the aerobic oxidation of various furans, including HMF, 2-furfuraldehyde, 2-furfuryl alcohol, 5-methyl-2-furfural and 5-methyl-2-furfuryl alcohol to the corresponding carboxylic acids in water.[375] The addition of Ni not only led to enhanced catalytic activity of Pd NPs, but also to excellent stability (especially for $Ni_{0.90}Pd_{0.10}$), as the catalyst could be recycled up to ten times. This nanoalloy catalyst is also active for the direct transformation of fructose to furan carboxylic acids.

4.6 Valorization of lignin and its derived compounds

4.6.1 Lignin depolymerization. Only 2% of the lignin obtained from pulp industry is used for chemicals production.[376,377] The remaining lignin (98%) is burned to generate energy for pulp mills (low-value fuel). Therefore, developing potential catalytic strategies for lignin-to-chemicals transformation is essential for a more sustainable lignocellulose biorefinery. The Hensen group developed a thermocatalytic process for the depolymerization of lignin in supercritical ethanol using Cu–Mg–Al mixed oxides.[378] About 23 wt% yield of monomers without char formation was obtained. They found that ethanol acts as a capping agent for the efficient depolymerization of lignin to aromatics. Moreover, ethanol is a preferred solvent to obtain higher yields of monomers compared with methanol solvent.

In another work, they investigated the effect of Cu content and (Cu + Mg)/Al ratio in Cu–Mg–Al mixed oxides for the depolymerization of soda lignin in supercritical ethanol.[379] The optimized catalyst, containing 20 wt% Cu and a (Cu + Mg)/Al ratio of 4, gave about 36 wt% yield of monomers, outperforming Cu/MgO and Cu/γ-Al_2O_3 catalysts. An efficient one-pot process by combining both lignin depolymerization and hydrodeoxygenation was developed using a combination of Cu–Mg–Al mixed oxide with various Ni-based catalysts (Ni/SiO_2, Ni_2P/SiO_2, and Ni/amorphous silica–alumina).[380] Results indicated that monomer yield and product selectivity were highly dependent on the nature of Ni catalyst. Chen *et al.*[381] found that oxygen vacancies and Mo^{6+} together with Mo^{5+} species, formed during the partial pre-reduction treatment, act as the active sites for lignin depolymerization in supercritical ethanol. Consequently, compared with untreated MoO_3 catalyst, the overall yield of small molecules from depolymerization of Kraft lignin increases almost 15% in the presence of MoO_3 pre-treated at 350 °C under hydrogen atmosphere.

Catalytic hydrogenolysis is a widespread process for the efficient upgrading of lignin to high-value aromatics and fuel grade hydrocarbons. Zhang *et al.*[382] revealed that NiRu catalyst containing 85% Ni and 15% Ru is highly active in the conversion of lignin to monomeric aromatic chemicals, outperforming monometallic Ni and Ru catalysts. The high performance of $Ni_{85}Ru_{15}$ catalyst was attributed to large amounts of surface-active atoms (compared with Ni), improved H_2 and substrate activation (compared with Ni), and inhibition of benzene ring hydrogenation (compared with Ru). The catalytic hydrotreatment of Alcell lignin was performed using supported Ru (support = C, Al_2O_3, and TiO_2), Pd (support = C and Al_2O_3), and a Cu/ZrO_2 catalyst.[383] Among them, Ru/TiO_2 catalyst is highly active with a lignin oil (78 wt% on lignin intake) containing 9 wt% alkylphenols, 2.5 wt% aromatics, and 3.5 wt% catechols. Solvent has a profound effect on the hydrogenolysis of diphenyl ether and lignin carried out over a RANEY® Ni catalyst.[384] Higher yields of cyclic alcohols and cyclic alkanes were obtained in the presence of methylcyclohexane solvent, whereas 2-propanol solvent yielded mainly cyclic alcohols, cyclic ketones, and unsaturated products. The hydrogenolysis of lignin in methanol, however, produced mostly phenols. Bimetallic Pd–Ni NPs supported on ZrO_2 exhibited high selectivity in the cleavage of lignin β-O-4 linkages under hydrogen pressure conditions.[385] The catalyst could be reused efficiently for ten and five times in the hydrogenolysis of a model compound and lignin, respectively, without much loss in catalytic activity and selectivity. The direct HDO of enzymatic lignin to C6–C9 cycloalkanes was successfully performed using a Ni catalyst supported on amorphous silica–alumina.[386] About 80 wt% lignin conversion was found at 300 °C and 6 MPa H_2. The synergy of acid and metal sites could be tailored to enhance the performance of Ni catalysts. Importantly, the presence of acid sites facilitates HDO of lignin-derived phenolic fragments to selectively obtain cyclic alkanes.

4.6.2 Hydroprocessing of lignin-derived compounds. Selective hydrogenation of lignin-derived compounds is a promising route to obtain bio-based cyclohexanols, which are very important chemicals for the synthesis of polymers, spices, and medicines. The Sels group developed a reductive demethoxylation route for the liquid phase transformation of 4-*n*-propylguaiacol to cyclohexanols using 65 wt% Ni/SiO_2–Al_2O_3 catalyst.[387] Kinetics studies demonstrated two competitive reaction pathways for 4-propylcyclohexanol (PCyol) synthesis: (i) hydrogenation of 4-*n*-propylguaiacol to 4-*n*-propyl-2-methoxycyclohexanol, followed by its hydrodemethoxylation (slow step) to PCyol. (ii) Another pathway involves hydrodemethoxylation of 4-*n*-propylguaiacol to 4-*n*-propylphenol, which rapidly undergoes hydrogenation to form PCyol. At optimized reaction conditions, Ni/SiO_2–Al_2O_3 catalyst gave about 85% yield of 4-propylcyclohexanol. The beneficial effect of Ni/CeO_2 and Ni/ZrO_2 catalysts was also observed in the production of cyclohexanols from lignin-derived phenols.[388] In addition, the Ni/CeO_2 catalyst could depolymerize a real 4-*n*-propylguaiacol-rich feedstock (obtained *via* hydroprocessing of softwood) into 4-*n*-propylcyclohexanol (80% yield), which could be dehydrogenated into the corresponding ketone using a Cu/ZrO_2 catalyst. The 3 wt% Pd/γ-Al_2O_3 catalyst, prepared by a wet-impregnation method, plays a remarkable catalytic role in the liquid phase hydrogenation of 4-ethylphenol to 4-ethylcyclohexanol (98.9% yield).[389] The Pd/γ-Al_2O_3 catalyst was also able to catalyze the hydrogenation of a monophenol mixture, which was directly derived from raw biomass, to cyclohexanols, and the depolymerization of lignin oligomers under mild reaction conditions.

Interestingly, bulk MoO_3 phase is also capable of catalyzing the vapor phase hydrodeoxygenation (HDO) of various lignin-derived oxygenates (phenol, *m*-cresol, anisole, guaiacol, and diphenyl ether) to benzene or toluene under H_2 pressure conditions.[390] MoO_3 catalyst preferentially cleaved phenolic Ph–OMe bonds over the weaker aliphatic PhO–Me bonds during the HDO of lignin-derived compounds. Partial surface carburization of the catalyst, occurred during the reaction, played a crucial role in stabilizing the Mo^{5+} species on the MoO_3 surface as well as in controlling the over-reduction of MoO_3 to form an inactive MoO_2 phase. In another work, MoO_3/ZrO_2 catalysts with varied MoO_3 loadings (1 to 36 wt%) were tested for the vapor phase HDO of anisole at H_2 pressures of $\leq$1 bar.[391] The monolayer coverage of MoO_3 on ZrO_2 surface (optimized for 15 wt% MoO_3) was crucial to obtain improved specific reaction rates in anisole HDO reaction. This is because the reduction of MoO_3 crystallites to less reactive MoO_2 is possible once the monolayer coverage is exceeded. Zhang *et al.*[392] pointed out that oxygen vacancies present in MoO_3 (Mo^{5+}) exhibit a favourable effect in the selective cleavage of Ph–OH bonds during the liquid phase HDO of phenol to produce benzene (97% yield, entry 7, Table 2). The conversion of guaiacol to substituted alkylphenols was performed in supercritical ethanol without using additional hydrogen source.[393] A total selectivity of 86% to alkylphenols at 99% guaiacol conversion was obtained at optimized reaction conditions. Characterization of used catalyst revealed that oxycarbohydride phase ($MoO_xC_yH_z$) with Mo^{5+}, formed under supercritical alcohol conditions, is the primary reason for improved conversion rates and high product selectivity.

Recently, much attention has been devoted towards understanding the role of metal oxide supports on the performance

of metal/metal oxide catalysts for hydroprocessing of lignin-derived compounds. For instance, the catalytic efficiency of MoO_x in liquid phase HDO of *m*-cresol to toluene (80–85%) was strongly dependent on the support nature (Al_2O_3, SBA-15, and SiO_2).[394] The activity order of investigated catalysts follows as MoO_x/Al_2O_3 > MoO_x/SBA-15 > MoO_x/SiO_2, which is in line with the reducibility of Mo species on the respective supports (entry 8, Table 2). Owing to high metal dispersion and strong metal–support interaction, the 10 wt% Co catalyst supported on TiO_2 (compared to CeO_2, ZrO_2, Al_2O_3, and SiO_2) showed the best HDO activity with >99.9% yield of propylcyclohexanols from lignin-derived phenols (entry 9, Table 2).[395] Irrespective of the metal oxide support, all the catalysts selectively cleaved the C_{aryl}–OCH_3 bond in lignin-derived compounds, followed by hydrogenation of the aromatic ring when the –OCH_3 group was present at the *ortho*-position. Interestingly, except for anatase TiO_2-40 nm, the guaiacol conversion and the product selectivity did not significantly differ between the supported Au catalysts and the supports alone (anatase TiO_2 in 45 μm, rutile TiO_2, ZrO_2, Al_2O_3, SiO_2, and activated carbon).[396] This indicates that Au NPs are barely active for the HDO of lignin-derived compounds. On the other hand, supported Pt based catalysts (TiO_2, SiO_2, Al_2O_3, and Nb_2O_5–Al_2O_3) displayed good activity in the vapour-phase HDO of diphenyl ether.[397] The 0.40 wt% Pt/20Nb–Al_2O_3 catalyst afforded 100% diphenyl ether conversion and 99.2% cyclohexane selectivity due to the presence of abundant water-tolerant Lewis acid sites (entry 10, Table 2). Bimetallic NiCo/γ-Al_2O_3 catalysts were found to be promising in the aqueous phase HDO of guaiacol compared to supported monometallic Ni and Co catalysts.[398] About 96% guaiacol conversion and 68% cyclohexanol selectivity were obtained over NiCo/γ-Al_2O_3 catalyst (Ni : Co = 1 : 1 with 20% total loading), which was ascribed to improved acidity and synergistic metal–support interaction (entry 11, Table 2). Liu *et al.*[399] used density functional theory calculations to evaluate reaction mechanisms and product selectivity in HDO of guaiacol over Fe-alloyed (Ni, Pt) catalysts. Results revealed that catechol was the major product of guaiacol HDO reaction over both Fe-alloyed catalysts and was formed *via* dehydrogenation of methoxy (OCH_3), followed by O–CH_2 bond scission.

The Song group investigated the role of TiO_2 addition on the structure–activity properties of Pd/SiO_2 catalysts for the vapor phase HDO of guaiacol.[400] Results demonstrated that TiO_2 is essential to stabilize Pd particles as well as to activate the C–O bond in guaiacol, leading to higher conversion rates *via* enhanced deoxygenation activity. Consequently, $Ti_{2.0}Pd/SiO_2$ catalyst exhibited about 80% cyclohexane selectivity at full conversion of guaiacol (entry 12, Table 2). They also pointed out the crucial effect of TiO_2 phase (anatase, rutile, and their mix, P25) on the performance of Pd catalysts for the vapor phase HDO of guaiacol.[401] Interestingly, 5 wt% Pd catalyst supported on anatase TiO_2 showed higher efficiency in guaiacol HDO to obtain cyclohexane due to the existence of partially reduced titanium species on the surface of anatase TiO_2 that can efficiently cleave the C–O bond in guaiacol. The activity of 5 wt% Ru/TiO_2 catalyst for the vapor phase HDO of guaiacol could be considerably promoted by ZrO_2 addition.[402] The authors propose that ZrO_2 can hinder the migration of Ti^{3+} species on the surface of Ru particles and thus, more Ru active sites are available for the HDO of guaiacol to obtain benzene. Xu *et al.*[403] also observed the favourable role of ZrO_2 addition in improving the efficiency of 5 wt% Ru/$La(OH)_3$ catalyst for the aqueous phase HDO of lignin-derived phenols. Zr and La can interact with each other to form a stable mixed (hydr)oxide, which effectively stabilizes active Ru particles. At optimized reaction conditions, 91.6% and 86.9% yields of cyclohexanol and alkyl cyclohexanols were obtained from guaiacol and alkyl phenols, respectively (entry 13, Table 2). Han *et al.*[404] demonstrated the influence of shape-controlled TiO_2 spheres in guaiacol hydrogenation. Promising results were obtained in terms of guaiacol conversion (100%) and cyclohexanol yield (84.2%) over Ru supported on mesoporous TiO_2 hollow spheres embedded within SiO_2 NPs. This remarkable catalytic activity is attributed to the unique spherical structure and improved acid properties. Thorough experimental and theoretical studies were performed to understand hydrogen-efficient HDO mechanism of phenol over Ru/TiO_2 catalyst.[405] Results indicated that the amphoteric nature of TiO_2 facilitates the H_2 heterolysis to generate an active site water molecule, promoting the direct substitution of phenolic OH with H to form benzene. Ambrusa *et al.*[406] found that high dispersion of NiCu particles on TiO_2 is the primary reason for achieving improved results in the liquid phase HDO of dibenzofuran to bicyclic hydrocarbons. Reaction temperature was also found to play a crucial role in tailoring product selectivity.

4.7 Valorization of lipids

The catalytic valorization of lipids (oils & fats) and their model compounds to produce biodiesel is discussed in this section.[407,408] Several Mo- and W-based mixed oxides were found to show good catalytic activities for biodiesel synthesis *via* liquid phase transesterification of triglycerides (oils) or esterification of fatty acids with simple alcohols (mainly methanol). Xie *et al.*[409] for instance, indicated that 30% WO_3/SnO_2 can be used as solid acid catalyst for the transesterification of soybean oil (79% conversion) with methanol to produce biodiesel. This catalyst can be reused up to four cycles without much loss in catalytic activity. However, there was a drastic decrease in biodiesel yield (57.8%) after 5th recycle, due to the blockage of catalyst active sites by adsorbed intermediates/byproducts. In another work, a mixed oxide Al_2O_3–ZrO_2 was used as support for WO_x catalyst, which displayed about 90% conversion of soybean oil at 250 °C that could be maintained up to 100 h of time on stream.[410] In contrast, very low oil conversions were obtained in the presence of sulfated tin oxide (SO_4^{2-}/SnO_2) and sulfated zirconia (SO_4^{2-}/ZrO_2) catalysts. According to López *et al.*,[411] tungstated zirconia was the most suitable catalyst for both the transesterification of triglycerides and the esterification of carboxylic acids to produce biodiesel. This catalyst was more active than the titania–zirconia for esterification and its activity could be easily regenerated than the sulfated zirconia by simply re-calcining the catalyst in air. Although sulfated zirconia is catalytically active for biodiesel

synthesis, a huge loss of sulfur was observed during reaction. Waste cooking oil, containing high amounts of free fatty acids, was used for the synthesis of biodiesel over MoO_3/ZrO_2, WO_3/ZrO_2, WO_3/ZrO_2–Al_2O_3, and MoO_3/SiO_2 catalysts.[412] Among them, MoO_3/SiO_2 was found to be the most promising catalyst, achieving 79% biodiesel yield at optimized reaction conditions. Komintarachat *et al.*[413] studied the role of different supports, namely Al_2O_3, SiO_2, SnO_2, and ZnO on the performance of WO_x catalysts for the transesterification of waste cooking oil (15% free fatty acid content). The activity of supported WO_x catalysts, based on biodiesel yields, was in the following order: Al_2O_3 > SiO_2 > SnO_2 > ZnO. The high activity of WO_x/Al_2O_3 catalyst can be explained by larger BET surface area (260 $m^2\ g^{-1}$) and greater pore volume (0.95 $cm^3\ g^{-1}$) of Al_2O_3 support, since bulky triglyceride molecules can efficiently adsorb/desorb through larger pores. Guldhe *et al.*[414] pointed out the potential catalytic role of WO_3/ZrO_2 solid acid in the conversion of *S. obliquus* lipids, giving 94.6% biodiesel yield, which is comparable to that obtained in the presence of a liquid acid catalyst (*e.g.*, H_2SO_4) and higher than that of an enzyme catalyst (immobilized *Pseudomonas fluorescence lipase*). The properties of biodiesel obtained in this work can comply with the specifications set by American and European biodiesel standards. Compared to WO_3 based catalyst, MoO_3/ZrO_2–TiO_2 is effective for the esterification of oleic acid with methanol to biodiesel.[415] This is due to well-balanced acid and specific surface area properties in MoO_3/ZrO_2–TiO_2 catalyst. For the same reaction, a pellet-type WO_3/ZrO_2 catalyst provided a 70% steady state conversion of oleic acid for 140 h.[416] The oxidation state of tungsten species played a crucial role in the activity of WO_3/ZrO_2 catalyst for biodiesel synthesis. dos Santos *et al.*[417] investigated the effect of tungsten loadings in WO_x/ZrO_2 catalyst for the esterification of palmitic acid. Polymeric tungsten species dispersed on tetragonal ZrO_2 can provide abundant Brønsted acidic sites, which are key active sites for palmitic acid esterification. Notably, the 15 wt% WO_x/ZrO_2 catalyst exhibited a high resistant to leaching, and hence excellent reusability for several recycles without much loss in catalytic activity.

Various $CaTiO_3$, $CaMnO_3$, $CaZrO_3$ and $Ca_2Fe_2O_5$ perovskites, prepared by milling and then calcination, were tested for biodiesel synthesis *via* methanolysis of sunflower oil.[418] Best catalytic results (biodiesel production) were obtained over two-phase CaO/$CaTiO_3$ or CaO/$Ca_2Fe_2O_5$ catalysts at 165 °C, which was attributed to the presence of isolated CaO active phase. As a result, a number of CaO-based oxides were developed for biodiesel synthesis.[419–422] Sr–Zr mixed oxides were also active in one-pot esterification and transesterification of waste cooking oil with ethanol.[423] Owing to well-balanced acid–base properties, mixed oxide with a 2 : 1 atomic ratio of Sr–Zr, followed by calcination at 650 °C, displayed the highest catalytic performance towards biodiesel production. In another work, Mg was added to SrO to improve its catalytic activity for biodiesel production.[424] Super strong basic sites in Sr–Mg mixed oxides were formed *via* a partial solid-state reaction induced by thermal treatment at 600 °C. These novel basic sites together with the original basic sites from SrO played a beneficial role in transesterification reaction, achieving about 96% biodiesel yield at optimized reaction conditions.

4.8 Glycerol upgrading

Nanostructured metal/metal oxide based catalysts were found to be highly effective for the conversion of glycerol to a number of valuable chemicals, such as acetins, acetals, glyceric acids, glyceraldehyde, lactic acid, 1,2-propanediol, 1,3-propanediol, dihydroxyacetone, acrylic acid, acrylonitrile, acetol, allyl alcohol, 1-propanol, propylene, *etc.*[425,426] Glycerol acetins, produced *via* acetylation of glycerol with acetic acid or acetic anhydride, have found useful applications as antiknock and fuel additives. Various mixed oxides, namely TiO_2–ZrO_2, WO_x/TiO_2–ZrO_2 and MoO_x/TiO_2–ZrO_2, along with ZrO_2 were examined for the acetylation of glycerol with acetic acid in liquid phase.[427] Several reaction parameters, such as catalyst loading, temperature, time, and molar ratio of acetic acid to glycerol were optimized. Owing to rational textural and acid properties, MoO_x/TiO_2–ZrO_2 catalyst afforded full conversion (100%) of glycerol with a high selectivity to triacetin. Glycerol acetals and ketals, important chemicals as fuel-additives, bases, scents, and flavors, are synthesized *via* liquid phase condensation of glycerol with aldehydes and ketones over ZrO_2[428] and SnO_2 based solid acid catalysts.[429] High concentration of acid and redox sites is crucial for this reaction, and hence improved product yields were obtained with Mo^{6+} doped SnO_2 solid acid.[429] The catalytic significance of various mixed oxides, such as CeO_2–ZrO_2,[430] promoted TiO_2–ZrO_2,[431] and SnO_2 based catalysts[432,433] has been also markedly noted in glycerol acetylation and acetalization reactions.

Glycerol oxidation is a sequential reaction that follows multiple pathways and gives various high-value chemicals (Fig. 31).[425,434] The major challenges associated with the catalytic oxidation of glycerol are (i) catalyst stability, (ii) product selectivity, and (iii) using alkaline-free conditions.[426] A series of nanostructured CuCo catalysts, prepared by a co-precipitation method, were studied for the aqueous phase oxidation of glycerol

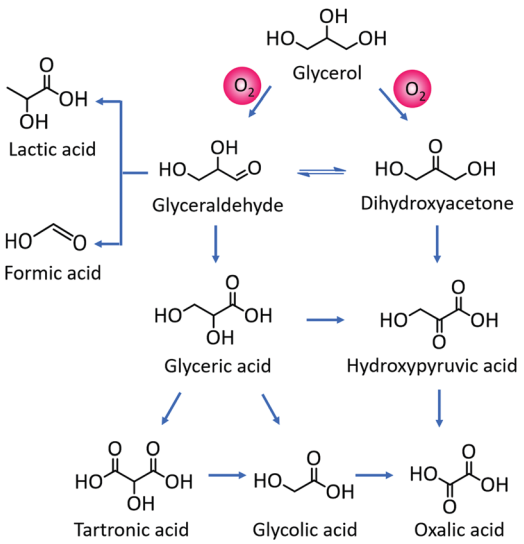

Fig. 31 Possible major products from glycerol oxidation reaction.

under basic conditions.[435] Both the Cu/Co ratio and the post-treatment are the foremost factors to achieve improved product yields (glyceric, glycolic, and formic acid) in glycerol oxidation over nanoscale CuCo catalysts. The catalytic efficiency of isolated Au clusters (from 1 to 5 atoms) dispersed on TiO_2 in the oxidation of glycerol using a NaOH solution can be enhanced by tuning the synthesis conditions of Au NPs, such as temperature and solvent.[436] The synthesis of Au NPs in H_2O at 1 °C resulted in a higher activity in glycerol oxidation compared with other Au/TiO_2 catalysts reported in the literature. Au loading and Au particle size are also important for the Au/TiO_2 catalyzed glycerol oxidation reaction.[437] Results suggested that low Au loadings favor the formation of smaller Au NPs with narrow size distribution, leading to improved catalytic efficiency as smaller Au particles act as much stronger adsorption sites for glycerol. Ag NPs supported on Al_2O_3 were found to be effective for the liquid phase oxidation of glycerol to glycolic acid.[438] About 85% glycerol conversion and 57% selectivity to glycolic acid were achieved over a 3.6 wt% Ag loaded catalyst. Díaz *et al.*[439] reported kinetic models to evaluate the deactivation of Al_2O_3 supported Au, Pt and Ag NPs for glycerol oxidation. Notably, Pt/Al_2O_3 and Au/Al_2O_3 favored glyceric acid production, while glycolic acid was the major product over Ag/Al_2O_3 catalyst. Among the catalysts tested, Pt/Al_2O_3 was the least stable catalyst. The catalytic efficiency of nanoscale Ag/CeO_2 catalyst is considerably improved for glycerol oxidation after the addition of Au, Pd or Pt.[440] Mainly, the 5% Pt containing Ag95–Pt5/CeO_2 catalyst showed the best performance with 54% glycerol conversion and 51% glycolic acid selectivity. Interestingly, further increase of the Pt amount (up to 50%) led to a noticeable shift in product selectivity from glycolic acid to glyceric acid. A synergistic effect of Au–Pd nano-alloys supported on ceria–zirconia was observed for the glycerol oxidation and the activity of the catalysts increased with the increase of Au : Pd ratio.[441] The oxidation pretreatment of 2.2AuPd/$Ce_{0.62}Zr_{0.38}O_2$ catalyst at 700 °C led to an improved performance for the oxidation of glycerol, attributed to the homogenous dispersion of Au–Pd nano-alloys. Recent results indicated that the introduction of Cu and Ag modifies the Au electronic state in Au/ZnO catalyst, enriched by strong metal–metal interactions.[442] The AuCu/ZnO catalyst having metallic Au with the lowest negative charge, was found to be the most active catalyst for glycerol oxidation using molecular oxygen. The utilization of supported bimetallic NPs based on Au, Pd, and Pt resulted in enhanced catalytic activities in glycerol oxidation due to the synergistic metal–metal and metal–support interactions.[426] The use of basic metal oxides (*e.g.*, MgO) as supports for Au-based catalysts seemed to be promising route for base-free oxidation of glycerol.

Lactic acid, a platform chemical for the production of biodegradable fibers, polylactic acid esters, and other bio-based chemicals, is commercially produced (~95% of world production) *via* enzyme-catalyzed fermentation of carbohydrates (glucose and sucrose).[443,444] However, this process is slow and involves high cost of enzymes, large amounts of salt waste generation and tedious workup separation procedures. The direct transformation of glycerol to lactic acid *via* glycerol oxidation to glyceraldehyde has been investigated as an alternative to the fermentation route. Three types of Cu based catalysts, such as Cu/SiO_2, CuO/Al_2O_3, and bulk Cu_2O with a base promoter (NaOH) were studied for the synthesis of lactic acid from glycerol in liquid phase without using reducing and oxidizing agents.[443] Both CuO/Al_2O_3 and bulk Cu_2O catalysts showed higher glycerol conversions (~95%) compared to that of Cu/SiO_2 catalyst (75%) at nearly identical lactic acid selectivity (75–80%). CuO/ZrO_2 catalyst was also found to be effective for direct conversion of glycerol to lactic acid in aqueous solution.[444] Cu loading (~30%) was optimized to attain abundant metallic Cu species in CuO/ZrO_2 catalyst, which could promote both dehydrogenation and hydrogenolysis of glycerol towards lactic acid production (94.6% yield). Palacio *et al.*[445] demonstrated that the preparation method of nanostructured Co_3O_4/CeO_2 catalyst could strongly affect both glycerol conversion and lactic acid selectivity. Compared to deposition–precipitation synthesized catalyst, improved results *i.e.* 79.8% lactic acid selectivity and 85.7% glycerol conversion were obtained over the impregnated Co_3O_4/CeO_2 catalyst, which contains uniformly dispersed crystalline Co_3O_4 NPs in synergistic interaction with the CeO_2 support. Cyclic dimer of lactic acid (*i.e.* lactide) is a key intermediate formed during the production of polylactic acid.[446] Lactide is currently produced by a two-step procedure, involving synthesis of a pre-polymer *via* water removal from concentrated lactic acid solution, followed by thermal depolymerization of pre-polymer chain through intramolecular esterification so called ''backbiting''. Alternatively, the Sels group developed a novel, efficient one-pot method for the synthesis of lactide from methyl lactate using TiO_2/SiO_2 catalysts.[447] Lactide selectivity was as high as 90% at 42% methyl lactate conversion over 5% TiO_2/SiO_2 catalyst at 220 °C, while bulk TiO_2 (both rutile and anatase) was almost inactive for lactide formation. A strong correlation between specific catalytic activity of TiO_2 and its electronic/geometric features was observed. A higher number of weak Ti–O–Si bonds and low coordination number of Ti sites in TiO_2/SiO_2 composite are essential for improved methyl lactate-to-lactide transformation.

The gas phase dehydration of glycerol to acrolein (an important chemical for the chemical and agricultural industries) was studied using W–Nb–O complex mixed oxides, along with WO_3/Nb_2O_5 and WO_3/ZrO_2 solid acids.[448] The structure of W–Nb–O strongly affects the product distribution in glycerol dehydration. Both W–Nb–O and WO_3/ZrO_2 catalysts displayed a lower deactivation rate than a zeolite catalyst. Calcination temperature (varied in the range of 110–700 °C) played a central role in tuning the structure–activity properties of Ta_2O_5 for the gas phase dehydration of glycerol.[449] Particularly, Ta_2O_5 catalyst calcined at 350 °C exhibited the best performance in terms of glycerol consumption rate and acrolein selectivity, which was attributed to the hydrated amorphous state and the strong acidic properties. Foo *et al.*[450] investigated the role of Lewis and Brønsted acidic sites in the dehydration of glycerol over niobia and Na^+-exchanged niobia catalysts. Results revealed that Lewis acidic sites favored the formation of hydroxyacetone, while acrolein selectivity is improved in the presence of more Brønsted acid sites than

the Lewis acid sites. Effects of coke formation on the product distribution was examined in the gas phase dehydration of glycerol over WO_3/TiO_2 catalyst.[451] Surprisingly, selectivity to acrolein increased as coke formed on the catalyst during the 14 h reaction time. The coke was suggested to cover specific active sites (weak and medium acidic sites), responsible for undesirable side reactions, resulting in improved glycerol-to-acrolein conversion, which is typically catalyzed by strong acidic sites.

Acrylic acid and its esters are very important chemicals for the manufacture of polymers, plastics, and synthetic rubbers.[452] The Ueda group developed several metal oxide-based catalysts for the conversion of glycerol (or acrolein) to acrylic acid.[453–456] In 2017, Sun *et al.*[98] provided a critical review on glycerol-to-acrylic acid conversion using a variety of solid catalysts, including metal oxides.

Owing to synergistic redox properties, metal oxide supported transition metals (*e.g.*, Ru, Rh, Pt, Pd, Cu, Co, and Ni) are attractive catalysts for the hydrogenolysis of glycerol to obtain 1,2-propanediol (1,2-PDO) or 1,3-propanediol (1,3-PDO). Both 1,2-PDO and 1,3-PDO have widespread applications in pharmaceutical, antifreeze additives, cosmetics, and polymer industries.[457] Table 6 summarizes the most important catalytic results obtained in glycerol hydrogenolysis over porous and nanoscale catalysts. For instance, the aqueous phase hydrogenolysis of glycerol to 1,3-PDO was studied over a Pt/WO_x catalyst.[458] Owing to larger specific surface area and abundant oxygen vacancies, the mesoporous WO_x support improved the dispersion of isolated Pt atoms. A very high space–time yield (3.78 gg Pt^{-1} h^{-1}) towards 1,3-PDO was obtained with this catalyst, which was attributed to synergistic Pt–WO_x interface and specificity of bond formation between glycerol and WO_x. Addition of Au to Pt/WO_x catalyst led to improved glycerol conversion (81.4%) with a 51.6% selectivity to 1,3-PDO.[459] The *in situ* generated Brønsted acidic sites and spatially separated pairs of H^+ and H^- function were the key factors for the efficient conversion of glycerol to 1,3-PDO (entry 3, Table 6). The promoting effect of non-noble Ni addition on the performance of $Ir/\gamma\text{-}Al_2O_3$ catalyst was also noticed for glycerol hydrogenolysis.[460] Results indicated that the calcination step was crucial to obtain strong Ir–Ni interaction and consequently a significant increase in glycerol conversion and 1,2-PDO selectivity. Sun *et al.*[461] observed a considerable leaching of Zn from PdZn alloys, resulting in rapid catalyst deactivation in the liquid phase hydrogenolysis of glycerol. Surprisingly, the physical mixture of Pd/m-ZrO_2 and ZnO inhibited the catalyst deactivation in glycerol hydrogenolysis, due to the *in situ* formation of stabilized PdZn alloy layers on Pd surfaces.

Multicomponent Cu–ZrO_2–MgO catalysts, prepared by a co-precipitation method with various Cu and ZrO_2 loadings, were found to be effective for the liquid phase hydrogenolysis of glycerol.[462] The efficacy of the catalysts is highly dependent on the concentration of available Cu sites and moderate catalyst basicity. About 97% selectivity to 1,2-PDO and 62% glycerol conversion were obtained over 20%Cu–10%ZrO_2–MgO catalyst (entry 4, Table 6). Cai *et al.*[463] examined both bare Cu–Al_2O_3 and ZrO_2-promoted Cu–Al_2O_3 catalysts for glycerol-to-1,2-PDO transformation in vapour phase. Compared to Cu–Al_2O_3 catalyst,

Table 6 Hydrogenolysis of glycerol over porous and nanoscale catalysts

Entry	Catalyst	Reaction conditions	Catalytic activity			Key factors for the catalyst activity	Ref.
			Product	Conv. (%)	Yield (%)		
1	2%Pt–5%Cu/H-mordenite	Vapor phase, 210 °C, H_2 flow rate of 80 mL min^{-1}, glycerol concentration of 10 wt%	1,3-PDO[a]	90	52.6	Synergistic bimetallic phase-support interaction, Brønsted acidity of H-mordenite and its multiple pore system	143
2	5 wt% Cu/SBA-15	Vapor phase, 0.4 g catalyst, 220 °C, H_2 flow rate of 30 mL min^{-1}, WHSV of 1.03 h^{-1}, 10 h	1,2-PDO[b]	90	75.6	Homogeneous Cu dispersion and catalyst acidity	216
3	Au–Pt/WO_x (2 wt% Pt and 0.1 wt% Au)	Liquid phase, 0.6 g catalyst, aq. solution of glycerol (12 g, 5 wt%), 140 °C, 10 bar H_2, 12 h	1,3-PDO	81.4	42	*In situ* generated Brønsted acid sites and spatially separated pairs of H^+ and H^- function	459
4	20%Cu–10%ZrO_2–MgO	Liquid phase, 0.6 g catalyst, 20 wt% of glycerol, 40 bar H_2, 8 h, 180 °C	1,2-PDO	62	60	High concentration of available Cu sites and moderate basicity of the catalyst	462
5	Cu–Al_2O_3–ZrO_2 (20 wt% Zr)	Vapor phase, 20 wt% glycerol ethanol solution, 27.8 mL h^{-1} liquid flow rate, 100 mL min^{-1} H_2 flow rate, H_2 : glycerol = 95 : 1 (mole ratio), 4 g catalyst, WHSV = 1.21 h^{-1} 230 °C, 35 bar operating pressure, data acquisition after steady operation for 3 h	1,2-PDO	97	92.4	High dispersion of Cu particles and synergistic Cu–Zr interaction	463
6	CuO–MgO–CeO_2 (Cu/Ce/Mg atomic ratio = 1/3/5)	Liquid phase, 1 g catalyst, 50 g of 20 wt% aqueous glycerol solution, 200 °C, 60 bar H_2 pressure, 10 h	1,2-PDO	51.8	50.4	High surface area, ample amounts of acid sites, abundant oxygen vacancies, and improved reducibility	457
7	ZnPd/ZnO–3Al reduced at 350 °C	Liquid phase, 0.1 g catalyst, 230 °C, 30 bar H_2, 5 mL of 20 wt% glycerol aqueous solution, 6 h	1,2-PDO	70	64.8	Smaller sized ZnPd particles, improved reduction of ZnO, and abundant oxygen vacancies	468

[a] 1,3-PDO – 1,3-propanediol. [b] 1,2-PDO – 1,2-propanediol.

ZrO_2-promoted Cu–Al_2O_3 catalyst showed durable activity for glycerol hydrogenolysis, which was attributed to high dispersion of Cu particles and synergistic Cu–Zr interaction (entry 5, Table 6). Mallesham *et al.*[457] demonstrated the beneficial effect of Ce on the catalytic performance of Cu–Mg mixed oxide for the liquid phase hydrogenolysis of glycerol to 1,2-PDO (entry 6, Table 6). Results revealed that the addition of Ce to Cu–Mg–O leads to improved specific surface area, enriched redox properties, and ample amounts of acid–base sites, and consequently high yields of 1,2-PDO over CuO–MgO–CeO_2 catalyst (Cu/Ce/Mg atomic ratio = 1/3/5). Leaching of Zn species and Cu sintering were the primary reasons for the deactivation of bimetallic CuZn catalysts in glycerol hydrogenolysis.[464] The significance of support nature and metal addition in improving catalyst stability and product selectivity in glycerol hydrogenolysis is discussed in recent articles.[465–469]

4.9 Terpenes upgrading

Terpenes are volatile unsaturated hydrocarbons found in many plants, such as pine, citrus, conifers, peppermint, spearmint, caraway, and dill. Some important examples of monoterpenes (*e.g.*, α-pinene, myrtenol, carvone, *p*-cymene, and citral) are shown in Fig. 32. The catalytic oxidation of terpenes gives a number of value-added terpenoid products, which can be used as flavors, fragrances, spices and cosmetics. Costa *et al.*[470] used ammonia hydroxide to stabilize Au hydroxides on MgO support, enabling the formation of highly dispersed Au NPs, which are indispensable to achieve higher yields of carbonylic monoterpenoids from the aerobic oxidation of bio-derived monoterpenic alcohols. Addition of Cu, Co or Ru has a considerable effect on the efficacy of nanoscale Au/TiO_2 catalyst for α-pinene oxidation.[471] The bimetallic AuCu/TiO_2 catalyst displayed the best performance in terms of α-pinene conversion and verbenone product selectivity due to synergistic metal–metal and metal–support interactions. Mn–Fe–O mixed oxide is a highly selective catalyst in the aerobic oxidation of *p*-cymene towards terephthalic acid, an important chemical for the production of poly(ethylene terephthalate) (PET).[472] *p*-Cymene can be produced from terpenes or eucalyptol. About 51% yield of terephthalic acid was obtained over Mn–Fe–O catalyst with molecular oxygen as the oxidant, outperforming Mn_2O_3, Fe_2O_3, $CoFe_2O_4$, $NiFe_2O_4$, and V/Al_2O_3 catalysts.

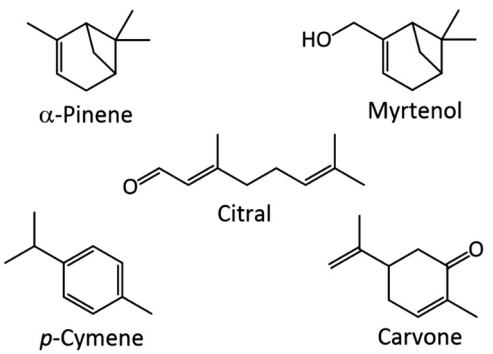

Fig. 32 Some important examples of monoterpenes.

The selective hydrogenation of terpenes is an important process for the production of valuable fine chemicals.[473] The direct synthesis of naturanol from α-pinene oxide, involving isomerization of α-pinene oxide to campholenic aldehyde in liquid phase, followed by its hydrogenation to naturanol, was performed using bimetallic Pt–Sn/SiO_2 catalysts.[474] Oxidized Sn species acted as active sites for isomerization step, while Sn/Pt ratio affected both the hydrogenation of α-pinene oxide and the naturanol selectivity. The conversion of carvone and selectivity to carvomenthone achieved in Al_2O_3 supported metal-catalyzed carvone hydrogenation reaction followed the order: Pd > Rh > Ru and Rh > Pd > Ru, respectively.[475] Interestingly, supercritical CO_2 as the reaction medium showed a promoting effect in carvone hydrogenation. Ekou *et al.*[476] indicated that catalyst preparation method and activation pre-treatment of Rh/TiO_2 and Pt/TiO_2 catalysts were the foremost factors for selective hydrogenation of citral into unsaturated alcohols. Results suggested that $TiO_{(2-x)}$ species play a vital role in the activation of C=O groups of citral to obtain desirable products. A comprehensive review was published on the selective hydrogenation of citral over metal-based solid catalysts.[473] In recent years, several nanoscale bimetallic[477] and supported metal nanocatalysts[478,479] were also investigated for citral hydrogenation.

The Simakova group developed a potential catalytic route for the direct amination of myrtenol with aniline using nanoscale Au catalysts supported on different metal oxides (*e.g.*, MgO, ZrO_2, CeO_2, Al_2O_3, and La_2O_3).[480] The resulting terpene amines are very useful for the production of drugs (for neurological diseases). A correlation between the acid–base properties of support and the performance of Au catalysts was established in this study. Au/ZrO_2 catalyst afforded about 52% selectivity to secondary amines of myrtenol at nearly complete conversion. They also examined the role of hydrogen addition and the reaction temperature towards product selectivity in myrtenol amination over Au/ZrO_2 catalyst.[481] The addition of H_2 (1 bar) at 100 °C reaction temperature led to complete conversion of myrtenol with 68% amine yield, preserving C=C bond in the initial myrtenol structure. On the other hand, the reduction of both C=C and C=N bonds was possible with the formation of two diastereomers (around 93% yield) when hydrogen was added at 180 °C reaction temperature. Conversion rates and product selectivity in myrtenol amination over nanosized Au-based catalysts were strongly dependent on catalyst pre-activation[482] as well as on the addition of alcohols and formic acid.[483]

4.10 Bioethanol conversion

A promising strategy for the conversion of bio-ethanol into isobutene was developed using nanosized $Zn_xZr_yO_z$ catalysts.[484,485] A high selectivity of isobutene up to 83% at full conversion of bioethanol was obtained at optimized reaction conditions. Selective deposition of ZnO on ZrO_2 led to optimization of ZrO_2 acidity and provided the required basicity, favoring the ethanol-to-isobutene transformation. Optimization of acid sites played a prominent role in controlling undesired reactions of bio-ethanol dehydration and acetone polymerization/coking, resulting in high yields of isobutene. It was suggested that basic sites could catalyze

ethanol dehydrogenation and aldol-condensation reactions to yield acetone, while Brønsted acidic sites promote acetone-to-isobutene reaction pathway. Scandium doped indium oxide was found to be active for bio-ethanol upgrading. However, propylene was obtained as the main product up to 60% yields in the presence of water and hydrogen, outperforming zeolite-based catalysts (propylene yield is up to 20–30%).[486,487]

5. Importance of water in liquid phase biomass valorization

Biomass conversion reactions are mostly carried out in liquid phase, rather than in gas phase normally used in petrochemical industry, because of low thermal stability of biomass feedstocks originating from highly oxygenated species.[488–490] On the other hand, effective utilization of bulky/viscous biomass molecules, facile optimization of process variables, improved product selectivity, and high atom economy are the persuasive factors to carry out biomass conversions in liquid phase. Therefore, liquid phase biomass processing is of great importance for the future biorefineries. Various solvents, including water, ionic liquids, bio-based solvents, and conventional organic solvents have been used for biomass valorization. Water is particularly a desirable solvent because of its high abundance, ecofriendly nature, and ability to solubilize biomass-derived oxygenated products.[490] In addition, water can serve as a reactant, promoter, or as a catalytic active phase for biomass processing (Fig. 33).[491–493] Biomass naturally contains huge moisture contents (30–60%, depending on the source) because water is one of the key reagents for photosynthesis process to produce biomass (Fig. 2). It is obvious that liquid phase biomass processing can result in the generation of significant amounts of water, along with bio-derived chemicals. Moreover, water is a byproduct in the dehydration reaction of various biomass-derived compounds, such as glucose, fructose, xylose, and glycerol. By using water as reaction medium, the process to separate *in situ* generated water formed during biomass conversion, can be simplified by creating a bi-phasic system in which water would be retained in the polar phase, while most bio-derived organic chemicals will reside in the apolar phase. Consequently, energy-intensive steps required for the purification of bio-based chemicals can be avoided, leading to improved product yields with high quality and reduced process costs.

Water is an important reactant for the hydrolysis of various biomass molecules, including lignocellulose, cellulose, hemicellulose, cellobiose, and triglycerides to produce valuable platform molecules.[493–495] Water is also essential for the production of levulinic acid from carbohydrates and HMF. The application of hydrothermal conditions, normally >100 °C and 10 bar, is indispensable for the efficient fractionation of biomass into platform molecules or building blocks.[284] Sometimes, supercritical conditions (374 °C and 221 bar for water) are required to enhance mass transfer properties and to increase reaction rates during biomass processing.[492] Under these sub- and supercritical conditions, water can provide hydronium ions (H_3O^+) and hydroxyl species (OH^-), which have very important roles in biomass conversion. For instance, hydronium ions can act as acidic sites for the acid-catalyzed reactions, especially for the hydrolysis of cellulose to glucose.[37,492,496] On the other hand, hydroxyl species can act as the source of oxygen for biomass oxidation reactions, such as HMF oxidation to 2,5-furandicarboxylic acid[497] and galacturonic acid oxidation to galactaric acid.[498] Recently, Meng *et al.*[499] pointed out the promoting role of water, which can suppress the side reactions of HMF, in the decarbonylation of HMF towards furfuryl alcohol synthesis.

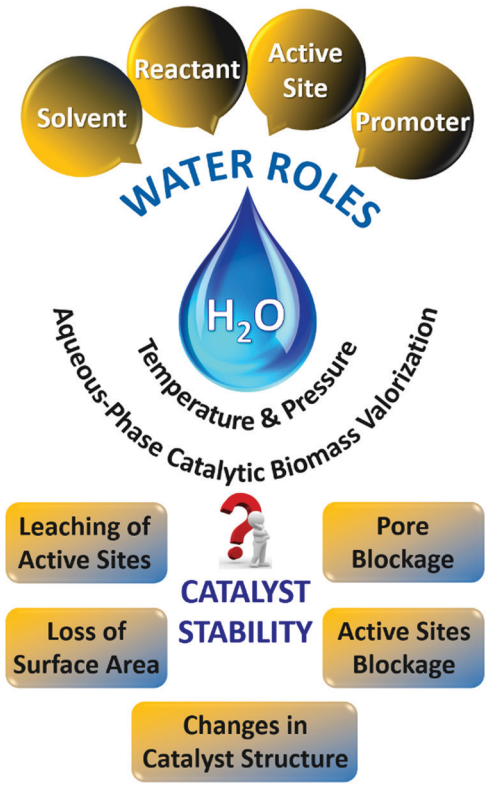

Fig. 33 Importance of water in liquid phase biomass valorization and its impact on catalyst stability.

6. Hydrothermal stability and deactivation of nanoporous catalysts during aqueous phase biomass valorization

Although water plays an important role in liquid phase biomass processing, there are two major concerns of the catalysts that must be taken into consideration when using water as solvent namely, (i) hydrothermal stability and (ii) catalyst deactivation.[489,500,501] These problems are mainly due to the inevitable utilization of harsh hydrothermal reaction conditions, which may degrade catalyst structure and consequently their catalytic performance. The deactivation of a solid catalyst can be determined in terms of undesirable structural changes, active phase leaching, loss of surface area, and blockage of

pores/active sites (Fig. 33). In hot liquid water conditions (>150 °C), desilication or dealumination of zeolites often occurs *via* hydrolysis of Si–O–Si and Si–O–Al bonds, respectively, leading to severe degradation of zeolite frameworks.[8,488,502] Gardner *et al.*[502] found that solvated Al^{3+} ions leached from ZSM-5 zeolite were the active sites for the aqueous phase glucose-to-fructose isomerization (reaction conditions: 170 °C and 30 min). Leaching of Si or Al species into the reaction mixture was drastically induced in the presence of inorganic metal salts, which are naturally present in biomass feedstocks. Since the catalyst active sites (Al^{3+}) were leached into the reaction solution, the ZSM-5 catalyst loses its recycling efficiency for glucose isomerization. Leaching of heterocations from zeolite frameworks was also observed during aqueous phase biomass conversions.[489,503,504] Incorporating heterocations into the zeolite frameworks can stimulate the distortions in bond angles and bond lengths, due to the disparity in host–guest properties. It is therefore obvious that incorporated heterocations can be more rapidly leached compared to constituent atoms (Si or Al) of the zeolites, under the hydrothermal conditions.[47] For instance, leaching of both extra-framework Ti and active framework Ti species from a titanium silicalite zeolite was found during furfural oxidation reaction in aqueous H_2O_2, and thus, rapid catalyst deactivation was observed.[503] The ordered structure of mesoporous silica and its surface area can also be affected adversely at elevated hydrothermal conditions (≥200 °C).[502,505] About 90% loss in the surface area of a mesoporous silica was observed at 200 °C for 10 h hydrothermal treatment due to the degradation of ordered mesoporous structure elicited by the hydrolysis of silica in hot liquid water.

Leaching of metal nanoparticles (*e.g.*, Zn) and acidic species (*e.g.*, –SO_3H) is possible during aqueous phase reactions due to the solvation and chelating effects. For instance, Zn leaching from PdZn[461] and CuZn[464] nanoalloys was found to be the main reason for catalyst deactivation in glycerol hydrogenolysis reaction. Biomass contains several oxygen, nitrogen or sulfur functionalities in the form of sugars or acids, which can form complexes with metal components of the catalysts, accelerating the leaching and the aggregation of metal NPs.[489] Under hydrothermal conditions (>200 °C and autogenous pressure), basic metal oxides (*e.g.*, MgO and γ-Al_2O_3) can form hydroxides with increased solubility in water that can lead to severe metal leaching and drastically reduced catalyst reusability.[506,507] Sulfur leaching *via* hydrolysis of sulfate groups is the primary reason for the deactivation of SO_3H-functionalized porous catalysts in aqueous phase biomass conversions.[508,509] The application of harsh reaction conditions can induce the leaching of metal salts (potassium, calcium and magnesium salts), present in biomass feedstocks, into the reaction solution.[510] These metal ions can replace the protons on the solid acids and can ultimately reduce the concentration of active sites needed for the acid-catalyzed reactions, such as dehydration of carbohydrates to HMF and hydrolysis of cellulose to glucose.

Blockage of pores/active sites by insoluble reaction intermediates/byproducts,[423,504] incorporated metals/catalyst precursors[55,200] or by solvent molecules[511] is another key factor for the deactivation of porous and nanostructured catalysts during aqueous phase biomass conversions. Pore blockage in microporous zeolites and mesoporous silica catalysts can adversely affect their specific surface area as well as the accessibility of active sites (usually present inside the pores). Compared to mesoporous silica catalysts (2–50 nm pore size), zeolites are more prone to suffer pore blockage because of their microporous nature (<2 nm pore size). It was found that insoluble oligomeric byproducts can accumulate predominantly on the outer regions of Sn-beta zeolite and can drastically affect the mass transport properties during retro-aldolization and isomerization of glucose.[504] Incorporation of larger sized metals, such as Ce into the zeolites should be avoided because they can block the micropores, resulting in low conversion rates as observed for the reaction of *tert*-butanol with 3,4-dihydro-2*H*-pyran over Ce/MCM-22 zeolite.[55] Interestingly, the concentration of acid sites in Ce/MCM-22 was not affected by hot water treatment at 160 °C for 48 h. Pore blockage and surface area loss are also possible in mesoporous silica materials if the impregnated catalyst precursors contain very large complex species, like isopolytungstates.[200] In addition to the accumulation of reaction byproducts, accumulation of water molecules on Brønsted acid sites (present in Ag/zeolite catalyst) was also noticed, impeding their accessibility for the reactant molecules, leading to low conversion rates in an alkene oxidation reaction.[511] The polar character of basic metal oxides (*e.g.*, MgO) is the key factor for the accumulation of undesirable nucleophiles (*e.g.*, water and oligomers), which can block the active sites and accelerate catalyst deactivation as observed in aldol condensation of biomass-derived cyclopentanone.[506] Moreover, soluble byproducts obtained during biomass processing or impurities present in biomass can cause fouling or poisoning of catalyst active sites.[512] All the drawbacks emphasized in this section have become a barrier for the practical application of porous and nanostructured catalysts in aqueous phase biomass conversions. Therefore, the development of efficient, durable, and water-tolerant catalysts is essential for sustainable biomass valorization.

Over the last ten years, many useful strategies have been developed to enhance the hydrothermal stability and catalytic performance of porous and nanostructured catalysts for a variety of aqueous phase chemical transformations, including biomass valorization. Improving the hydrophobicity of nanoporous catalysts is one of the most promising strategies to enhance their hydrothermal stability. Moreover, it can enrich the catalyst wettability towards bio-derived organic chemicals. As a result, the direct contact of water molecules with zeolite can be inhibited as shown in Fig. 34.[490] Zeolite frameworks are typically composed of siloxane bonds, but they can also contain hydrophilic silanol (SiOH) groups, which originate from framework siloxy (*i.e.*, SiO^-) defects formed during hydrothermal synthesis of zeolites.[513–515] These SiOH species are known to be the main active sites for the hydrolysis of zeolite frameworks in hot liquid water conditions (>150 °C and autogenous pressure). Hence, the formation of SiOH defects should be prevented to improve hydrothermal stability of the zeolites,

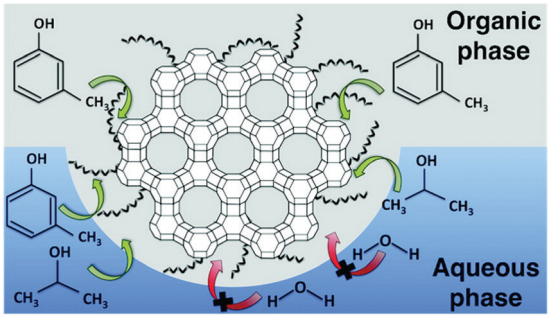

Fig. 34 The behavior of hydrophobized zeolites, prepared by silylation approach, in aqueous and organic phases. Reproduced with permission from ref. 490. Copyright (2012) American Chemical Society.

which can be done by using alternative charge-balancing anions (*i.e.*, F^-). However, this process involves the utilization of environmentally unfriendly media, such as NaF, NH_4F, and HF.[516] In contrast, the functionalization of zeolites by silylation approach has attracted much attention as this strategy allows the anchoring of hydrophobic organosilane groups on the external/internal surfaces of the zeolites.[113,490,513,517] This hydrophobization route using organosilanes can impede the interactions of water molecules with zeolites, thus stabilizing the framework against harsh hydrothermal conditions (Fig. 34).[490] Alternatively, Grand *et al.*[518] used a tungsten incorporation method to inhibit the formation of silanol defects in nanosized MFI-type zeolites. This approach greatly enhanced the structure stability of the zeolites because of the formation of W–O–Si bridges, which are more stable than Si–O–Si bonds.

A structural reconstruction strategy was also found to improve hydrophobicity of nanosized Sn-beta zeolites.[519] This process involves dealumination using HNO_3 treatment, followed by degradation at hydrothermal conditions (140 °C for 45 min) and finally, self-assembly at 140 °C for 1 h. The resulting zeolites showed high catalytic performance in aqueous phase redox reactions, which was attributed to their outstanding hydrophobicity. The selective anchoring of metal organic framework (MOF) nanospheres on a hierarchical zeolite (FAU) assisted to improve its hydrophobic nature, due to the surface functionalization of the zeolite.[520] The degree of surface functionalization and hydrophobicity can be easily tuned by optimizing the amount of deposited MOF and the number of deposition cycles. Zeolite-encapsulated metal nanoparticles may contain contaminated water because of the hydrothermal conditions used for their synthesis.[145] To circumvent this problem, a solvent-free method was used to synthesize AuPd@zeolite catalysts, which exhibited good hydrothermal stability for the aerobic oxidation of bioethanol due to the absence of contaminated water in the catalyst structure.

Zeolitization, silylation, carbon coating, surface modification using functional molecules (*e.g.*, oleic acid), and incorporating heteroatoms (*e.g.*, Co, Ce, or Al) are commonly used methods to improve hydrothermal stability of mesoporous silica materials.[507,521–523] Especially, carbon coating is of great research interest because carbon is hydrophobic, which can

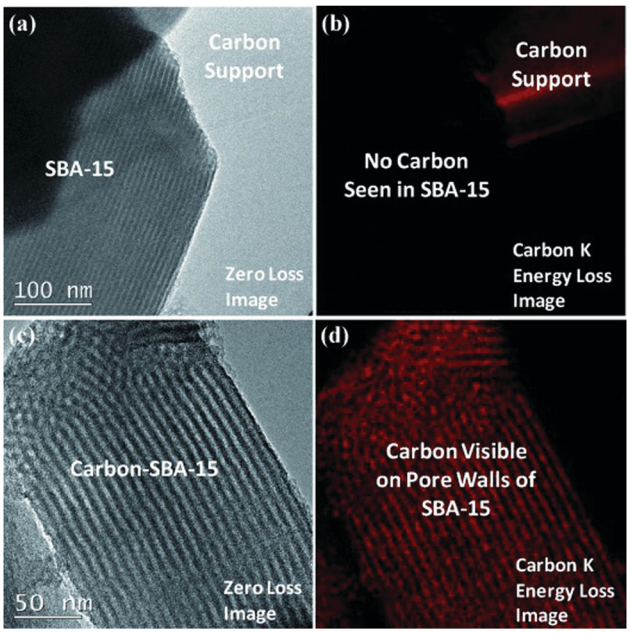

Fig. 35 HRTEM images (a and c) and elemental carbon maps (b and d) of calcined SBA-15 and 10 wt% carbon-coated SBA-15 material. Reproduced with permission from ref. 505. Copyright (2012) John Wiley and Sons.

efficiently prevent the mesoporous silica from hydrolytic attack under hydrothermal conditions. This approach involves the deposition of carbon thin films, obtained by controlled pyrolysis of carbohydrates (*e.g.*, sucrose or glucose), on mesoporous SiO_2. Fig. 35 shows the coating of carbon on the pore walls of SBA-15 material.[505] With metal catalysts supported on carbon-coated mesoporous silica, improved hydrothermal stability and high catalytic performance in aqueous phase biomass conversions were obtained compared with the uncoated analogues.[505,524,525] Pyrolysis of carbon precursor at lower temperature (300 °C rather than 600 °C) is vital to achieve better metal dispersion and improved hydrophobicity for Pd/carbon-coated SBA-15 catalyst.[525] This is because low-temperature pyrolyzed carbon overlayer (300 °C) contains higher amounts of oxygen-containing functional groups, which can stabilize Pd NPs during aqueous phase furfural hydrogenation. The formation of surface hydroxyl groups, responsible for the hydrolysis of Si–O–Si bonds in mesoporous silica, was partially hindered by doping a metal into the SBA-15 material.[521] As a result, the metal-doped SBA-15 materials (metal = Co, Ce, and Al) provided higher hydrothermal stability compared with the undoped material. Oleic acid functionalization strategy was also found to be promising to enhance the hydrophobicity of mesoporous silica due to the formation of strong bonds between carbonyl group of oleic acid with silanol group on mesoporous silica surface.[523] However, a considerable reduction in specific surface area, pore volume, and pore size was observed because of the adsorption of oleic acid molecules on the inner pore surface of mesoporous silica.

The coordination of a metal with another metal or metal oxide is an attractive strategy, not only to achieve enhanced structure–activity properties, but also to improve hydrothermal

stability of nanostructured metal/metal oxide catalysts. For instance, mixed oxide supported metal particles (*e.g.*, Ru/Zr–W–O)[310] and metal oxide supported bimetallic particles (*e.g.*, Pd–Cu/ZrO_2)[326] were found to be highly active for cellulose hydrogenolysis and levulinic acid hydrogenation in aqueous phase, respectively, compared to the pristine counterparts, which was attributed to strong metal–metal and metal–support interactions. Such synergistic interactions were also observed in unsupported mixed oxides, namely SiO_2–Al_2O_3,[269] and La_2O_3–ZrO_2.[526,527] These mixed oxides afforded improved hydrothermal stability and high catalytic performance for the conversion of biomass-derived molecules (*e.g.*, cellobiose, inulin, and acetic acid) to value-added chemicals. Carbon coating, as has been demonstrated for mesoporous silica, also plays a key role in improving hydrothermal stability of metal oxides (*e.g.*, γ-Al_2O_3).[507,528,529] The structural, acid, and redox properties of metal/coated-metal oxide catalysts (*e.g.*, Pd/coated-γ-Al_2O_3) can be controlled by the degree of carbon coating.[528] In contrast to the coating of γ-Al_2O_3 support by carbon layer, Pham *et al.*[507] developed a carbon-overcoated strategy, which can protect the whole structure of metal/metal oxide catalysts (*e.g.*, Cu/γ-Al_2O_3 catalyst) against hydrolytic attack, without showing detrimental effects on their catalytic activity. As a result, carbon-overcoated Cu/γ-Al_2O_3 catalyst presented high hydrothermal stability for the aqueous phase hydrogenation of furfural to furfuryl alcohol compared with the uncoated catalyst. Moreover, the carbon in Cu/γ-Al_2O_3 can be functionalized, providing additional active sites for biomass valorization. On the other hand, O'Neill *et al.*[530] proposed an oxide (alumina) overcoating method for the stabilization of Cu/γ-Al_2O_3 catalyst. This approach greatly prevented Cu sintering and leaching during aqueous phase furfural hydrogenation. It must be noted that γ-Al_2O_3 can convert to soluble boehmite phase (AlOOH) at high hydrothermal conditions (>200 °C) and can result in the degradation of alumina coating.[507] Alkyl phosphonate coating was also found to improve hydrothermal stability of γ-Al_2O_3, attributed to strong Al_2O_3–PO_x bonds, which can inhibit the formation of hydrated boehmite phase. As a result, the specific surface area of functionalized γ-Al_2O_3 was unaffected over a 20 h hydrothermal treatment at 200 °C and autogenous pressure.[531] In recent work, Ngo *et al.*[506] reported a facile strategy to enhance hydrophobicity of basic metal oxides (*e.g.*, MgO) by functionalizing with octadecyltrichlorosilane. The resulting functionalized MgO catalyst exhibited improved hydrothermal stability in the aqueous phase aldol condensation of biomass-derived cyclopentanone, outperforming conventional MgO-based catalysts. In another recent work, the hydrophobicity of Pd/γ-Al_2O_3 catalysts, enhanced by the deposition of organophosphonic acids, played a pivotal role to achieve higher product yields (*p*-cresol) in hydrodeoxygenation of biomass-derived vanillin.[532]

The development of hierarchically porous zeolite- and silica-based catalysts is the utmost potential route to improve mass transport properties during aqueous phase biomass conversions. In this review (Sections 2.4 and 3.3), we have summarized several strategies developed for the synthesis of hierarchical porous catalysts, while discussing the ensuing catalytic effects in the relevant biomass conversions. The deposition of insoluble heavy byproducts on the surface and pores of the catalysts can be prevented by using hydrophobic solvent mixtures (*e.g.*, ethanol/water and GVL/water) instead of pure water.[504,533,534] If the catalyst still contains the deposited insoluble byproducts, a simple calcination step under air atmosphere at the requisite temperature can be used to remove them from the catalyst surface.[503]

7. Conclusions and future prospects

During the last ten years, significant research efforts have been made towards tailoring the porosity and the nanoscale properties of solid catalysts, aiming to develop state-of-the-art catalysts with improved properties for a large spectrum of industrially important catalytic applications. The most promising porous and nanosized materials that have paved the way for exciting scientific discoveries in heterogeneous catalysis are microporous zeolites, mesoporous silicas, and nanoscale metals/metal oxides. Although several important applications of these fascinating catalysts have been reported in the recent literature, their catalytic role in valorizing biomass into useful fine chemicals and biofuels has particularly attracted paramount attention in view of a more sustainable economy and a carbon-neutral society.

In this review, a wide variety of potential catalytic strategies for the valorization of both edible (lipids and starch) and non-edible (lignocellulose) biomass substrates as well as their derived compounds have been demonstrated over microporous zeolites, mesoporous silicas, and nanoscale metals/metal oxides. Despite the nature of biomass feedstock, hydroprocessing is indeed the most appealing route for efficient biomass upgrading.[535] The resulting products can strongly resemble the petro-based products. Since hydroprocessing often involves multiple reaction steps, the development of versatile solid catalysts with adequate amounts of necessary active sites is essential for achieving improved reaction rates. Catalytic fast pyrolysis (CFP) is another attractive process to convert lignocellulose biomass into transportation fuels in a single-step process. Low quality of pyrolytic bio-oil, uncontrolled product selectivity, and fast catalyst deactivation due to coke formation are the major constraints in CFP technology. Hence, the design of efficient and stable solid catalysts that are able to deal with coke as well as with various decomposition intermediates formed during CFP processing, represents a potential solution to tackle the above concerns.[536] Catalytic oxidation is one of the widely used processes in biorefinery research to produce a variety of key platform chemicals for polymer, food, and pharmaceutical industries. The catalytic oxidation of 5-hydroxymethylfurfural (HMF) to 2,5-furandicarboxylic acid (FDCA) is of great importance since FDCA is a promising substitute for petroleum-derived terephthalic acid in the manufacture of poly(ethylene terephthalate) polymer (PET). However, the design of milder and greener reaction methodologies as well as efficient solid catalysts for HMF-to-FDCA transformation remains a great challenge. Catalytic transesterification is another important reaction for valorizing edible biomass, especially lipids (oils & fats) to biodiesel fuel.[537]

In addition, hydrolysis, isomerization, dehydration, esterification, decarbonylation, etherification, and many other processes were also effective in biomass valorization to useful fuels and fine chemicals.

One of the most interesting and challenging subjects in biorefinery is the efficient valorization of lignin, since it is the only scalable and renewable feedstock for the production of aromatic chemicals. In this context, reductive fractionation of lignocellulose using solid catalysts has attracted much attention as this strategy provides two valuable separated fractions: (i) lignin oil containing high-value phenolic compounds and (ii) valorizable solid carbohydrate pulp. The obtained lignin-derived molecules can be upgraded to polymer precursors or fuel-grade chemicals using hydroprocessing reactions. As well, carbohydrate pulp can be used for the production of paper, platform molecules, or biofuels. Over the last five years, notable findings on this novel "lignin-first" biorefinery concept were reported. However, there are still several hurdles that needs to be addressed in this process, including the use of mild reaction conditions, simplifying reaction methodology, as well as improving catalyst selectivity and its reusability.

This review has provided a large number of approaches to tailor unique catalytic properties of microporous zeolites, mesoporous silicas, and nanoscale metals/metal oxides. Doping of heteroatoms into the zeolite structures, developing hierarchical zeolites with wide-ranging pore dimensions, and introducing new active sites by modifying synthesis conditions are some of the vital strategies demonstrated to improve zeolites' properties for efficient biomass valorization. Poor hydrothermal stability in the presence of inorganic salts is one of major disadvantages of zeolites for their applications in biomass upgrading. For example, the presence of NaCl promotes the hydrolysis of Si–O–Al bonds of ZSM-5 zeolite, resulting in the leaching of active Al^{3+} species into the reaction mixture that can catalyze the dehydration reaction of glucose through a homogeneous catalytic process, which is associated with catalyst recovery and reusability concerns.[502] Similar types of modification routes used for the zeolites, such as heteroatom doping, immobilizing acid–base and redox functionalities, multimodal pore structures, and tailoring pore morphologies have been also suggested for mesoporous silica catalysts. Owing to large pore geometries, mesoporous silica catalysts can facilitate efficient diffusion of (bulky) bio-based molecules towards catalytically active sites, thus overcoming mass transport problems often encountered with microporous zeolites. However, mesoporous silica contains negligible amounts of acid sites, which are indispensable for a number of biomass upgrading reactions, such as hydrolysis, hydrodeoxygenation, dehydration, and esterification. Although immobilization of acid functional species (*e.g.*, $-SO_3H$) into the mesoporous silica framework has been attempted, leaching of these acid groups is inevitable during biomass upgrading, due to the application of elevated temperature/pressure conditions as well as the presence of large amounts of water in biomass feedstocks. Pristine mesoporous silica catalysts also suffer from low hydrothermal stability because of their small wall thickness and low degree of cross-linked silicate units.

Nanoscale metals/metal oxides are the most widely used solid catalysts for biomass valorization because of their excellent redox properties and unusual structural defects, along with nanosize-dependent catalytic properties. Tailoring the particle size and morphology of metallic materials at nanoscale range (1–100 nm in at least one dimension) could generate remarkable changes in their structural and electronic properties that could be largely different from the corresponding bulk metal catalysts. Nano-alloys, nanosized metal oxides, metal oxide supported single metal atom catalysts, and shape-controlled metal oxide supported metal NPs are some of the novel, appealing metal-based nanocatalysts discussed in this review in view of their unusual catalytic performances in biomass valorization. However, difficulties in the separation and recovery of nanoscale metal catalysts from reaction mixtures may limit their applications in biomass valorization. A feasible solution to tackle this issue is the development of composite nanocatalysts with magnetic properties. For instance, the addition of magnetic Fe_3O_4 to metal nanocatalysts can provide new nanocomposite catalysts with magnetic properties. The resulting catalysts can be efficiently recovered from the reaction mixtures using external magnetic field without affecting their activity and selectivity.[538] In this review, several useful strategies have been summarized to improve the hydrothermal stability and to inhibit the deactivation of porous and nanostructured catalysts during aqueous phase biomass conversions. However, more stimulating research must be undertaken towards the development of active, multifunctional solid catalysts for the large-scale biomass valorization to produce high yields of fuels and chemicals. Based on the above-mentioned challenges and opportunities, we believe that this comprehensive review may provide useful insights for the design of advanced porous and nanoscale solid catalysts with versatile characteristics (Fig. 36) to support a viable biorefinery.

Fig. 36 Key characteristics of porous and nanoscale catalysts for achieving improved structure–activity performance in biomass valorization.

Conflicts of interest

There are no conflicts to declare.

Acknowledgements

This project has received funding from the European Union's Horizon 2020 research and innovation programme under the Marie Skłodowska-Curie grant agreement number-747968 (project acronym: CATLIGCAR). E. P. acknowledges the Research Foundation of Flanders (FWO Vlaanderen). E. V. M. and B. F. S. thank the Industrial Research Fund of KU Leuven (IOF, grant ZKC8139) and VLAIO (Catalisti cluster SBO project SPICY). V. I. P. kindly acknowledges UEFISCDI for financial support (projects PN-III-P4-ID-PCE-2016-0146 and 32PCCDI-2018). We also acknowledge the financial support from VLAIO/Catalisti (ARBOREF), the Research Foundation Flanders (FWO) (WOG and BioFact Excellence of Science project), and the INTERREG BIO-HArT project which is established by a contribution of the European Interreg V Flanders-The Netherlands program that stimulates innovation, sustainable energy, a healthy environment and the labor market by means of cross-border projects.

References

1 R. Zhang, N. Liu, Z. Lei and B. Chen, *Chem. Rev.*, 2016, **116**, 3658–3721.
2 L. T. Mika, E. Cséfalvay and Á. Németh, *Chem. Rev.*, 2018, **118**, 505–613.
3 A. F. Lee, J. A. Bennett, J. C. Manayil and K. Wilson, *Chem. Soc. Rev.*, 2014, **43**, 7887–7916.
4 R. Lødeng, C. Ranga, T. Rajkhowa, V. I. Alexiadis, H. Bjørkan, S. Chytil, I. H. Svenum, J. Walmsley and J. W. Thybaut, *Biomass Convers. Biorefin.*, 2017, **7**, 343–359.
5 A. Deneyer, E. Peeters, T. Renders, S. Van den Bosch, N. Van Oeckel, T. Ennaert, T. Szarvas, T. I. Korányi, M. Dusselier and B. F. Sels, *Nat. Energy*, 2018, **3**, 969–977.
6 C. Li, X. Zhao, A. Wang, G. W. Huber and T. Zhang, *Chem. Rev.*, 2015, **115**, 11559–11624.
7 Z. Zhang, J. Song and B. Han, *Chem. Rev.*, 2017, **117**, 6834–6880.
8 T. Ennaert, J. Van Aelst, J. Dijkmans, R. De Clercq, W. Schutyser, M. Dusselier, D. Verboekend and B. F. Sels, *Chem. Soc. Rev.*, 2016, **45**, 584–611.
9 Q. Liu, S. C. Chmely and N. Abdoulmoumine, *Energy Fuels*, 2017, **31**, 3525–3536.
10 A. K. Chandel, B. C. M. Gonçalves, J. L. Strap and S. S. da Silva, *Crit. Rev. Biotechnol.*, 2015, **35**, 281–293.
11 A. K. Chandel, V. K. Garlapati, A. K. Singh, F. A. F. Antunes and S. S. da Silva, *Bioresour. Technol.*, 2018, **264**, 370–381.
12 G. Sahu, N. K. Gupta, A. Kotha, S. Saha, S. Datta, P. Chavan, N. Kumari and P. Dutta, *ChemBioEng Rev.*, 2018, **5**, 231–252.
13 G. Pathak, D. Das, K. Rajkumari and L. Rokhum, *Green Chem.*, 2018, **20**, 2365–2373.
14 D. M. Alonso, S. G. Wettstein and J. A. Dumesic, *Chem. Soc. Rev.*, 2012, **41**, 8075–8098.
15 W. Schutyser, S. den Bosch, T. Renders, T. De Boe, S.-F. Koelewijn, A. Dewaele, T. Ennaert, O. Verkinderen, B. Goderis, C. M. Courtin and B. F. Sels, *Green Chem.*, 2015, **17**, 5035–5045.
16 T. Renders, W. Schutyser, S. den Bosch, S.-F. Koelewijn, T. Vangeel, C. M. Courtin and B. F. Sels, *ACS Catal.*, 2016, **6**, 2055–2066.
17 R. Rinaldi, R. Jastrzebski, M. T. Clough, J. Ralph, M. Kennema, P. C. A. Bruijnincx and B. M. Weckhuysen, *Angew. Chem., Int. Ed.*, 2016, **55**, 8164–8215.
18 P. Sudarsanam, R. Zhong, S. Van den Bosch, S. M. Coman, V. I. Parvulescu and B. F. Sels, *Chem. Soc. Rev.*, 2018, **47**, 8349–8402.
19 R. De Clercq, M. Dusselier and B. F. Sels, *Green Chem.*, 2017, **19**, 5012–5040.
20 D. Wang and D. Astruc, *Chem. Soc. Rev.*, 2017, **46**, 816–854.
21 S. Mintova, M. Jaber and V. Valtchev, *Chem. Soc. Rev.*, 2015, **44**, 7207–7233.
22 J. M. Campelo, D. Luna, R. Luque, J. M. Marinas and A. A. Romero, *ChemSusChem*, 2009, **2**, 18–45.
23 Y. Wang, S. De and N. Yan, *Chem. Commun.*, 2016, **52**, 6210–6224.
24 D. Astruc, F. Lu and J. R. Aranzaes, *Angew. Chem., Int. Ed.*, 2005, **44**, 7852–7872.
25 L. D. Rampino and F. F. Nord, *J. Am. Chem. Soc.*, 1941, **63**, 2745–3268.
26 K. E. Kavanagh and F. F. Nord, *J. Am. Chem. Soc.*, 1943, **65**, 2121–2125.
27 G. Parravano, *J. Catal.*, 1970, **18**, 320–328.
28 M. Haruta, N. Yamada, T. Kobayashi and S. Iijima, *J. Catal.*, 1989, **115**, 301–309.
29 J. Liang, Z. Liang, R. Zou and Y. Zhao, *Adv. Mater.*, 2017, **29**, 1701139.
30 D. P. Serrano, J. M. Escola and P. Pizarro, *Chem. Soc. Rev.*, 2013, **42**, 4004–4035.
31 D. Verboekend, N. Nuttens, R. Locus, J. Van Aelst, P. Verolme, J. C. Groen, J. Perez-Ramirez and B. F. Sels, *Chem. Soc. Rev.*, 2016, **45**, 3331–3352.
32 C. T. Kresge and W. J. Roth, *Chem. Soc. Rev.*, 2013, **42**, 3663–3670.
33 L.-B. Sun, X.-Q. Liu and H.-C. Zhou, *Chem. Soc. Rev.*, 2015, **44**, 5092–5147.
34 L. Wang and F.-S. Xiao, *Green Chem.*, 2015, **17**, 24–39.
35 X.-Y. Yang, A. Leonard, A. Lemaire, G. Tian and B.-L. Su, *Chem. Commun.*, 2011, **47**, 2763–2786.
36 M. H. Amin, P. Sudarsanam, M. R. Field, J. Patel and S. K. Bhargava, *Langmuir*, 2017, **33**, 10632–10644.
37 M. Besson, P. Gallezot and C. Pinel, *Chem. Rev.*, 2014, **114**, 1827–1870.
38 C. Gerardin, J. Reboul, M. Bonne and B. Lebeau, *Chem. Soc. Rev.*, 2013, **42**, 4217–4255.
39 S. Abate, K. Barbera, G. Centi, P. Lanzafame and S. Perathoner, *Catal. Sci. Technol.*, 2016, **6**, 2485–2501.
40 M. Xu, C. Mukarakate, D. J. Robichaud, M. R. Nimlos, R. M. Richards and B. G. Trewyn, *Top. Catal.*, 2016, **59**, 73–85.

41 C. Perego, A. Bosetti, M. Ricci and R. Millini, *Energy Fuels*, 2017, **31**, 7721–7733.
42 G. Busca, *Microporous Mesoporous Mater.*, 2017, **254**, 3–16.
43 P. Ferrini, J. Dijkmans, R. De Clercq, S. Van de Vyver, M. Dusselier, P. A. Jacobs and B. F. Sels, *Coord. Chem. Rev.*, 2017, **343**, 220–255.
44 H. Hernando, J. Fermoso, C. Ochoa-Hernández, M. Opanasenko, P. Pizarro, J. M. Coronado, J. Čejka and D. P. Serrano, *Catal. Today*, 2018, **304**, 30–38.
45 X. Querol, N. Moreno, J. C. Umaña, A. Alastuey, E. Hernández, A. López-Soler and F. Plana, *Int. J. Coal Geol.*, 2002, **50**, 413–423.
46 S. De, S. Dutta and B. Saha, *Catal. Sci. Technol.*, 2016, **6**, 7364–7385.
47 H. Y. Luo, J. D. Lewis and Y. Román-Leshkov, *Annu. Rev. Chem. Biomol. Eng.*, 2016, **7**, 663–692.
48 J. Jae, G. A. Tompsett, A. J. Foster, K. D. Hammond, S. M. Auerbach, R. F. Lobo and G. W. Huber, *J. Catal.*, 2011, **279**, 257–268.
49 Y. Wei, T. E. Parmentier, K. P. de Jong and J. Zecevic, *Chem. Soc. Rev.*, 2015, **44**, 7234–7261.
50 B. Smit and T. L. M. Maesen, *Nature*, 2008, **451**, 671–678.
51 H. Li, S. Yang, A. Riisager, A. Pandey, R. S. Sangwan, S. Saravanamurugan and R. Luque, *Green Chem.*, 2016, **18**, 5701–5735.
52 T. C. Keller, E. G. Rodrigues and J. Pérez-Ramírez, *ChemSusChem*, 2014, **7**, 1729–1738.
53 W. Zhang, J. Xie, W. Hou, Y. Liu, Y. Zhou and J. Wang, *ACS Appl. Mater. Interfaces*, 2016, **8**, 23122–23132.
54 A. Herbst and C. Janiak, *CrystEngComm*, 2017, **19**, 4092–4117.
55 B. Gil, W. J. Roth, J. Grzybek, A. Korzeniowska, Z. Olejniczak, M. Eliáš, M. Opanasenko and J. Čejka, *Catal. Today*, 2018, **304**, 22–29.
56 K. Murugappan, C. Mukarakate, S. Budhi, M. Shetty, M. R. Nimlos and Y. Roman-Leshkov, *Green Chem.*, 2016, **18**, 5548–5557.
57 V. Paasikallio, K. Kalogiannis, A. Lappas, J. Lehto and J. Lehtonen, *Energy Technol.*, 2017, **5**, 94–103.
58 P. K. W. Likun, H. Zhang, T. Vitidsant, P. Reubroycharoen and R. Xiao, *Energy Fuels*, 2017, **31**, 6120–6131.
59 H. Zhang, P. K. W. Likun and R. Xiao, *Sci. Total Environ*, 2018, **618**, 151–156.
60 P. Sirous Rezaei, H. Shafaghat and W. M. A. W. Daud, *RSC Adv.*, 2015, **5**, 65408–65414.
61 B. M. E. Chagas, C. Dorado, M. J. Serapiglia, C. A. Mullen, A. A. Boateng, M. A. F. Melo and C. H. Ataíde, *Fuel*, 2016, **179**, 124–134.
62 Y.-K. Park, M. L. Yoo, S. H. Jin and S. H. Park, *Renewable Energy*, 2015, **79**, 20–27.
63 Z. Wang, R. Ma, W. Lin and W. Song, *Int. J. Green Energy*, 2016, **13**, 853–858.
64 Y. Zhang, P. Chen and H. Lou, *J. Energy Chem.*, 2016, **25**, 427–433.
65 C. A. Mullen and A. A. Boateng, *ACS Sustainable Chem. Eng.*, 2015, **3**, 1623–1631.
66 E. L. Schultz, C. A. Mullen and A. A. Boateng, *Energy Technol.*, 2017, **5**, 196–204.
67 L. Mao, Y. Li and Z. C. Zhang, *Front. Chem. Sci. Eng.*, 2018, **12**, 50–58.
68 K. Soongprasit, V. Sricharoenchaikul and D. Atong, *J. Anal. Appl. Pyrolysis*, 2017, **124**, 696–703.
69 G. Kabir, A. T. M. Din and B. H. Hameed, *Bioresour. Technol.*, 2018, **249**, 42–48.
70 Z. Ma, A. Ghosh, N. Asthana and J. van Bokhoven, *ChemCatChem*, 2017, **9**, 954–961.
71 J. R. Christianson, S. Caratzoulas and D. G. Vlachos, *ACS Catal.*, 2015, **5**, 5256–5263.
72 G. Zhang, P. Feng, W. Zhang, H. Liu, C. Wang, H. Ma, D. Wang and Z. Tian, *Microporous Mesoporous Mater.*, 2017, **247**, 158–165.
73 M. Moreno-Recio, J. Santamaría-González and P. Maireles-Torres, *Chem. Eng. J.*, 2016, **303**, 22–30.
74 R. Otomo, T. Yokoi and T. Tatsumi, *ChemCatChem*, 2015, **7**, 4180–4187.
75 L. Li, J. Ding, J.-G. Jiang, Z. Zhu and P. Wu, *Chin. J. Catal.*, 2015, **36**, 820–828.
76 T. D. Swift, H. Nguyen, Z. Erdman, J. S. Kruger, V. Nikolakis and D. G. Vlachos, *J. Catal.*, 2016, **333**, 149–161.
77 T.-Y. Cheng, P.-Y. Chao, Y.-H. Huang, C.-C. Li, H.-Y. Hsu, Y.-S. Chao and T.-C. Tsai, *Microporous Mesoporous Mater.*, 2016, **233**, 148–153.
78 X. Xiang, J. Cui, G. Ding, H. Zheng, Y. Zhu and Y. Li, *ACS Sustainable Chem. Eng.*, 2016, **4**, 4506–4510.
79 L. Bing, Z. Zhang and K. Deng, *Ind. Eng. Chem. Res.*, 2012, **51**, 15331–15336.
80 I. Delidovich, K. Leonhard and R. Palkovits, *Energy Environ. Sci.*, 2014, **7**, 2803–2830.
81 H. Li, S. Saravanamurugan, S. Yang and A. Riisager, *Green Chem.*, 2016, **18**, 726–734.
82 F. Yang, S. Zhang, Z. C. Zhang, J. Mao, S. Li, J. Yin and J. Zhou, *Catal. Sci. Technol.*, 2015, **5**, 4602–4612.
83 J. Cui, J. Tan, T. Deng, X. Cui, Y. Zhu and Y. Li, *Green Chem.*, 2016, **18**, 1619–1624.
84 N. K. Gupta, A. Fukuoka and K. Nakajima, *ACS Catal.*, 2017, **7**, 2430–2436.
85 X. Zhao, G. Yu, J. Li, Y. Feng, L. Zhang, Y. Peng, Y. Tang and L. Wang, *ACS Sustainable Chem. Eng.*, 2018, **6**, 4105–4114.
86 H. P. Winoto, B. S. Ahn and J. Jae, *J. Ind. Eng. Chem.*, 2016, **40**, 62–71.
87 E. Y. C. Jorge, T. de, M. Lima, C. G. S. Lima, L. Marchini, W. N. Castelblanco, D. G. Rivera, E. A. Urquieta-Gonzalez, R. S. Varma and M. W. Paixao, *Green Chem.*, 2017, **19**, 3856–3868.
88 Q. Yao, L. Xu, Z. Han and Y. Zhang, *Chem. Eng. J.*, 2015, **280**, 74–81.
89 M. A. Mellmer, J. M. R. Gallo, D. M. Alonso and J. A. Dumesic, *ACS Catal.*, 2015, **5**, 3354–3359.
90 E. Mahmoud, J. Yu, R. J. Gorte and R. F. Lobo, *ACS Catal.*, 2015, **5**, 6946–6955.
91 M. M. Antunes, S. Lima, P. Neves, A. L. Magalhães, E. Fazio, F. Neri, M. T. Pereira, A. F. Silva, C. M. Silva,

S. M. Rocha, M. Pillinger, A. Urakawa and A. A. Valente, *Appl. Catal., B*, 2016, **182**, 485–503.
92 P. Charoenwiangnuea, T. Maihom, P. Kongpracha, J. Sirijaraensre and J. Limtrakul, *RSC Adv.*, 2016, **6**, 105888–105894.
93 Y. Wang, P. Zhang, G. Huang, Q. Yuan, Y. Guan and P. Wu, *ACS Sustainable Chem. Eng.*, 2017, **5**, 6645–6653.
94 M. E. Sad, L. F. G. Peña, C. L. Padró and C. R. Apesteguía, *Catal. Today*, 2018, **302**, 203–209.
95 P. M. Veiga, A. C. L. Gomes, C. O. Veloso and C. A. Henriques, *Appl. Catal., A*, 2017, **548**, 2–15.
96 G. M. Lari, P. Y. Dapsens, D. Scholz, S. Mitchell, C. Mondelli and J. Perez-Ramirez, *Green Chem.*, 2016, **18**, 1249–1260.
97 J. Dijkmans, M. Dusselier, D. Gabriëls, K. Houthoofd, P. C. M. M. Magusin, S. Huang, Y. Pontikes, M. Trekels, A. Vantomme, L. Giebeler, S. Oswald and B. F. Sels, *ACS Catal.*, 2015, **5**, 928–940.
98 D. Sun, Y. Yamada, S. Sato and W. Ueda, *Green Chem.*, 2017, **19**, 3186–3213.
99 A. S. de Oliveira, S. J. S. Vasconcelos, J. R. de Sousa, F. F. de Sousa, J. M. Filho and A. C. Oliveira, *Chem. Eng. J.*, 2011, **168**, 765–774.
100 L. Huang, F. Qin, Z. Huang, Y. Zhuang, J. Ma, H. Xu and W. Shen, *Ind. Eng. Chem. Res.*, 2016, **55**, 7318–7327.
101 H. Zhang, Z. Hu, L. Huang, H. Zhang, K. Song, L. Wang, Z. Shi, J. Ma, Y. Zhuang, W. Shen, Y. Zhang, H. Xu and Y. Tang, *ACS Catal.*, 2015, **5**, 2548–2558.
102 R. Beerthuis, L. Huang, N. R. Shiju, G. Rothenberg, W. Shen and H. Xu, *ChemCatChem*, 2018, **10**, 211–221.
103 Y. P. Wijaya, I. Kristianto, H. Lee and J. Jae, *Fuel*, 2016, **182**, 588–596.
104 C.-C. Chang, H. Je Cho, J. Yu, R. J. Gorte, J. Gulbinski, P. Dauenhauer and W. Fan, *Green Chem.*, 2016, **18**, 1368–1376.
105 I. F. Teixeira, B. T. W. Lo, P. Kostetskyy, M. Stamatakis, L. Ye, C. C. Tang, G. Mpourmpakis and S. C. E. Tsang, *Angew. Chem., Int. Ed.*, 2016, **55**, 13061–13066.
106 P. Ferrini, S. F. Koelewijn, J. Van Aelst, N. Nuttens and B. F. Sels, *ChemSusChem*, 2017, **10**, 2249–2257.
107 Y. Liao, R. Zhong, E. Makshina, M. d'Halluin, Y. van Limbergen, D. Verboekend and B. F. Sels, *ACS Catal.*, 2018, **8**, 7861–7878.
108 Y. Liao, M. d'Halluin, E. Makshina, D. Verboekend and B. F. Sels, *Appl. Catal., B*, 2018, **234**, 117–129.
109 G. Afreen, T. Patra and S. Upadhyayula, *Mol. Catal.*, 2017, **441**, 122–133.
110 M. Heuchel, F. Reinhardt, N. Merdanoğlu, E. Klemm and Y. Traa, *Microporous Mesoporous Mater.*, 2017, **254**, 59–68.
111 S. Ai, M. Zheng, Y. Jiang, X. Yang, X. Li, J. Pang, J. Sebastian, W. Li, A. Wang, X. Wang and T. Zhang, *AIChE J.*, 2017, **63**, 4032–4042.
112 C. P. Nash, A. Ramanathan, D. A. Ruddy, M. Behl, E. Gjersing, M. Griffin, H. Zhu, B. Subramaniam, J. A. Schaidle and J. E. Hensley, *Appl. Catal., A*, 2016, **510**, 110–124.
113 S. Xu, H. Sheng, T. Ye, D. Hu and S. Liao, *Catal. Commun.*, 2016, **78**, 75–79.
114 C. K. Narula, Z. Li, E. M. Casbeer, R. A. Geiger, M. Moses-Debusk, M. Keller, M. V. Buchanan and B. H. Davison, *Sci. Rep.*, 2015, **5**, 16039.
115 M. A. Sanhoob, O. Muraza, E. N. Shafei, T. Yokoi and K.-H. Choi, *Appl. Catal., B*, 2017, **210**, 432–443.
116 X. Wang, X. Hu, C. Song, K. W. Lux, M. Namazian and T. Imam, *Ind. Eng. Chem. Res.*, 2017, **56**, 12046–12055.
117 L. Zhang, T. N. Pham, J. Faria and D. E. Resasco, *Appl. Catal., A*, 2015, **504**, 119–129.
118 Z. Song, A. Takahashi, N. Mimura and T. Fujitani, *Catal. Lett.*, 2009, **131**, 364–369.
119 W. Xia, A. Takahashi, I. Nakamura, H. Shimada and T. Fujitani, *J. Mol. Catal. A: Chem.*, 2010, **328**, 114–118.
120 C. Duan, X. Zhang, R. Zhou, Y. Hua, J. Chen and L. Zhang, *Catal. Lett.*, 2011, **141**, 1821–1827.
121 F. Xue, C. Miao, Y. Yue, W. Hua and Z. Gao, *Green Chem.*, 2017, **19**, 5582–5590.
122 E. V. Makshina, M. Dusselier, W. Janssens, J. Degreve, P. A. Jacobs and B. F. Sels, *Chem. Soc. Rev.*, 2014, **43**, 7917–7953.
123 E. V. Makshina, W. Janssens, B. F. Sels and P. A. Jacobs, *Catal. Today*, 2012, **198**, 338–344.
124 V. L. Sushkevich and I. I. Ivanova, *ChemSusChem*, 2016, **9**, 2216–2225.
125 P. S. Rezaei, H. Shafaghat and W. M. A. W. Daud, *Green Chem.*, 2016, **18**, 1684–1693.
126 L. Sun, X. Zhang, L. Chen, B. Zhao, S. Yang and X. Xie, *J. Anal. Appl. Pyrolysis*, 2016, **121**, 342–346.
127 S. Cheng, L. Wei, X. Zhao, E. Kadis and J. Julson, *Energy Technol.*, 2016, **4**, 706–713.
128 M. M. Yung, A. K. Starace, C. Mukarakate, A. M. Crow, M. A. Leshnov and K. A. Magrini, *Energy Fuels*, 2016, **30**, 5259–5268.
129 S. Ogo, Y. Okuno, H. Sekine, S. Manabe, T. Yabe, A. Onda and Y. Sekine, *ChemistrySelect*, 2017, **2**, 6201–6205.
130 N. A. S. Ramli and N. A. S. Amin, *Appl. Catal., B*, 2015, **163**, 487–498.
131 N. A. S. Ramli and N. A. S. Amin, *Energy Convers. Manage.*, 2015, **95**, 10–19.
132 W. Zhang, T. Meng, J. Tang, W. Zhuang, Y. Zhou and J. Wang, *ACS Sustainable Chem. Eng.*, 2017, **5**, 10029–10037.
133 Q. Zhang, T. Wang, J. Tan, Q. Zhang, Y. Li and L. Ma, *Int. J. Green Energy*, 2016, **13**, 767–773.
134 C.-B. Chen, M.-Y. Chen, B. Zada, Y.-J. Ma, L. Yan, Q. Xu, W. Li, Q.-X. Guo and Y. Fu, *RSC Adv.*, 2016, **6**, 112477–112485.
135 H. Xia, J. Zhang, X. Yan, S. Xu and L. Yang, *J. Fuel Chem. Technol.*, 2015, **43**, 575–580.
136 A. S. Nagpure, N. Lucas and S. V. Chilukuri, *ACS Sustainable Chem. Eng.*, 2015, **3**, 2909–2916.
137 C. Wang, Z. Liu, L. Wang, X. Dong, J. Zhang, G. Wang, S. Han, X. Meng, A. Zheng and F.-S. Xiao, *ACS Catal.*, 2018, **8**, 474–481.
138 M. Hellinger, H. W. P. Carvalho, S. Baier, D. Wang, W. Kleist and J.-D. Grunwaldt, *Appl. Catal., A*, 2015, **490**, 181–192.
139 L. Wang, F. Yuan, L. Liu, N. Mominou, S. Li, C. Li and W. Wang, *J. Ind. Eng. Chem.*, 2015, **21**, 494–499.

140 X. Xu, E. Jiang, Z. Li and Y. Sun, *Fuel*, 2018, **221**, 440–446.
141 P. S. Rezaei, H. Shafaghat and W. M. A. W. Daud, *RSC Adv.*, 2015, **5**, 51278–51285.
142 F. Wang, X. Kang, M. Zhou, X. Yang, L. Gao and G. Xiao, *Appl. Catal., A*, 2017, **539**, 80–89.
143 S. S. Priya, P. Bhanuchander, V. P. Kumar, S. K. Bhargava and K. V. R. Chary, *Ind. Eng. Chem. Res.*, 2016, **55**, 4461–4472.
144 T. Hanaoka, T. Miyazawa, K. Shimura and S. Hirata, *Chem. Eng. J.*, 2015, **263**, 178–185.
145 J. Zhang, L. Wang, L. Zhu, Q. Wu, C. Chen, X. Wang, Y. Ji, X. Meng and F. Xiao, *ChemSusChem*, 2015, **8**, 2867–2871.
146 H. Chen, Y. Dai, X. Jia, H. Yu and Y. Yang, *Green Chem.*, 2016, **18**, 3048–3056.
147 A. Wang, D. Austin, A. Karmakar, G. M. Bernard, V. K. Michaelis, M. M. Yung, H. Zeng and H. Song, *ACS Catal.*, 2017, **7**, 3681–3692.
148 A. Witsuthammakul and T. Sooknoi, *Catal. Sci. Technol.*, 2016, **6**, 1737–1745.
149 L. Y. Jia, M. Raad, S. Hamieh, J. Toufaily, T. Hamieh, M. M. Bettahar, G. Mauviel, M. Tarrighi, L. Pinard and A. Dufour, *Green Chem.*, 2017, **19**, 5442–5459.
150 T. C. Hoff, D. W. Gardner, R. Thilakaratne, J. Proano-Aviles, R. C. Brown and J.-P. Tessonnier, *Appl. Catal., A*, 2017, **529**, 68–78.
151 D. P. Gamliel, H. J. Cho, W. Fan and J. A. Valla, *Appl. Catal., A*, 2016, **522**, 109–119.
152 M. Asadieraghi and W. M. A. W. Daud, *Energy Convers. Manage.*, 2015, **101**, 151–163.
153 S. C. Oh, T. Nguyendo, Y. He, A. Filie, Y. Wu, D. T. Tran, I. C. Lee and D. Liu, *Catal. Sci. Technol.*, 2017, **7**, 1153–1166.
154 H. Li, Z. Fang, J. Luo and S. Yang, *Appl. Catal., B*, 2017, **200**, 182–191.
155 J. Zhang, L. Wang, G. Wang, F. Chen, J. Zhu, C. Wang, C. Bian, S. Pan and F.-S. Xiao, *ACS Sustainable Chem. Eng.*, 2017, **5**, 3123–3131.
156 S. Song, L. Di, G. Wu, W. Dai, N. Guan and L. Li, *Appl. Catal., B*, 2017, **205**, 393–403.
157 G. M. Lari, B. Puértolas, M. S. Frei, C. Mondelli and J. Pérez-Ramírez, *ChemCatChem*, 2016, **8**, 1507–1514.
158 M. M. Antunes, P. Neves, A. Fernandes, S. Lima, A. F. Silva, M. F. Ribeiro, C. M. Silva, M. Pillinger and A. A. Valente, *Catal. Sci. Technol.*, 2016, **6**, 7812–7829.
159 J. Xing, L. Song, C. Zhang, M. Zhou, L. Yue and X. Li, *Catal. Today*, 2015, **258**, 90–95.
160 L. Wang, J. Zhang, X. Yi, A. Zheng, F. Deng, C. Chen, Y. Ji, F. Liu, X. Meng and F.-S. Xiao, *ACS Catal.*, 2015, **5**, 2727–2734.
161 Y. Zhang, C. Xia, M. Lin, Q. Duan, B. Zhu, X. Peng, B. Wang, S. Yuan, Y. Liu and X. Shu, *Catal. Commun.*, 2017, **101**, 1–4.
162 M. Popova, H. Lazarova, Y. Kalvachev, T. Todorova, Á. Szegedi, P. Shestakova, G. Mali, V. D. B. C. Dasireddy and B. Likozar, *Catal. Commun.*, 2017, **100**, 10–14.
163 Y. Deng, J. Wei, Z. Sun and D. Zhao, *Chem. Soc. Rev.*, 2013, **42**, 4054–4070.
164 W. Li, Q. Yue, Y. Deng and D. Zhao, *Adv. Mater.*, 2013, **25**, 5129–5152.
165 N. Linares, A. M. Silvestre-Albero, E. Serrano, J. Silvestre-Albero and J. Garcia-Martinez, *Chem. Soc. Rev.*, 2014, **43**, 7681–7717.
166 Y. Shi, Y. Wan and D. Zhao, *Chem. Soc. Rev.*, 2011, **40**, 3854–3878.
167 F. Hoffmann, M. Cornelius, J. Morell and M. Fröba, *Angew. Chem., Int. Ed.*, 2006, **45**, 3216–3251.
168 X. Yan, S. Komarneni and Z. Yan, *J. Colloid Interface Sci.*, 2013, **390**, 217–224.
169 P. Akhter, M. Hussain, G. Saracco and N. Russo, *Nanoscale Res. Lett.*, 2014, **9**, 158.
170 S. S. Kim, W. Zhang and T. J. Pinnavaia, *Science*, 1998, **282**, 1302–1305.
171 S. Kerkhofs, T. Willhammar, H. Van Den Noortgate, C. E. A. Kirschhock, E. Breynaert, G. Van Tendeloo, S. Bals and J. A. Martens, *Chem. Mater.*, 2015, **27**, 5161–5169.
172 R. Ciriminna, A. Fidalgo, V. Pandarus, F. Béland, L. M. Ilharco and M. Pagliaro, *Chem. Rev.*, 2013, **113**, 6592–6620.
173 J. Dhainaut, J.-P. Dacquin, A. F. Lee and K. Wilson, *Green Chem.*, 2010, **12**, 296–303.
174 Y. Yang, C. Ochoa-Hernández, P. Pizarro, V. A. de la Peña O'shea, J. M. Coronado and D. P. Serrano, *Appl. Catal., B*, 2016, **197**, 206–213.
175 S. B. A. Hamid, M. M. Ambursa, P. Sudarsanam, L. H. Voon and S. K. Bhargava, *Catal. Commun.*, 2017, **94**, 18–22.
176 J. Andas, F. Adam and I. A. Rahman, *Appl. Surf. Sci.*, 2014, **315**, 154–162.
177 N. Linares, E. Serrano, M. Rico, A. Mariana Balu, E. Losada, R. Luque and J. Garcia-Martinez, *Chem. Commun.*, 2011, **47**, 9024–9035.
178 X. Li, Q. Xia, V. C. Nguyen, K. Peng, X. Liu, N. Essayem and Y. Wang, *Catal. Sci. Technol.*, 2016, **6**, 7586–7596.
179 N. A. Brunelli, K. Venkatasubbaiah and C. W. Jones, *Chem. Mater.*, 2012, **24**, 2433–2442.
180 A. Romero, E. Alonso, Á. Sastre and A. Nieto-Márquez, *Microporous Mesoporous Mater.*, 2016, **224**, 1–8.
181 L. Yang, X. Yang, E. Tian and H. Lin, *ChemSusChem*, 2015, **9**, 36–41.
182 L. Yang, X. Yang, E. Tian, V. Vattipalli, W. Fan and H. Lin, *J. Catal.*, 2016, **333**, 207–216.
183 L. Zhen, F. Gang, P. Chunyan, L. Wang, C. Ping, L. Hui and Z. Xiaoming, *Chin. J. Catal.*, 2012, **33**, 1696–1705.
184 J. Pang, M. Zheng, X. Li, L. Song, R. Sun, J. Sebastian, A. Wang, J. Wang, X. Wang and T. Zhang, *ChemistrySelect*, 2017, **2**, 309–314.
185 M. Moreno-Recio, I. Jiménez-Morales, P. L. Arias, J. Santamaría-González and P. Maireles-Torres, *ChemistrySelect*, 2017, **2**, 2444–2451.
186 V. B. F. Custodis, S. A. Karakoulia, K. S. Triantafyllidis and J. A. van Bokhoven, *ChemSusChem*, 2016, **9**, 1134–1145.
187 S. Jeenpadiphat, C. Kasiban and D. N. Tungasmita, *J. Chem. Technol. Biotechnol.*, 2016, **91**, 2519–2528.
188 T. Mochizuki, D. Atong, S.-Y. Chen, M. Toba and Y. Yoshimura, *Catal. Commun.*, 2013, **36**, 1–4.

189 Y. P. Wijaya, D. J. Suh and J. Jae, *Catal. Commun.*, 2015, **70**, 12–16.
190 M. Di Serio, R. Turco, P. Pernice, A. Aronne, F. Sannino and E. Santacesaria, *Catal. Today*, 2012, **192**, 112–116.
191 H. Teruki, K. Kouji and I. Masakazu, *Chem. Lett.*, 2011, **40**, 614–616.
192 L. Xu, W. Wei, H. Li and H. Li, *ACS Catal.*, 2014, **4**, 251–258.
193 Y. Zhang, Y. Chen, Y. Shen, Y. Yan, J. Pan, W. Shi and L. Yu, *ChemPlusChem*, 2016, **81**, 108–118.
194 Z. Xiao, Y. Fan, Y. Cheng, Q. Zhang, Q. Ge, R. Sha, J. Ji and J. Mao, *Fuel*, 2018, **215**, 406–416.
195 Y. Kuwahara, Y. Magatani and H. Yamashita, *Catal. Today*, 2015, **258**, 262–269.
196 P. Demma Carà, R. Ciriminna, N. R. Shiju, G. Rothenberg and M. Pagliaro, *ChemSusChem*, 2014, **7**, 835–840.
197 F. Yang, Y. Ding, J. Tang, S. Zhou, B. Wang and Y. Kong, *Mol. Catal.*, 2017, **435**, 144–155.
198 W. Wei, Y. Zhao, S. Peng, H. Zhang, Y. Bian, H. Li and H. Li, *ACS Appl. Mater. Interfaces*, 2014, **6**, 20851–20859.
199 J. Chen, F. Lu, J. Zhang, W. Yu, F. Wang, J. Gao and J. Xu, *ChemCatChem*, 2013, **5**, 2822–2826.
200 M. Kaur, R. Malhotra and A. Ali, *Renewable Energy*, 2018, **116**, 109–119.
201 N. Godard, A. Vivian, L. Fusaro, L. Cannavicci, C. Aprile and D. P. Debecker, *ChemCatChem*, 2211, **9**, 2211–2218.
202 Y. Cao, J. Wang, M. Kang and Y. Zhu, *J. Mol. Catal. A: Chem.*, 2014, **381**, 46–53.
203 Z. Xiao, J. Mao, J. Ji, R. Sha, Y. Fan and C. Xing, *J. Fuel Chem. Technol.*, 2017, **45**, 641–650.
204 Z. Xiao, Q. Ge, C. Xing, C. Jiang, S. Fang, J. Ji and J. Mao, *J. Energy Chem.*, 2016, **25**, 434–444.
205 J. Grams, N. Potrzebowska, J. Goscianska, B. Michalkiewicz and A. M. Ruppert, *Int. J. Hydrogen Energy*, 2016, **41**, 8656–8667.
206 A. Romero, A. Nieto-Márquez and E. Alonso, *Appl. Catal., A*, 2017, **529**, 49–59.
207 C. García-Sancho, I. Sádaba, R. Moreno-Tost, J. Mérida-Robles, J. Santamaría-González, M. López-Granados and P. Maireles-Torres, *ChemSusChem*, 2013, **6**, 635–642.
208 S. Srivastava, P. Mohanty, J. K. Parikh, A. K. Dalai, S. S. Amritphale and A. K. Khare, *Chin. J. Catal.*, 2015, **36**, 933–942.
209 S. Li, Y. Wang, L. Gao, Y. Wu, X. Yang, P. Sheng and G. Xiao, *Microporous Mesoporous Mater.*, 2018, **262**, 154–165.
210 C. P. Jiménez-Gómez, J. A. Cecilia, R. Moreno-Tost and P. Maireles-Torres, *ChemSusChem*, 2017, **10**, 1448–1459.
211 Z. Huang, W. Pan, H. Zhou, F. Qin, H. Xu and W. Shen, *ChemSusChem*, 2013, **6**, 1063–1069.
212 C. Tian, X. Zhu, S. Chai, Z. Wu, A. Binder, S. Brown, L. Li, H. Luo, Y. Guo and S. Dai, *ChemSusChem*, 2014, **7**, 1703–1709.
213 Y. Kuwahara, W. Kaburagi, Y. Osada, T. Fujitani and H. Yamashita, *Catal. Today*, 2017, **281**, 418–428.
214 R. Sheikh, G. N. Shao, Z. Khan, N. Abbas, H. Kim and Y. Park, *Asia-Pac. J. Chem. Eng.*, 2015, **10**, 339–346.
215 A. Carrero, A. J. Vizcaíno, J. A. Calles and L. García-Moreno, *J. Energy Chem.*, 2017, **26**, 42–48.
216 M. Harisekhar, V. P. Kumar, S. S. Priya and K. V. R. Chary, *J. Chem. Technol. Biotechnol.*, 2015, **90**, 1906–1917.
217 V. Shanmugam, R. Zapf, S. Neuberg, V. Hessel and G. Kolb, *Appl. Catal., B*, 2017, **203**, 859–869.
218 H.-J. Chae, T.-W. Kim, Y.-K. Moon, H.-K. Kim, K.-E. Jeong, C.-U. Kim and S.-Y. Jeong, *Appl. Catal., B*, 2014, **150–151**, 596–604.
219 J. L. Cheong, Y. Shao, S. J. R. Tan, X. Li, Y. Zhang and S. S. Lee, *ACS Sustainable Chem. Eng.*, 2016, **4**, 4887–4894.
220 W. Janssens, E. V. Makshina, P. Vanelderen, F. De Clippel, K. Houthoofd, S. Kerkhofs, J. A. Martens, P. A. Jacobs and B. F. Sels, *ChemSusChem*, 2015, **8**, 994–1008.
221 G. V. Mamontov, M. V. Grabchenko, V. I. Sobolev, V. I. Zaikovskii and O. V. Vodyankina, *Appl. Catal., A*, 2016, **528**, 161–167.
222 F. G. Baddour, C. P. Nash, J. A. Schaidle and D. A. Ruddy, *Angew. Chem., Int. Ed.*, 2016, **55**, 9026–9029.
223 D. Duraczyńska, A. Michalik-Zym, B. D. Napruszewska, R. Dula, R. P. Socha, L. Lityńska-Dobrzyńska, A. Gaweł, K. Bahranowski and E. M. Serwicka, *ChemistrySelect*, 2016, **1**, 2148–2155.
224 R. N. Olcese, G. Lardier, M. Bettahar, J. Ghanbaja, S. Fontana, V. Carré, F. Aubriet, D. Petitjean and A. Dufour, *ChemSusChem*, 2013, **6**, 1490–1499.
225 Y. Yang, G. Lv, L. Deng, B. Lu, J. Li, J. Zhang, J. Shi and S. Du, *Microporous Mesoporous Mater.*, 2017, **250**, 47–54.
226 T. M. Sankaranarayanan, A. Berenguer, C. Ochoa-Hernández, I. Moreno, P. Jana, J. M. Coronado, D. P. Serrano and P. Pizarro, *Catal. Today*, 2015, **243**, 163–172.
227 N. T. T. Tran, Y. Uemura, S. Chowdhury and A. Ramli, *Appl. Catal., A*, 2016, **512**, 93–100.
228 M. M. Ambursa, P. Sudarsanam, L. H. Voon, S. B. A. Hamid and S. K. Bhargava, *Fuel Process. Technol.*, 2017, **162**, 87–97.
229 N. T. T. Tran, Y. Uemura and A. Ramli, *Procedia Eng.*, 2016, **148**, 1252–1258.
230 X. Zhang, W. Tang, Q. Zhang, T. Wang and L. Ma, *Appl. Energy*, 2018, **227**, 73–79.
231 H. Huang, C. A. Denard, R. Alamillo, A. J. Crisci, Y. Miao, J. A. Dumesic, S. L. Scott and H. Zhao, *ACS Catal.*, 2014, **4**, 2165–2168.
232 Y. Huang, P.-Y. Chao, T.-Y. Cheng, Y. Ho, C.-T. Lin, H.-Y. Hsu, J.-J. Wong and T.-C. Tsai, *Chem. Eng. J.*, 2016, **283**, 778–788.
233 A. Najafi Chermahini, H. Hafizi, N. Andisheh, M. Saraji and A. Shahvar, *Res. Chem. Intermed.*, 2017, **43**, 5507–5521.
234 P. A. Russo, M. M. Antunes, P. Neves, P. V. Wiper, E. Fazio, F. Neri, F. Barreca, L. Mafra, M. Pillinger, N. Pinna and A. A. Valente, *Green Chem.*, 2014, **16**, 4292–4305.
235 J. C. Manayil, V. C. dos Santos, F. C. Jentoft, M. Granollers Mesa, A. F. Lee and K. Wilson, *ChemCatChem*, 2017, **9**, 2231–2238.
236 L. Sherry and J. A. Sullivan, *Catal. Today*, 2011, **175**, 471–476.
237 D. N. Durgasri, T. Vinodkumar, P. Sudarsanam and B. M. Reddy, *Catal. Lett.*, 2014, **144**, 971–979.
238 P. Sudarsanam, K. Kuntaiah and B. M. Reddy, *New J. Chem.*, 2014, **38**, 5991–6001.

239 L. Liu and A. Corma, *Chem. Rev.*, 2018, **118**, 4981–5079.
240 R. C. R. Santos, D. M. V. Braga, A. N. Pinheiro, E. R. Leite, V. N. Freire, E. Longhinotti and A. Valentini, *Catal. Sci. Technol.*, 2016, **6**, 4986–5002.
241 I. E. Wachs and K. Routray, *ACS Catal.*, 2012, **2**, 1235–1246.
242 F. Yang, D. Deng, X. Pan, Q. Fu and X. Bao, *Natl. Sci. Rev.*, 2015, **2**, 183–201.
243 A. S. K. Hashmi and G. J. Hutchings, *Angew. Chem., Int. Ed.*, 2006, **45**, 7896–7936.
244 M. Okumura, T. Fujitani, J. Huang and T. Ishida, *ACS Catal.*, 2015, **5**, 4699–4707.
245 P. Sudarsanam, B. Mallesham, P. S. Reddy, D. Großmann, W. Grünert and B. M. Reddy, *Appl. Catal., B*, 2014, **144**, 900–908.
246 P. Sudarsanam, B. Mallesham, A. Rangaswamy, B. G. Rao, S. K. Bhargava and B. M. Reddy, *J. Mol. Catal. A: Chem.*, 2016, **412**, 47–55.
247 P. Sudarsanam, P. R. Selvakannan, S. K. Soni, S. K. Bhargava and B. M. Reddy, *RSC Adv.*, 2014, **4**, 43460–43469.
248 P. Sudarsanam, B. Mallesham, D. N. Durgasri and B. M. Reddy, *J. Ind. Eng. Chem.*, 2014, **20**, 3115–3121.
249 C. Marsden, E. Taarning, D. Hansen, L. Johansen, S. K. Klitgaard, K. Egeblad and C. H. Christensen, *Green Chem.*, 2008, **10**, 168–170.
250 Y. Li and W. Shen, *Chem. Soc. Rev.*, 2014, **43**, 1543–1574.
251 D. Lei, K. Yu, M.-R. Li, Y. Wang, Q. Wang, T. Liu, P. Liu, L.-L. Lou, G. Wang and S. Liu, *ACS Catal.*, 2017, **7**, 421–432.
252 M. Sankar, N. Dimitratos, P. J. Miedziak, P. P. Wells, C. J. Kiely and G. J. Hutchings, *Chem. Soc. Rev.*, 2012, **41**, 8099–8139.
253 P. Deka, B. J. Borah, H. Saikia and P. Bharali, *Chem. Rec.*, 2018, **18**, 1–13.
254 A. Holewinski, H. Xin, E. Nikolla and S. Linic, *Curr. Opin. Chem. Eng.*, 2013, **2**, 312–319.
255 S. Navalón and H. García, *Nanomaterials*, 2016, **6**, 123.
256 Z. Zhang and G. W. Huber, *Chem. Soc. Rev.*, 2018, **47**, 1351–1390.
257 L. Yang, J. Su, X. Yang and H. Lin, in *Reaction Pathways and Mechanisms in Thermocatalytic Biomass Conversion I.*, ed. M. Schlaf and Z. C. Zhang, Springer Singapore, 2016, pp. 171–202.
258 B. Hammer and J. K. Nørskov, *Impact of Surface Science on Catalysis*, Academic Press, 2000, vol. 45, pp. 71–129.
259 J. K. Nørskov, F. Studt, F. Abild-Pedersen and T. Bligaard, *Fundamental Concepts in Heterogeneous Catalysis. J*, Wiley Online Library, 2014.
260 K. Sun, M. Kohyama, S. Tanaka and S. Takeda, *J. Phys. Chem. A*, 2012, **116**, 9568–9573.
261 Y. Xu and M. Mavrikakis, *J. Phys. Chem. B*, 2003, **107**, 9298–9307.
262 R. K. Rai, D. Tyagi, K. Gupta and S. K. Singh, *Catal. Sci. Technol.*, 2016, **6**, 3341–3361.
263 R. Ferrando, J. Jellinek and R. L. Johnston, *Chem. Rev.*, 2008, **108**, 845–910.
264 M. B. Gawande, R. K. Pandey and R. V. Jayaram, *Catal. Sci. Technol.*, 2012, **2**, 1113–1125.
265 A. S. Burange and M. B. Gawande, *Encyclopedia of Inorganic and Bioinorganic Chemistry*, 2016, pp. 1–19.
266 J. C. Védrine, *Catalysts*, 2017, **7**, 341.
267 B. Govinda Rao, P. Sudarsanam, A. Rangaswamy and B. M. Reddy, *Catal. Lett.*, 2015, **145**, 1436–1445.
268 L. Katta, P. Sudarsanam, B. Mallesham and B. M. Reddy, *Catal. Sci. Technol.*, 2012, **2**, 995–1004.
269 P. Sudarsanam, B. Hillary, M. H. Amin, N. Rockstroh, U. Bentrup, A. Brückner and S. K. Bhargava, *Langmuir*, 2018, **34**, 2663–2673.
270 J. Wang, X. Zhang, Q. Sun, S. Chan and H. Su, *Catal. Commun.*, 2015, **61**, 57–61.
271 M. Watanabe, Y. Aizawa, T. Iida, R. Nishimura and H. Inomata, *Appl. Catal., A*, 2005, **295**, 150–156.
272 G. Pacchioni, *Catal. Lett.*, 2015, **145**, 80–94.
273 X. Xiao, H. Bergstrom, R. Saenger, B. Johnson, R. Sun and A. Peterson, *Catal. Sci. Technol.*, 2018, **8**, 1819–1827.
274 S. Tosoni, H.-Y. T. Chen, A. Ruiz Puigdollers and G. Pacchioni, *Philos. Trans. R. Soc., A*, 2018, **376**, 20170056.
275 T. Prasomsri, T. Nimmanwudipong and Y. Roman-Leshkov, *Energy Environ. Sci.*, 2013, **6**, 1732–1738.
276 D. Chen, Q. Ma, L. Wei, N. Li, Q. Shen, W. Tian, J. Zhou and J. Long, *J. Anal. Appl. Pyrolysis*, 2018, **130**, 169–180.
277 S. M. Schimming, O. D. LaMont, M. König, A. K. Rogers, A. D. D'Amico, M. M. Yung and C. Sievers, *ChemSusChem*, 2015, **8**, 2073–2083.
278 K. A. Rogers and Y. Zheng, *ChemSusChem*, 2016, **9**, 1750–1772.
279 C. A. Gaertner, J. C. Serrano-Ruiz, D. J. Braden and J. A. Dumesic, *Ind. Eng. Chem. Res.*, 2010, **49**, 6027–6033.
280 P. Sudarsanam, L. Katta, G. Thrimurthulu and B. M. Reddy, *J. Ind. Eng. Chem.*, 2013, **19**, 1517–1524.
281 L. Katta, P. Sudarsanam, G. Thrimurthulu and B. M. Reddy, *Appl. Catal., B*, 2010, **101**, 101–108.
282 J.-O. Shim, D.-W. Jeong, W.-J. Jang, K.-W. Jeon, B.-H. Jeon, S. Y. Cho, H.-S. Roh, J.-G. Na, C. H. Ko, Y.-K. Oh and S. S. Han, *Renewable Energy*, 2014, **65**, 36–40.
283 J. N. Chheda, G. W. Huber and J. A. Dumesic, *Angew. Chem., Int. Ed.*, 2007, **46**, 7164–7183.
284 H. Xiong, H. N. Pham and A. K. Datye, *Green Chem.*, 2014, **16**, 4627–4643.
285 A. G. Chakinala, J. K. Chinthaginjala, K. Seshan, W. P. M. van Swaaij, S. R. A. Kersten and D. W. F. Brilman, *Catal. Today*, 2012, **195**, 83–92.
286 M. W. Hahn, J. R. Copeland, A. H. van Pelt and C. Sievers, *ChemSusChem*, 2013, **6**, 2304–2315.
287 B. C. Gates, M. Flytzani-Stephanopoulos, D. A. Dixon and A. Katz, *Catal. Sci. Technol.*, 2017, **7**, 4259–4275.
288 A. Fukuoka and P. L. Dhepe, *Chem. Rec.*, 2009, **9**, 224–235.
289 K. Tomishige, Y. Nakagawa and M. Tamura, *Green Chem.*, 2017, **19**, 2876–2924.
290 H. Saikia, R. Duarah, P. Sudarsanam, S. K. Bhargava and P. Bharali, *ChemistrySelect*, 2017, **2**, 2123–2130.
291 S. J. Tauster, *Acc. Chem. Res.*, 1987, **20**, 389–394.
292 M. Kim and H. Lee, *ACS Sustainable Chem. Eng.*, 2017, **5**, 11371–11376.

293 X. Wang, G. Zhao, H. Zou, Y. Cao, Y. Zhang, R. Zhang, F. Zhang and M. Xian, *Green Chem.*, 2011, **13**, 2690–2695.
294 B. Hillary, P. Sudarsanam, M. H. Amin and S. K. Bhargava, *Langmuir*, 2017, **33**, 1743–1750.
295 S. Putla, M. H. Amin, B. M. Reddy, A. Nafady, K. A. Al Farhan and S. K. Bhargava, *ACS Appl. Mater. Interfaces*, 2015, **7**, 16525–16535.
296 P. Sudarsanam, B. Hillary, B. Mallesham, B. G. Rao, M. H. Amin, A. Nafady, A. M. Alsalme, B. M. Reddy and S. K. Bhargava, *Langmuir*, 2016, **32**, 2208–2215.
297 P. Sudarsanam, B. Hillary, D. K. Deepa, M. H. Amin, B. Mallesham, B. M. Reddy and S. K. Bhargava, *Catal. Sci. Technol.*, 2015, **5**, 3496–3500.
298 P. Sudarsanam and B. Reddy, in *Nanotechnology Commercialization*, ed. T. Tsuzuki, Pan Stanford Publishing, Singapore, 2013, pp. 73–138.
299 X.-F. Yang, A. Wang, B. Qiao, J. Li, J. Liu and T. Zhang, *Acc. Chem. Res.*, 2013, **46**, 1740–1748.
300 W. Schutyser, T. Renders, S. den Bosch, S.-F. Koelewijn, G. T. Beckham and B. F. Sels, *Chem. Soc. Rev.*, 2018, **47**, 852–908.
301 S. den Bosch, T. Renders, S. Kennis, S.-F. Koelewijn, G. den Bossche, T. Vangeel, A. Deneyer, D. Depuydt, C. M. Courtin, J. M. Thevelein, W. Schutyser and B. F. Sels, *Green Chem.*, 2017, **19**, 3313–3326.
302 P. Ferrini and R. Rinaldi, *Angew. Chem., Int. Ed.*, 2014, **53**, 8634–8639.
303 Y.-L. Wang, J.-F. Zheng, S. Yan, Y.-Y. Ye, S.-R. Li, D. Wang and Y.-Q. Liu, *Energy Fuels*, 2017, **31**, 2907–2913.
304 A. P. Tathod and P. L. Dhepe, *Bioresour. Technol.*, 2015, **178**, 36–44.
305 T. He, Z. Jiang, P. Wu, J. Yi, J. Li and C. Hu, *Sci. Rep.*, 2016, **6**, 38623.
306 R. Li, B. Li, X. Kai and T. Yang, *Fuel Process. Technol.*, 2017, **167**, 363–370.
307 P. Sudarsanam, B. Hillary, M. H. Amin, S. B. A. Hamid and S. K. Bhargava, *Appl. Catal., B*, 2016, **185**, 213–224.
308 M. Zheng, J. Pang, R. Sun, A. Wang and T. Zhang, *ACS Catal.*, 2017, **7**, 1939–1954.
309 Z. Tai, J. Zhang, A. Wang, J. Pang, M. Zheng and T. Zhang, *ChemSusChem*, 2013, **6**, 652–658.
310 M. Lucas, K. Fabičovicová and P. Claus, *ChemCatChem*, 2018, **10**, 612–618.
311 C. Liu, C. Zhang, S. Sun, K. Liu, S. Hao, J. Xu, Y. Zhu and Y. Li, *ACS Catal.*, 2015, **5**, 4612–4623.
312 Z. Tan, L. Shi, Y. Zan, G. Miao, S. Li, L. Kong, S. Li and Y. Sun, *Appl. Catal., A*, 2018, **560**, 28–36.
313 X. Jin, J. Shen, W. Yan, M. Zhao, P. S. Thapa, B. Subramaniam and R. V. Chaudhari, *ACS Catal.*, 2015, **5**, 6545–6558.
314 Y. Jia and H. Liu, *Chin. J. Catal.*, 2015, **36**, 1552–1559.
315 A. P. Tathod and P. L. Dhepe, *Green Chem.*, 2014, **16**, 4944–4954.
316 M. Yadav, D. K. Mishra and J.-S. Hwang, *Appl. Catal., A*, 2012, **425–426**, 110–116.
317 L. Yan, Q. Yao and Y. Fu, *Green Chem.*, 2017, **19**, 5527–5547.
318 J. Ftouni, A. Muñoz-Murillo, A. Goryachev, J. P. Hofmann, E. J. M. Hensen, L. Lu, C. J. Kiely, P. C. A. Bruijnincx and B. M. Weckhuysen, *ACS Catal.*, 2016, **6**, 5462–5472.
319 J. Ftouni, H. C. Genuino, A. Muñoz-Murillo, P. C. A. Bruijnincx and B. M. Weckhuysen, *ChemSusChem*, 2017, **10**, 2891–2896.
320 Y. Gao, H. Zhang, A. Han, J. Wang, H. Tan, E. Tok, S. Jaenicke and G. Chuah, *ChemistrySelect*, 2018, **3**, 1343–1351.
321 A. S. Piskun, J. Ftouni, Z. Tang, B. M. Weckhuysen, P. C. A. Bruijnincx and H. J. Heeres, *Appl. Catal., A*, 2018, **549**, 197–206.
322 S. Cao, J. R. Monnier and J. R. Regalbuto, *J. Catal.*, 2017, **347**, 72–78.
323 W. Luo, M. Sankar, A. M. Beale, Q. He, C. J. Kiely, P. C. A. Bruijnincx and B. M. Weckhuysen, *Nat. Commun.*, 2015, **6**, 6540.
324 M. Al-Naji, A. Yepez, A. M. Balu, A. A. Romero, Z. Chen, N. Wilde, H. Li, K. Shih, R. Gläser and R. Luqueb, *J. Mol. Catal. A: Chem.*, 2016, **417**, 145–152.
325 A. M. Hengne and C. V. Rode, *Green Chem.*, 2012, **14**, 1064–1072.
326 S. C. Patankar and G. D. Yadav, *ACS Sustainable Chem. Eng.*, 2015, **3**, 2619–2630.
327 M. Varkolu, V. Velpula, D. R. Burri and S. R. R. Kamaraju, *New J. Chem.*, 2016, **40**, 3261–3267.
328 M. Varkolu, D. R. Burri, S. R. R. Kamaraju, S. B. Jonnalagadda and W. E. van Zyl, *Chem. Eng. Technol.*, 2017, **40**, 719–726.
329 S. Lomate, A. Sultana and T. Fujitani, *Catal. Lett.*, 2018, **148**, 348–358.
330 V. V. Kumar, G. Naresh, M. Sudhakar, C. Anjaneyulu, S. K. Bhargava, J. Tardio, V. K. Reddy, A. H. Padmasri and A. Venugopal, *RSC Adv.*, 2016, **6**, 9872–9879.
331 V. V. Kumar, G. Naresh, S. Deepa, P. G. Bhavani, M. Nagaraju, M. Sudhakar, K. V. R. Chary, J. Tardio, S. K. Bhargava and A. Venugopal, *Appl. Catal., A*, 2017, **531**, 169–176.
332 K. Gupta, R. K. Rai and S. K. Singh, *ChemCatChem*, 2018, **10**, 2326–2349.
333 X. Li, P. Jia and T. Wang, *ACS Catal.*, 2016, **6**, 7621–7640.
334 R. Mariscal, P. Maireles-Torres, M. Ojeda, I. Sadaba and M. Lopez Granados, *Energy Environ. Sci.*, 2016, **9**, 1144–1189.
335 S. M. Rogers, C. R. A. Catlow, C. E. Chan-Thaw, A. Chutia, N. Jian, R. E. Palmer, M. Perdjon, A. Thetford, N. Dimitratos, A. Villa and P. P. Wells, *ACS Catal.*, 2017, **7**, 2266–2274.
336 R. Albilali, M. Douthwaite, Q. He and S. H. Taylor, *Catal. Sci. Technol.*, 2018, **8**, 252–267.
337 J. Wu, G. Gao, J. Li, P. Sun, X. Long and F. Li, *Appl. Catal., B*, 2017, **203**, 227–236.
338 G. M. King, S. Iqbal, P. J. Miedziak, G. L. Brett, S. A. Kondrat, B. R. Yeo, X. Liu, J. K. Edwards, D. J. Morgan, D. K. Knight and G. J. Hutchings, *ChemCatChem*, 2015, **7**, 2122–2129.
339 J. Guo, G. Xu, Z. Han, Y. Zhang, Y. Fu and Q. Guo, *ACS Sustainable Chem. Eng.*, 2014, **2**, 2259–2266.
340 M. Manikandan, A. K. Venugopal, A. S. Nagpure, S. Chilukuri and T. Raja, *RSC Adv.*, 2016, **6**, 3888–3898.

341 K. Gupta and S. K. Singh, *ACS Sustainable Chem. Eng.*, 2018, **6**, 4793–4800.
342 V. S. Marakatti, N. Arora, S. Rai, S. C. Sarma and S. C. Peter, *ACS Sustainable Chem. Eng.*, 2018, **6**, 7325–7338.
343 D. Li, Q. Liu, C. Zhu, H. Wang, C. Cui, C. Wang and L. Ma, *J. Energy Chem.*, 2019, **30**, 34–41.
344 G. Bottari, A. J. Kumalaputri, K. K. Krawczyk, B. L. Feringa, H. J. Heeres and K. Barta, *ChemSusChem*, 2015, **8**, 1323–1327.
345 X. Kong, Y. Zhu, H. Zheng, Y. Zhu and Z. Fang, *ACS Sustainable Chem. Eng.*, 2017, **5**, 11280–11289.
346 J. Ohyama, Y. Hayashi, K. Ueda, Y. Yamamoto, S. Arai and A. Satsuma, *J. Phys. Chem. C*, 2016, **120**, 15129–15136.
347 N. Siddiqui, A. S. Roy, R. Goyal, R. Khatun, C. Pendem, A. N. Chokkapu, A. Bordoloi and R. Bal, *Sustainable Energy Fuels*, 2018, **2**, 191–198.
348 M.-Y. Chen, C.-B. Chen, B. Zada and Y. Fu, *Green Chem.*, 2016, **18**, 3858–3866.
349 B. Seemala, C. M. Cai, C. E. Wyman and P. Christopher, *ACS Catal.*, 2017, **7**, 4070–4082.
350 H. Zhang, M. Okumura and N. Toshima, *J. Phys. Chem. C*, 2011, **115**, 14883–14891.
351 N. Toshima and H. Zhang, *Macromol. Symp.*, 2012, **317–318**, 149–159.
352 H. Zhang and N. Toshima, *J. Colloid Interface Sci.*, 2013, **394**, 166–176.
353 H. Zhang, L. Wang, L. Lu and N. Toshima, *Sci. Rep.*, 2016, **6**, 30752.
354 P. J. Miedziak, H. Alshammari, S. A. Kondrat, T. J. Clarke, T. E. Davies, M. Morad, D. J. Morgan, D. J. Willock, D. W. Knight, S. H. Taylor and G. J. Hutchings, *Green Chem.*, 2014, **16**, 3132–3141.
355 Y. Cao, X. Liu, S. Iqbal, P. J. Miedziak, J. K. Edwards, R. D. Armstrong, D. J. Morgan, J. Wang and G. J. Hutchings, *Catal. Sci. Technol.*, 2016, **6**, 107–117.
356 Y. Cao, S. Iqbal, P. J. Miedziak, D. R. Jones, D. J. Morgan, X. Liu, J. Wang and G. J. Hutchings, *J. Chem. Technol. Biotechnol.*, 2017, **92**, 2246–2253.
357 C. Megías-Sayago, S. Ivanova, C. López-Cartes, M. A. Centeno and J. A. Odriozola, *Catal. Today*, 2017, **279**, 148–154.
358 X. Jin, M. Zhao, M. Vora, J. Shen, C. Zeng, W. Yan, P. S. Thapa, B. Subramaniam and R. V. Chaudhari, *Ind. Eng. Chem. Res.*, 2016, **55**, 2932–2945.
359 E. Derrien, M. Mounguengui-Diallo, N. Perret, P. Marion, C. Pinel and M. Besson, *Ind. Eng. Chem. Res.*, 2017, **56**, 13175–13189.
360 R. Wojcieszak, I. M. Cuccovia, M. A. Silva and L. M. Rossi, *J. Mol. Catal. A: Chem.*, 2016, **422**, 35–42.
361 X. Tong, L. Yu, H. Chen, X. Zhuang, S. Liao and H. Cui, *Catal. Commun.*, 2017, **90**, 91–94.
362 S. Siankevich, G. Savoglidis, Z. Fei, G. Laurenczy, D. T. L. Alexander, N. Yan and P. J. Dyson, *J. Catal.*, 2014, **315**, 67–74.
363 N. K. Gupta, S. Nishimura, A. Takagaki and K. Ebitani, *Green Chem.*, 2011, **13**, 824–827.
364 A. Lolli, S. Albonetti, L. Utili, R. Amadori, F. Ospitali, C. Lucarelli and F. Cavani, *Appl. Catal., A*, 2015, **504**, 408–419.
365 A. Lolli, R. Amadori, C. Lucarelli, M. G. Cutrufello, E. Rombi, F. Cavani and S. Albonetti, *Microporous Mesoporous Mater.*, 2016, **226**, 466–475.
366 Z. Miao, T. Wu, J. Li, T. Yi, Y. Zhang and X. Yang, *RSC Adv.*, 2015, **5**, 19823–19829.
367 S. Albonetti, A. Lolli, V. Morandi, A. Migliori, C. Lucarelli and F. Cavani, *Appl. Catal., B*, 2015, **163**, 520–530.
368 D. K. Mishra, J. K. Cho and Y. J. Kim, *J. Ind. Eng. Chem.*, 2018, **60**, 513–519.
369 X. Han, C. Li, X. Liu, Q. Xia and Y. Wang, *Green Chem.*, 2017, **19**, 996–1004.
370 F. Neaţu, R. S. Marin, M. Florea, N. Petrea, O. D. Pavel and V. I. Pârvulescu, *Appl. Catal., B*, 2016, **180**, 751–757.
371 K. Yu, Y. Liu, D. Lei, Y. Jiang, Y. Wang, Y. Feng, L.-L. Lou, S. Liu and W. Zhou, *Catal. Sci. Technol.*, 2018, **8**, 2299–2303.
372 Z. Gui, S. Saravanamurugan, W. Cao, L. Schill, L. Chen, Z. Qi and A. Riisager, *ChemistrySelect*, 2017, **2**, 6632–6639.
373 A. Jain, S. C. Jonnalagadda, K. V. Ramanujachary and A. Mugweru, *Catal. Commun.*, 2015, **58**, 179–182.
374 Z. Yang, W. Qi, R. Su and Z. He, *ACS Sustainable Chem. Eng.*, 2017, **5**, 4179–4187.
375 K. Gupta, R. K. Rai, A. D. Dwivedi and S. K. Singh, *ChemCatChem*, 2016, **9**, 2760–2767.
376 J. Zakzeski and B. M. Weckhuysen, *ChemSusChem*, 2011, **4**, 369–378.
377 C. G. Boeriu, F. I. Fiţigău, R. J. A. Gosselink, A. E. Frissen, J. Stoutjesdijk and F. Peter, *Ind. Crops Prod.*, 2014, **62**, 481–490.
378 X. Huang, T. I. Korányi, M. D. Boot and E. J. M. Hensen, *ChemSusChem*, 2014, **7**, 2276–2288.
379 X. Huang, C. Atay, T. I. Korányi, M. D. Boot and E. J. M. Hensen, *ACS Catal.*, 2015, **5**, 7359–7370.
380 T. I. Korányi, X. Huang, A. E. Coumans and E. J. M. Hensen, *ACS Sustainable Chem. Eng.*, 2017, **5**, 3535–3543.
381 M. Chen, X. Ma, R. Ma, Z. Wen, F. Yan, K. Cui, H. Chen and Y. Li, *Ind. Eng. Chem. Res.*, 2017, **56**, 14025–14033.
382 J. Zhang, J. Teo, X. Chen, H. Asakura, T. Tanaka, K. Teramura and N. Yan, *ACS Catal.*, 2014, **4**, 1574–1583.
383 A. Kloekhorst and H. J. Heeres, *ACS Sustainable Chem. Eng.*, 2015, **3**, 1905–1914.
384 X. Wang and R. Rinaldi, *ChemSusChem*, 2012, **5**, 1455–1466.
385 J. Zhang, Y. Cai, G. Lu and C. Cai, *Green Chem.*, 2016, **18**, 6229–6235.
386 J. Kong, B. Li and C. Zhao, *RSC Adv.*, 2016, **6**, 71940–71951.
387 W. Schutyser, G. Van den Bossche, A. Raaffels, S. Van den Bosch, S.-F. Koelewijn, T. Renders and B. F. Sels, *ACS Sustainable Chem. Eng.*, 2016, **4**, 5336–5346.
388 W. Schutyser, S. den Bosch, J. Dijkmans, S. Turner, M. Meledina, G. Van Tendeloo, D. P. Debecker and B. F. Sels, *ChemSusChem*, 2015, **8**, 1805–1818.
389 J. Yi, Y. Luo, T. He, Z. Jiang, J. Li and C. Hu, *Catalysts*, 2016, **6**, 12.
390 T. Prasomsri, M. Shetty, K. Murugappan and Y. Roman-Leshkov, *Energy Environ. Sci.*, 2014, **7**, 2660–2669.
391 M. Shetty, K. Murugappan, W. H. Green and Y. Román-Leshkov, *ACS Sustainable Chem. Eng.*, 2017, **5**, 5293–5301.

392 X. Zhang, J. Tang, Q. Zhang, Q. Liu, Y. Li, L. Chen, C. Wang and L. Ma, *Catal. Today*, 2019, **319**, 41–47.
393 K. Cui, L. Yang, Z. Ma, F. Yan, K. Wu, Y. Sang, H. Chen and Y. Li, *Appl. Catal., B*, 2017, **219**, 592–602.
394 V. O. O. Gonçalves, C. Ciotonea, S. Arrii-Clacens, N. Guignard, C. Roudaut, J. Rousseau, J.-M. Clacens, S. Royer and F. Richard, *Appl. Catal., B*, 2017, **214**, 57–66.
395 X. Liu, W. Jia, G. Xu, Y. Zhang and Y. Fu, *ACS Sustainable Chem. Eng.*, 2017, **5**, 8594–8601.
396 J. Mao, J. Zhou, Z. Xia, Z. Wang, Z. Xu, W. Xu, P. Yan, K. Liu, X. Guo and Z. C. Zhang, *ACS Catal.*, 2017, **7**, 695–705.
397 W. Guan, X. Chen, S. Jin, C. Li, C.-W. Tsang and C. Liang, *Ind. Eng. Chem. Res.*, 2017, **56**, 14034–14042.
398 M. Zhou, J. Ye, P. Liu, J. Xu and J. Jiang, *ACS Sustainable Chem. Eng.*, 2017, **5**, 8824–8835.
399 X. Liu, W. An, Y. Wang, C. H. Turner and D. E. Resasco, *Catal. Sci. Technol.*, 2018, **8**, 2146–2158.
400 M. Lu, J. Zhu, M. Li, Y. Shan, M. He and C. Song, *Energy Fuels*, 2016, **30**, 6671–6676.
401 M. Lu, H. Du, B. Wei, J. Zhu, M. Li, Y. Shan and C. Song, *Energy Fuels*, 2017, **31**, 10858–10865.
402 M. Lu, H. Du, B. Wei, J. Zhu, M. Li, Y. Shan, J. Shen and C. Song, *Ind. Eng. Chem. Res.*, 2017, **56**, 12070–12079.
403 G.-Y. Xu, J.-H. Guo, Y.-C. Qu, Y. Zhang, Y. Fu and Q.-X. Guo, *Green Chem.*, 2016, **18**, 5510–5517.
404 B. Han, Z. Bao, T. Liu, H. Zhou, G. Zhuang, X. Zhong, S. Deng and J. Wang, *ChemistrySelect*, 2017, **2**, 9599–9606.
405 R. C. Nelson, B. Baek, P. Ruiz, B. Goundie, A. Brooks, M. C. Wheeler, B. G. Frederick, L. C. Grabow and R. N. Austin, *ACS Catal.*, 2015, **5**, 6509–6523.
406 M. M. Ambursa, T. H. Ali, H. V. Lee, P. Sudarsanam, S. K. Bhargava and S. B. A. Hamid, *Fuel*, 2016, **180**, 767–776.
407 F. Su and Y. Guo, *Green Chem.*, 2014, **16**, 2934–2957.
408 A. M. Ruhul, M. A. Kalam, H. H. Masjuki, I. M. R. Fattah, S. S. Reham and M. M. Rashed, *RSC Adv.*, 2015, **5**, 101023–101044.
409 W. Xie and T. Wang, *Fuel Process. Technol.*, 2013, **109**, 150–155.
410 S. Furuta, H. Matsuhashi and K. Arata, *Catal. Commun.*, 2004, **5**, 721–723.
411 D. E. López, J. G. Goodwin, D. A. Bruce and S. Furuta, *Appl. Catal., A*, 2008, **339**, 76–83.
412 K. Jacobson, R. Gopinath, L. C. Meher and A. K. Dalai, *Appl. Catal., B*, 2008, **85**, 86–91.
413 C. Komintarachat and S. Chuepeng, *Ind. Eng. Chem. Res.*, 2009, **48**, 9350–9353.
414 A. Guldhe, P. Singh, F. A. Ansari, B. Singh and F. Bux, *Fuel*, 2017, **187**, 180–188.
415 M. Veillette, A. Giroir-Fendler, N. Faucheux and M. Heitz, *Chem. Eng. J.*, 2017, **308**, 101–109.
416 Y.-M. Park, D.-W. Lee, D.-K. Kim, J.-S. Lee and K.-Y. Lee, *Catal. Today*, 2008, **131**, 238–243.
417 V. C. dos Santos, K. Wilson, A. F. Lee and S. Nakagaki, *Appl. Catal., B*, 2015, **162**, 75–84.
418 Ž. Kesić, I. Lukić, M. Zdujić, Č. Jovalekić, V. Veljković and D. Skala, *Fuel Process. Technol.*, 2016, **143**, 162–168.
419 M. Kouzu, A. Fujimori, T. Suzuki, K. Koshi and H. Moriyasu, *Fuel Process. Technol.*, 2017, **165**, 94–101.
420 N. Kaur and A. Ali, *RSC Adv.*, 2015, **5**, 13285–13295.
421 G. Moradi, M. Mohadesi, R. Rezaei and R. Moradi, *Can. J. Chem. Eng.*, 2015, **93**, 1531–1538.
422 R. G. Prado, G. D. Almeida, A. R. de Oliveira, P. M. T. G. de Souza, C. C. Cardoso, V. R.-L. Constantino, F. G. Pinto, J. Tronto and V. M. D. Pasa, *Energy Fuels*, 2016, **30**, 6662–6670.
423 N. Kaur and A. Ali, *RSC Adv.*, 2014, **4**, 43671–43681.
424 K. Faungnawakij, B. Yoosuk, S. Namuangruk, P. Krasae, N. Viriya-empikul and B. Puttasawat, *ChemCatChem*, 2012, **4**, 209–216.
425 B. Katryniok, H. Kimura, E. Skrzynska, J.-S. Girardon, P. Fongarland, M. Capron, R. Ducoulombier, N. Mimura, S. Paul and F. Dumeignil, *Green Chem.*, 2011, **13**, 1960–1979.
426 A. Villa, N. Dimitratos, C. E. Chan-Thaw, C. Hammond, L. Prati and G. J. Hutchings, *Acc. Chem. Res.*, 2015, **48**, 1403–1412.
427 P. S. Reddy, P. Sudarsanam, G. Raju and B. M. Reddy, *Catal. Commun.*, 2010, **11**, 1224–1228.
428 P. S. Reddy, P. Sudarsanam, B. Mallesham, G. Raju and B. M. Reddy, *J. Ind. Eng. Chem.*, 2011, **17**, 377–381.
429 B. Mallesham, P. Sudarsanam, G. Raju and B. M. Reddy, *Green Chem.*, 2013, **15**, 478–489.
430 P. S. Reddy, P. Sudarsanam, G. Raju and B. M. Reddy, *J. Ind. Eng. Chem.*, 2012, **18**, 648–654.
431 P. Sudarsanam, B. Mallesham, A. N. Prasad, P. S. Reddy and B. M. Reddy, *Fuel Process. Technol.*, 2013, **106**, 539–545.
432 B. Mallesham, P. Sudarsanam and B. M. Reddy, *Catal. Sci. Technol.*, 2014, **4**, 803–813.
433 B. Mallesham, P. Sudarsanam and B. M. Reddy, *Ind. Eng. Chem. Res.*, 2014, **53**, 18775–18785.
434 S. E. Davis, M. S. Ide and R. J. Davis, *Green Chem.*, 2013, **15**, 17–45.
435 G. Dodekatos and H. Tüysüz, *ChemCatChem*, 2017, **9**, 610–619.
436 S. M. Rogers, C. R. A. Catlow, C. E. Chan-Thaw, D. Gianolio, E. K. Gibson, A. L. Gould, N. Jian, A. J. Logsdail, R. E. Palmer, L. Prati, N. Dimitratos, A. Villa and P. P. Wells, *ACS Catal.*, 2015, **5**, 4377–4384.
437 C. D'Agostino, G. Brett, G. Divitini, C. Ducati, G. J. Hutchings, M. D. Mantle and L. F. Gladden, *ACS Catal.*, 2017, **7**, 4235–4241.
438 E. Skrzynska, S. Zaid, A. Addad, J.-S. Girardon, M. Capron and F. Dumeignil, *Catal. Sci. Technol.*, 2016, **6**, 3182–3196.
439 J. A. Díaz, E. Skrzyńska, S. Zaid, J. Girardon, M. Capron, F. Dumeignil and P. Fongarland, *J. Chem. Technol. Biotechnol.*, 2017, **92**, 2267–2275.
440 S. Zaid, E. Skrzyńska, A. Addad, S. Nandi, L. Jalowiecki-Duhamel, J.-S. Girardon, M. Capron and F. Dumeignil, *Top. Catal.*, 2017, **60**, 1072–1081.
441 C. M. Olmos, L. E. Chinchilla, E. G. Rodrigues, J. J. Delgado, A. B. Hungría, G. Blanco, M. F. R. Pereira, J. J. M. Órfão, J. J. Calvino and X. Chen, *Appl. Catal., B*, 2016, **197**, 222–235.

442 I. Kaskow, P. Decyk and I. Sobczak, *Appl. Surf. Sci.*, 2018, **444**, 197–207.
443 D. Roy, B. Subramaniam and R. V. Chaudhari, *ACS Catal.*, 2011, **1**, 548–551.
444 G.-Y. Yang, Y.-H. Ke, H.-F. Ren, C.-L. Liu, R.-Z. Yang and W.-S. Dong, *Chem. Eng. J.*, 2016, **283**, 759–767.
445 R. Palacio, S. Torres, D. Lopez and D. Hernandez, *Catal. Today*, 2018, **302**, 196–202.
446 M. Dusselier, P. Van Wouwe, A. Dewaele, E. Makshina and B. F. Sels, *Energy Environ. Sci.*, 2013, **6**, 1415–1442.
447 R. De Clercq, M. Dusselier, E. Makshina and B. F. Sels, *Angew. Chem., Int. Ed.*, 2018, **57**, 3074–3078.
448 K. Omata, S. Izumi, T. Murayama and W. Ueda, *Catal. Today*, 2013, **201**, 7–11.
449 L.-Z. Tao, B. Yan, Y. Liang and B.-Q. Xu, *Green Chem.*, 2013, **15**, 696–705.
450 G. S. Foo, D. Wei, D. S. Sholl and C. Sievers, *ACS Catal.*, 2014, **4**, 3180–3192.
451 M. Dalil, D. Carnevali, M. Edake, A. Auroux, J.-L. Dubois and G. S. Patience, *J. Mol. Catal. A: Chem.*, 2016, **421**, 146–155.
452 R. Beerthuis, G. Rothenberg and N. R. Shiju, *Green Chem.*, 2015, **17**, 1341–1361.
453 K. Omata, K. Matsumoto, T. Murayama and W. Ueda, *Catal. Today*, 2016, **259**, 205–212.
454 F. Wang, J. Xu, J. Dubois and W. Ueda, *ChemSusChem*, 2010, **3**, 1383–1389.
455 C. Chen, N. Kosuke, T. Murayama and W. Ueda, *ChemCatChem*, 2013, **5**, 2869–2873.
456 K. Omata, K. Matsumoto, T. Murayama and W. Ueda, *Chem. Lett.*, 2014, **43**, 435–437.
457 B. Mallesham, P. Sudarsanam, B. V. S. Reddy and B. M. Reddy, *Appl. Catal., B*, 2016, **181**, 47–57.
458 J. Wang, X. Zhao, N. Lei, L. Li, L. Zhang, S. Xu, S. Miao, X. Pan, A. Wang and T. Zhang, *ChemSusChem*, 2016, **9**, 784–790.
459 X. Zhao, J. Wang, M. Yang, N. Lei, L. Li, B. Hou, S. Miao, X. Pan, A. Wang and T. Zhang, *ChemSusChem*, 2017, **10**, 819–824.
460 A. J. Pamphile-Adrián, P. P. Florez-Rodriguez, M. H. M. Pires, G. Perez and F. B. Passos, *Catal. Today*, 2017, **289**, 302–308.
461 Q. Sun, S. Wang and H. Liu, *ACS Catal.*, 2017, **7**, 4265–4275.
462 V. Rekha, N. Raju, C. Sumana, S. Paul Douglas and N. Lingaiah, *Catal. Lett.*, 2016, **146**, 1487–1496.
463 F. Cai, W. Zhu and G. Xiao, *Catal. Sci. Technol.*, 2016, **6**, 4889–4900.
464 D. Durán-Martín, M. L. Granados, J. L. G. Fierro, C. Pinel and R. Mariscal, *Top. Catal.*, 2017, **60**, 1062–1071.
465 S. García-Fernández, I. Gandarias, Y. Tejido-Núñez, J. Requies and P. L. Arias, *ChemCatChem*, 2017, **9**, 4508–4519.
466 M. Gu, Z. Shen, L. Yang, B. Peng, W. Dong, W. Zhang and Y. Zhang, *Ind. Eng. Chem. Res.*, 2017, **56**, 13572–13581.
467 X. Li, B. Zhang, Q. Wu, C. Zhang, Y. Yu, Y. Li, W. Lin, H. Cheng and F. Zhao, *J. Catal.*, 2016, **337**, 284–292.
468 X. Li, Q. Wu, B. Zhang, C. Zhang, W. Lin, H. Cheng and F. Zhao, *Catal. Today*, 2018, **302**, 210–216.
469 I. C. Freitas, R. L. Manfro and M. M. V. M. Souza, *Appl. Catal., B*, 2018, **220**, 31–41.
470 V. V. Costa, M. Estrada, Y. Demidova, I. Prosvirin, V. Kriventsov, R. F. Cotta, S. Fuentes, A. Simakov and E. V. Gusevskaya, *J. Catal.*, 2012, **292**, 148–156.
471 S. Ajaikumar, J. Ahlkvist, W. Larsson, A. Shchukarev, A.-R. Leino, K. Kordas and J.-P. Mikkola, *Appl. Catal., A*, 2011, **392**, 11–18.
472 F. Neaţu, G. Culică, M. Florea, V. I. Parvulescu and F. Cavani, *ChemSusChem*, 2016, **9**, 3102–3112.
473 A. Stolle, T. Gallert, C. Schmoger and B. Ondruschka, *RSC Adv.*, 2013, **3**, 2112–2153.
474 G. Neri, G. Rizzo, A. S. Aricò, C. Crisafulli, L. De Luca, A. Donato, M. G. Musolino and R. Pietropaolo, *Appl. Catal., A*, 2007, **325**, 15–24.
475 C. I. Melo, R. Bogel-Lukasik, M. G. da Silva and E. Bogel-Lukasik, *Green Chem.*, 2011, **13**, 2825–2830.
476 T. Ekou, L. Ekou, A. Vicente, G. Lafaye, S. Pronier, C. Especel and P. Marécot, *J. Mol. Catal. A: Chem.*, 2011, **337**, 82–88.
477 J. Zhou, Y. Yang, C. Li, S. Zhang, Y. Chen, S. Shi and M. Wei, *J. Mater. Chem. A*, 2016, **4**, 12825–12832.
478 L. Yang, Z. Jiang, G. Fan and F. Li, *Catal. Sci. Technol.*, 2014, **4**, 1123–1131.
479 W. Li, G. Fan, L. Yang and F. Li, *Catal. Sci. Technol.*, 2016, **6**, 2337–2348.
480 Y. S. Demidova, I. L. Simakova, M. Estrada, S. Beloshapkin, E. V. Suslov, D. V. Korchagina, K. P. Volcho, N. F. Salakhutdinov, A. V. Simakov and D. Y. Murzin, *Appl. Catal., A*, 2013, **464–465**, 348–356.
481 Y. S. Demidova, E. V. Suslov, I. L. Simakova, E. S. Mozhajcev, D. V. Korchagina, K. P. Volcho, N. F. Salakhutdinov, A. Simakov and D. Y. Murzin, *J. Mol. Catal. A: Chem.*, 2017, **426**, 60–67.
482 I. L. Simakova, Y. S. Demidova, M. Estrada, S. Beloshapkin, E. V. Suslov, K. P. Volcho, N. F. Salakhutdinov, D. Y. Murzin and A. Simakov, *Catal. Today*, 2017, **279**, 63–70.
483 Y. S. Demidova, E. V. Suslov, I. L. Simakova, K. P. Volcho, E. Smolentseva, N. F. Salakhutdinov, A. Simakov and D. Y. Murzin, *Mol. Catal.*, 2017, **433**, 414–419.
484 J. Sun, K. Zhu, F. Gao, C. Wang, J. Liu, C. H. F. Peden and Y. Wang, *J. Am. Chem. Soc.*, 2011, **133**, 11096–11099.
485 C. Liu, J. Sun, C. Smith and Y. Wang, *Appl. Catal., A*, 2013, **467**, 91–97.
486 S. Mizuno, M. Kurosawa, M. Tanaka and M. Iwamoto, *Chem. Lett.*, 2012, **41**, 892–894.
487 M. Iwamoto, S. Mizuno and M. Tanaka, *Chem. – Eur. J.*, 2013, **19**, 7214–7220.
488 T. Ennaert, J. Geboers, E. Gobechiya, C. M. Courtin, M. Kurttepeli, K. Houthoofd, C. E. A. Kirschhock, P. C. M. M. Magusin, S. Bals, P. A. Jacobs and B. F. Sels, *ACS Catal.*, 2015, **5**, 754–768.
489 I. Sádaba, M. López Granados, A. Riisager and E. Taarning, *Green Chem.*, 2015, **17**, 4133–4145.
490 P. A. Zapata, J. Faria, M. P. Ruiz, R. E. Jentoft and D. E. Resasco, *J. Am. Chem. Soc.*, 2012, **134**, 8570–8578.

491 A. Kruse and N. Dahmen, *J. Supercrit. Fluids*, 2015, **96**, 36–45.
492 K. Wu, Y. Wu, Y. Chen, H. Chen, J. Wang and M. Yang, *ChemSusChem*, 2016, **9**, 1355–1385.
493 L. T. Mika, E. Cséfalvay and I. T. Horváth, *Catal. Today*, 2015, **247**, 33–46.
494 L. Vilcocq, É. Rebmann, Y. W. Cheah and P. Fongarland, *ACS Sustainable Chem. Eng.*, 2018, **6**, 5555–5565.
495 L. Negahdar, I. Delidovich and R. Palkovits, *Appl. Catal., B*, 2016, **184**, 285–298.
496 V. C. Nguyen, N. Q. Bui, M. Eternot, T. T. H. Vu, P. Fongarland and N. Essayem, *Mol. Catal.*, 2018, **458**, 171–179.
497 S. E. Davis, B. N. Zope and R. J. Davis, *Green Chem.*, 2012, **14**, 143–147.
498 R. K. Pazhavelikkakath Purushothaman, F. van der Klis, A. E. Frissen, J. van Haveren, A. Mayoral, A. van der Bent and D. S. van Es, *Green Chem.*, 2018, **20**, 2763–2774.
499 Q. Meng, D. Cao, G. Zhao, C. Qiu, X. Liu, X. Wen, Y. Zhu and Y. Li, *Appl. Catal., B*, 2017, **212**, 15–22.
500 F. Liu, K. Huang, A. Zheng, F.-S. Xiao and S. Dai, *ACS Catal.*, 2018, **8**, 372–391.
501 J. N. Jocz, P. E. Savage and L. T. Thompson, *Ind. Eng. Chem. Res.*, 2018, **57**, 8655–8663.
502 D. W. Gardner, J. Huo, T. C. Hoff, R. L. Johnson, B. H. Shanks and J.-P. Tessonnier, *ACS Catal.*, 2015, **5**, 4418–4422.
503 A. C. Alba-Rubio, J. L. G. Fierro, L. León-Reina, R. Mariscal, J. A. Dumesic and M. L. Granados, *Appl. Catal., B*, 2017, **202**, 269–280.
504 W. N. P. van der Graaff, C. H. L. Tempelman, F. C. Hendriks, J. Ruiz-Martinez, S. Bals, B. M. Weckhuysen, E. A. Pidko and E. J. M. Hensen, *Appl. Catal., A*, 2018, **564**, 113–122.
505 H. N. Pham, A. E. Anderson, R. L. Johnson, K. Schmidt-Rohr and A. K. Datye, *Angew. Chem., Int. Ed.*, 2012, **51**, 13163–13167.
506 D. T. Ngo, T. Sooknoi and D. E. Resasco, *Appl. Catal., B*, 2018, **237**, 835–843.
507 H. N. Pham, A. E. Anderson, R. L. Johnson, T. J. Schwartz, B. J. O'Neill, P. Duan, K. Schmidt-Rohr, J. A. Dumesic and A. K. Datye, *ACS Catal.*, 2015, **5**, 4546–4555.
508 M. Karaki, A. Karout, J. Toufaily, F. Rataboul, N. Essayem and B. Lebeau, *J. Catal.*, 2013, **305**, 204–216.
509 R. F. Perez, S. J. Canhaci, L. E. P. Borges and M. A. Fraga, *Catal. Today*, 2017, **289**, 273–279.
510 S. Kang, J. Fu and G. Zhang, *Renewable Sustainable Energy Rev.*, 2018, **94**, 340–362.
511 H. Yang, C. Ma, X. Zhang, Y. Li, J. Cheng and Z. Hao, *ACS Catal.*, 2018, **8**, 1248–1258.
512 C. Sievers, Y. Noda, L. Qi, E. M. Albuquerque, R. M. Rioux and S. L. Scott, *ACS Catal.*, 2016, **6**, 8286–8307.
513 S. Prodinger, M. A. Derewinski, A. Vjunov, S. D. Burton, I. Arslan and J. A. Lercher, *J. Am. Chem. Soc.*, 2016, **138**, 4408–4415.
514 J. S. Bates and R. Gounder, *J. Catal.*, 2018, **365**, 213–226.
515 M. J. Cordon, J. W. Harris, J. C. Vega-Vila, J. S. Bates, S. Kaur, M. Gupta, M. E. Witzke, E. C. Wegener, J. T. Miller, D. W. Flaherty, D. D. Hibbitts and R. Gounder, *J. Am. Chem. Soc.*, 2018, **140**, 14244–14266.
516 Z. Jin, L. Wang, Q. Hu, L. Zhang, S. Xu, X. Dong, X. Gao, R. Ma, X. Meng and F.-S. Xiao, *ACS Catal.*, 2018, **8**, 5250–5254.
517 H.-T. Vu, F. M. Harth and N. Wilde, *Front. Chem.*, 2018, **6**, 143.
518 J. Grand, S. N. Talapaneni, A. Vicente, C. Fernandez, E. Dib, H. A. Aleksandrov, G. N. Vayssilov, R. Retoux, P. Boullay, J.-P. Gilson, V. Valtchev and S. Mintova, *Nat. Mater.*, 2017, **16**, 1010–1015.
519 Z. Zhu, H. Xu, J. Jiang, H. Wu and P. Wu, *Chem. Commun.*, 2017, **53**, 12516–12519.
520 D. Suttipat, W. Wannapakdee, T. Yutthalekha, S. Ittisanronnachai, T. Ungpittagul, K. Phomphrai, S. Bureekaew and C. Wattanakit, *ACS Appl. Mater. Interfaces*, 2018, **10**, 16358–16366.
521 Y. Tang, Y. Chen, Y. Wu, M. Zheng, C. Zhang, M. Yang and G. Cao, *Microporous Mesoporous Mater.*, 2016, **224**, 420–425.
522 R. A. Mayanovic, H. Yan, A. D. Brandt, Z. Wang, M. Mandal, K. Landskron and W. A. Bassett, *Microporous Mesoporous Mater.*, 2014, **195**, 161–166.
523 J. Choi, Y. Han, S. Park, J. Park and H. Kim, *J. Nanomater.*, 2014, **2014**, 580347.
524 M. N. Gatti, F. Pompeo, G. F. Santori and N. N. Nichio, *Catal. Today*, 2017, **296**, 26–34.
525 J. Huo, R. L. Johnson, P. Duan, H. N. Pham, D. Mendivelso-Perez, E. A. Smith, A. K. Datye, K. Schmidt-Rohr and B. H. Shanks, *Catal. Sci. Technol.*, 2018, **8**, 1151–1160.
526 J. A. Lopez-Ruiz, A. R. Cooper, G. Li and K. O. Albrecht, *ACS Catal.*, 2017, **7**, 6400–6412.
527 A. Aronne, M. Di Serio, R. Vitiello, N. J. Clayden, L. Minieri, C. Imparato, A. Piccolo, P. Pernice, P. Carniti and A. Gervasini, *J. Phys. Chem. C*, 2017, **121**, 17378–17389.
528 J. Oh, T. W. Kim, K. Jeong, J. H. Park and Y.-W. Suh, *ChemCatChem*, 2018, **10**, 3892–3900.
529 H. Xiong, T. J. Schwartz, N. I. Andersen, J. A. Dumesic and A. K. Datye, *Angew. Chem., Int. Ed.*, 2015, **54**, 7939–7943.
530 B. J. O'Neill, D. H. K. Jackson, A. J. Crisci, C. A. Farberow, F. Shi, A. C. Alba-Rubio, J. Lu, P. J. Dietrich, X. Gu, C. L. Marshall, P. C. Stair, J. W. Elam, J. T. Miller, F. H. Ribeiro, P. M. Voyles, J. Greeley, M. Mavrikakis, S. L. Scott, T. F. Kuech and J. A. Dumesic, *Angew. Chem., Int. Ed.*, 2013, **52**, 13808–13812.
531 T. Van Cleve, D. Underhill, M. Veiga Rodrigues, C. Sievers and J. W. Medlin, *Langmuir*, 2018, **34**, 3619–3625.
532 P. Hao, D. K. Schwartz and J. W. Medlin, *ACS Catal.*, 2018, 11165–11173.
533 Y. Rodenas, R. Mariscal, J. L. G. Fierro, D. Martín Alonso, J. A. Dumesic and M. López Granados, *Green Chem.*, 2018, **20**, 2845–2856.
534 W. N. P. van der Graaff, C. H. L. Tempelman, G. Li, B. Mezari, N. Kosinov, E. A. Pidko and E. J. M. Hensen, *ChemSusChem*, 2016, **9**, 3145–3149.
535 S. Gillet, M. Aguedo, L. Petitjean, A. R. C. Morais, A. M. da Costa Lopes, R. M. Lukasik and P. T. Anastas, *Green Chem.*, 2017, **19**, 4200–4233.
536 C. Liu, H. Wang, A. M. Karim, J. Sun and Y. Wang, *Chem. Soc. Rev.*, 2014, **43**, 7594–7623.
537 I. B. Laskar, K. Rajkumari, R. Gupta, S. Chatterjee, B. Paul and L. Rokhum, *RSC Adv.*, 2018, **8**, 20131–20142.
538 B. Liu and Z. Zhang, *ACS Catal.*, 2016, **6**, 326–338.